

Particle Image Velocimetry for Building Thermal Airflow Analysis

Cheng Zhang

A Thesis
in
the Department
of
Building, Civil, Environmental Engineering

Presented in Partial Fulfillment of the Requirements
for the Degree of
Master of Applied Science (Building Engineering) at
Concordia University
Montreal, Quebec, Canada

March 2019

© Cheng Zhang, 2019

CONCORDIA UNIVERSITY

SCHOOL OF GRADUATE STUDIES

This is to certify that the thesis prepared

By: Cheng Zhang

Entitled: Particle image velocimetry for building thermal airflow analysis

and submitted in partial fulfillment of the requirements for the degree of

Master of Applied Science (Building Engineering)

complies with the regulations of the University and meets the accepted standards with respect to originality and quality.

Signed by the final Examining Committee:

Dr. Theodore Stathopoulos Chair

Dr. Hoi Dick Ng Examiner

Dr. Samuel Li Examiner

Dr. Liangzhu (Leon) Wang Supervisor

Approved by

Chair of Department or Graduate Program Director

2019

Dean of Faculty

ABSTRACT

Particle image velocimetry for building thermal airflow analysis

Cheng Zhang

It is crucial to quantify the airflow field in and around a building, as this can provide information for creating a healthy and comfortable thermal environment for people. Over the last decade, particle image velocimetry (PIV) has gradually become the most popular measurement technique for measuring building environment airflow fields.

The objective of this thesis is to provide an overview of the typical two-dimensional PIV technique used in the building environment. The measurement principle and procedures are discussed based on the existing literature and previous research experiences. Four problems are investigated to show different applications of the PIV technique in measuring airflow fields, combined with other assessment models: the analytical model, the empirical model, the multizone model and the computational fluid dynamics (CFD) model. The performance of buoyancy-driven natural ventilation in a single-zone sub-scale model is studied using different experimental technologies. The behavior of single jet flow interaction with wind is investigated through experimental and numerical methods. The hybrid ventilation flow field and temperature distribution is measured by PIV and thermocouple experiments. PIV, combined with empirical models, is used to predict localized mechanical ventilation system performance in a warehouse model. The results show that the quantitative and detailed flow information obtained by PIV can be used for flow pattern visualization, flow structure analysis, numerical model validation, and empirical model correlation. The limitations of the PIV technique in sub-scale model measurements is also discussed.

ACKNOWLEDGEMENTS

I would like to express my very great appreciation to my supervisor Dr. Liangzhu (Leon) Wang. Advice and supervision given by Dr. Wang has been a great help in completing this thesis. I would like to offer my special thanks for his valuable and constructive suggestions during planning and working of this research.

Furthermore, I would like to express my appreciation to Dr. Wael Fayrouz, who taught me how to use PIV system and provided significant support and advice. I would also like to thank various colleagues in the group, Dr. Dahai Qi, Weigang Li, Chang Shu, Senwen Yang, Xin Zhang and Ali Katal for their assistance. In particular: Dr. Dahai Qi provided great advice on my research. Senwen Yang and Xin Zhang helped to build experiment model and measurements. Chang Shu, Senwen Yang and Weigang Li provided assist and advice on CFD simulation setup, Ali Katal assisted to build the simulation model. It is a joyful experience to work with them and learn research skills from them.

I would also like to acknowledge the permission from Dr. Andreas Athienitis and Dr. Ted Stathopoulos for using the particle image velocimetry system, and permission from Dr. Lyes Kadem for using the traverse system, without which this thesis work would not be possible. We would like to continue the collaborations with them.

I would like to acknowledge the financial and technical support from the Air Management and Control Association (AMCA) and NutraPonics Canada Corporation.

Finally, I wish to thank my parents for their support and encouragement, without their help, it is impossible to complete this research. I also wish to thank my friends in Canada and China, as it is helpful to have their support and encouragement.

TABLE OF CONTENTS

ACKNOWLEDGEMENTS.....	iv
LIST OF FIGURES	x
LIST OF TABLES.....	xvii
NOMENCLATURE	xviii
ACRONYMS.....	xxi
1 Introduction.....	1
1.1 Background	1
1.2 Motivation	5
1.3 Objectives.....	7
2 Literature review.....	8
2.1 PIV for ventilation devices.....	8
2.1.1 External airflow of ventilation devices.....	8
2.1.2 Internal airflow of ventilation devices	11
2.2 PIV for airflow around persons.....	11
2.3 PIV for indoor airflows	13
2.3.1 Sub-scale model testing	13
2.3.2 Full-scale model testing.....	15
2.4 PIV for outdoor airflows	17
2.5 PIV errors and uncertainties.....	20

3	PIV methodology and application cases	23
3.1	PIV system components	23
3.1.1	Illumination system.....	24
3.1.2	Image recording devices	26
3.1.3	Tracer particles.....	27
3.2	Experimental procedure	29
3.2.1	Preparation	29
3.2.2	Setup and calibration.....	30
3.2.3	Data acquisition	32
3.2.4	Data processing.....	34
3.3	PIV application cases	42
4	Natural ventilation in single zone model	44
4.1	Introduction	44
4.2	Methodology	45
4.2.1	Experimental design.....	45
4.2.2	Particle image velocimetry measurement setup.....	46
4.2.3	Tracer gas test setup.....	48
4.3	Results and discussions	51
4.3.1	Preliminary test and test plan.....	51
4.3.2	Airflow validation with tracer gas measurement	54

4.3.3	Indoor flow without ventilation	55
4.3.4	Indoor flow with natural ventilation	56
4.4	Conclusions	65
5	Air curtain interaction with wind	66
5.1	Introduction	66
5.2	Methodology	67
5.2.1	Model Configuration.....	67
5.2.2	PIV measurement setup	68
5.2.3	CFD simulation for wind tunnel experiment	69
5.2.4	Air curtain flow analytical model	72
5.3	Results and discussions	74
5.3.1	Comparing PIV, CFD, and analytical results.....	74
5.3.2	Wind tunnel wind field	75
5.3.3	Jet flow visualization	76
5.3.4	Effects of air supply and validation with CFD simulation results	78
5.3.5	Effects of wind and validation with CFD simulation results	82
5.3.6	Effects of the vestibular and people in different positions	84
5.3.7	Results comparison in full-scale experiments and sub-scale experiments	86
5.4	Conclusions	87
6	Hybrid ventilation in sub-scale high-rise buildings	89

6.1	Introduction	89
6.2	Methodology	89
6.2.1	Experimental design.....	89
6.2.2	PIV measurement setup	91
6.2.3	Numerical simulation model.....	92
6.3	Results and discussion.....	93
6.3.1	Airflow field measurement results.....	93
6.3.2	Temperature measurement results	96
6.3.3	Comparison with simulation results.....	97
6.4	Conclusions	100
7	Mechanical ventilation in a sub-scale warehouse.....	101
7.1	Introduction	101
7.2	Methodology	102
7.2.1	3D printing model and experimental design.....	102
7.2.2	PIV measurement setup	104
7.2.3	CFD simulations	105
7.2.4	Single jet flow empirical model.....	107
7.3	Results and discussions	108
7.3.1	CFD simulation results	108
7.3.2	Flow field measurement results	110

7.3.3	PIV data correlation results.....	112
8	Discussion and conclusions	117
8.1	Conclusions	117
8.2	Contributions of this study	119
8.3	Limitations of the study.....	119
8.4	Future work	120
	References.....	121
	Appendix1: PIV measurement procedure.....	134
	Appendix2: Tracer gas measurement procedure.....	147

LIST OF FIGURES

Figure 1-1. Illustration of the parts and overall framework of the research.	6
Figure 2-1. Jet visualization and the corresponding instantaneous vector field by PIV pair- photograph at a slot velocity of 0.8 m/s. (a) Laser sheet pair-image one; (b) laser sheet pair-image two; (c) instantaneous velocity vector field.	9
Figure 2-2. Particle image velocimetry measurement setup.	12
Figure 2-3. Average velocity field on the central plane for three cases.	15
Figure 2-4. (a) Measured cross section of the cabin mockup; (b) Sub-regions in the measured cross section.	16
Figure 2-5. (a) The perspective view of the tornado-like vortex. (b) Reconstructed 3-D views of vortex structure around the test model.	18
Figure 3-1. Schematic of a 2D PIV measurement system in a wind tunnel [13].	24
Figure 3-2. Double-pulsed Nd:YAG laser system [112].	25
Figure 3-3. FlowSense EO CCD camera.	26
Figure 3-4. Tracer particles and generators: (a) aluminum oxide powder; (b) oil droplets and the associated generator; (c) fog fluid and fog machine.	29
Figure 3-5. (a) Model designed for PIV experiments; (b) traverse used in PIV experiments.	30
Figure 3-6. Calibration target.	32
Figure 3-7. Photographs of the flow with seeded particles: (a) an excess of particles in the flow; (b) acceptable particle seeding; (c) insufficient particles in the flow.	33
Figure 3-8. Reflection on the models.	33
Figure 3-9. Photographs of particles separation between two frames.	34
Figure 3-10. Pre-processing of PIV images.	35

Figure 3-11. Image evaluation results.....	36
Figure 3-12. Image evaluation results with peak validation and local neighborhood validation.	38
Figure 3-13. Schematic representation of the evaluation procedures of the PIV results.....	39
Figure 3-14. Examples of post-processing: (a) turbulence kinetic energy of the flow around the plant; (b) scalar mean map of the flow around the plant.	40
Figure 3-15. Flow chart of the main steps of the PIV experiment and associated critical parameters.	41
Figure 4-1. Schematics of the sub-scale model with heated floor.	46
Figure 4-2. Schematics of the thermocouples' locations inside the chamber.....	46
Figure 4-3. Area measured using PIV.....	47
Figure 4-4. High pressure gas analyzer UGA 100.....	50
Figure 4-5. Tracer gas measurement setup.	50
Figure 4-6. Indoor flow field velocity vectors combined with the PIV results of the four planes.	51
Figure 4-7. Indoor flow field velocity streamlines combined with the PIV results of the four planes.	52
Figure 4-8. Comparison of the velocity contour captured by the four measurement planes verses one measurement plane.....	52
Figure 4-9. Temperature changes after heaters were turned on.....	53
Figure 4-10. CO ₂ concentration changes in tracer gas measurement (airflow rate 0.000338 m ³ /s).	54
Figure 4-11. Schematic view of airflow rate calculation method using PIV results.	55
Figure 4-12. Indoor flow field streamlines without ventilation.....	56

Figure 4-13 Indoor flow streamlines with foam base	58
Figure 4-14 Indoor flow streamlines with wood base	61
Figure 4-15 Temperature (°C) distribution with foam base	63
Figure 4-16 Temperature (°C) distribution with wood base.....	64
Figure 5-1. (a) Atmospheric boundary layer wind tunnel at Concordia University; (b) scaled-down chamber model.....	67
Figure 5-2. PIV measurements setup.....	69
Figure 5-3. Mesh structure for CFD simulations. (a) Whole domain; (b) model.	70
Figure 5-4. Schematic view of the model with outer domain.....	70
Figure 5-5. Velocity and turbulence intensity profiles of the wind tunnel flow: (a) 4 m/s reference velocity; (b) 10 m/s reference velocity.	71
Figure 5-6. Schematic of slot jet impingement on a flat surface.	72
Figure 5-7. Visualization of air curtain at 10 Hz. A) potential core zone; B) transition zone; C) developed zone.....	73
Figure 5-8. Centerline velocity below the air supply inlet (Case1: air curtain supply speed 9.6 m/s and supply angle 0°, ΔP -2.67 Pa; Case2: air curtain supply speed 9.6 m/s and supply angle 0°, ΔP 1.74 Pa; Case3: air curtain supply speed 9.6 m/s and supply angle 0°, ΔP 6.17 Pa).....	74
Figure 5-9 Wind field contour of wind tunnel.....	75
Figure 5-10 Wind filed streamlines of wind tunnel.....	75
Figure 5-11. Flow visualization of air curtain jet flow under 0.00285 m ³ /s infiltration at the door: (a) 9.6 m/s supply velocity; (b) 5.7 m/s supply velocity; (c) 2 m/s supply velocity.....	77
Figure 5-12. Flow visualization of air curtain jet flow under 0.00056 m ³ /s exfiltration: (a) 9.6 m/s supply velocity; (b) 5.7 m/s supply velocity.	77

Figure 5-13. Performance curve and velocity vectors of 0° air curtains with an average supply speed of 9.6 m/s under 4 m/s wind obtained by experimental and numerical methods.	79
Figure 5-14. Performance curve and velocity vectors of 20° air curtains with an average supply speed of 9.6 m/s under 4 m/s wind obtained by experimental and numerical methods.	79
Figure 5-15. Performance curve and velocity vectors of 0° air curtains with an average supply speed of 9.6 m/s under 10 m/s wind obtained by experimental and numerical methods.	80
Figure 5-16. Performance curve and velocity vectors of 20° air curtains with an average supply speed of 9.6 m/s under 10 m/s wind obtained by experimental and numerical methods.	80
Figure 5-17. Performance curve and velocity vectors of 0° air curtains with an average supply speed of 9.6 m/s under no wind conditions obtained by experimental and numerical methods...	81
Figure 5-18. Performance curve and velocity vectors of 0° air curtains with an average supply speed of 5.6 m/s under no wind conditions obtained by experimental and numerical methods...	82
Figure 5-19. Velocity vectors of air curtains with 9.6 m/s supply velocities and 0° supply angles, under the same pressure conditions ($\Delta P=2.5$ Pa) obtained by the experimental and numerical methods.	83
Figure 5-20. Velocity vectors of air curtains with 9.6 m/s air supply velocities and 0° air supply angles under 10 m/s wind obtained by experimental methods.	84
Figure 5-21. Velocity vectors of air curtains with 9.6 m/s air supply velocities and 0° air supply angles, under 4 m/s outside wind obtained by the experimental method.	85
Figure 5-22. Velocity vectors of air curtains with 9.6 m/s air supply velocities and 0° air supply angles under 10 m/s outside wind conditions obtained by experimental methods.	85
Figure 5-23. Comparison of velocity vectors of air curtains with 9.6 m/s air supply velocities and 20° air supply angles between full-scale and sub-scale experimental methods.	86

Figure 5-24. Performance curve of air curtains with 9.6 m/s air supply velocities and 0° air supply angles.	88
Figure 5-25. Performance curve of air curtains with 9.6 m/s air supply velocities and 20° air supply angles.	88
Figure 6-1. EV building model. (a) SE facade of EV building model; (b) top view of the EV building model.	90
Figure 6-2. Schematic PIV experiments setup.	91
Figure 6-3. Velocity contour of flow across corridor grilles under natural ventilation conditions.	93
Figure 6-4. Velocity contour of flow across corridor grilles under hybrid ventilation conditions.	94
Figure 6-5. Airflow rate through the corridor grilles under natural ventilation conditions.	95
Figure 6-6. Airflow rate through the corridor grilles under hybrid ventilation conditions.	96
Figure 6-7. Temperature (°C) distribution in corridors, offices, and atriums: (a) natural ventilation; (b) hybrid ventilation.	97
Figure 6-8. Comparison of natural ventilation air flow rates at the inlet dampers between the PIV experimental results and numerical results.	98
Figure 6-9. Comparison of hybrid ventilation air flow rates at the inlet dampers between the PIV experimental results and the numerical results.	99
Figure 7-1. Full-scale growing bed experiment. Left: with localized air supply. Right: without localized air supply.	102
Figure 7-2. 3D-printed crop model.	103
Figure 7-3. Schematic PIV experiment setup.	105

Figure 7-4. Schematic view of the growing bed model.....	106
Figure 7-5. Mesh structure of the air supply system and growing bed.....	106
Figure 7-6. Schematic of the round free jet.....	107
Figure 7-7. Simulated velocity field contours: (a) full-scale model; (b) sub-scale model.....	109
Figure 7-8. Simulated 3D velocity field streamlines: (a) full-scale model; (b) sub-scale model.	109
Figure 7-9. Jet flow rates for the full-scale model and the sub-scale model.....	110
Figure 7-10. Visualization of the flow field with 6.8 cfm air supply flow rate.....	111
Figure 7-11. Flow field vectors measured by PIV.....	111
Figure 7-12 Flow field contours measured by PIV.....	112
Figure 7-13. Dimensionless centerline velocity below the nozzle inlet.....	113
Figure 7-14. Dimensionless centerline velocity below the nozzle inlet.....	114
Figure 7-15. Dimensionless jet diameter.....	115
Figure 8-1. Procedure for PIV experimental studies in sub-scale building model airflow environments.....	118
Figure A1-1 DynamicStudio devices list.....	135
Figure A1-2 Control panel of laser.....	137
Figure A1-3 Acquisition setup in DynamicStudio system control panel.....	138
Figure A1-4 Measure scale factor for calibration.....	139
Figure A1-5 Define mask.....	142
Figure A1-6 Adaptive correlation: (a) interrogation areas; (b) validation.....	144
Figure A1-7 (a) average filter; (b) vector statistics.....	145
Figure A1-8 Numeric export.....	146

Figure A2-1 UGA schematic[107].....	147
Figure A2-2 Connection Settings.....	148
Figure A2-3 UGA software	149
Figure A2-4 Scan Schedule Setup	151
Figure A2-5 Scan Parameters	152

LIST OF TABLES

Table 1. Technical specifications for CCD camera.	26
Table 2. Particle seeds diameter and scattering cross section.....	28
Table 3. PIV application cases.....	43
Table 4. Setup of PIV data acquisition and evaluation.	48
Table 5. Characteristics of tracer gases.....	49
Table 6. Setup of PIV data acquisition and evaluation.	69
Table 7. Setup of PIV data acquisition and evaluation.	91
Table 8. Romaine lettuce growth stages.	103
Table 9. Parameters of the sub-scale model and corresponding parameters of the full-scale model.	104
Table 10. Setup of PIV data acquisition and evaluation.	105
Table 11 Localized mechanical ventilation system performances according to modified empirical models.....	116
Table 12 Evaluation methods in DynamicStudio	143

NOMENCLATURE

a	Empirical constant
A	Area (m^2)
b_0	Nozzle width, m
C	Flow coefficient
C_c	cross section, m^2
C_d	Discharge coefficient
C_g	Concentration of tracer gas, kg/m^3
C_p	Specific heat capacity of the air ($J/(kg \cdot ^\circ C)$)
C_{pw}	Specific heat capacity of the envelope ($J/(kg \cdot ^\circ C)$)
C_s	Roughness constant
d_{int}	Desired interrogation area, pixels
D_0	Jet flow diameter
d_0	Diameter of orifice
d_p	Diameter of the particles, μm
g	Gravitational acceleration, m/s^2
H	Distance between top and bottom openings (m)
h	Convective coefficient ($W/(m^2 \cdot K)$)
h_t	Heat transfer coefficient, $Btu/s \cdot ft^2 \cdot ^\circ F$
k	Conduction heat transfer coefficient ($W/(m \cdot K)$)
k_s	Sand-grain roughness height, m
L	Thickness (m)
M	Mass (kg)

\dot{m}	Mass flow rate (kg/s)
P	Pressure (Pa)
Q	Heat source (W)
Q_r	ventilation rate, m ³ /s
S	Airflow source of certain zone
T	Temperature (°C)
Δt	Delay time, μ s
U	Overall heat transfer coefficient (W/(m ² ·K))
u	Jet centerline velocity, m/s
u_f	Velocity of air, m/s
u_g	Velocity of particles, m/s
U_{max}	Maximum velocity of the shooting section, pixels/s
u_0	Jet initial velocity, m/s
u_{p0}	Initial velocity of particles, m/s
V	Total volume of the ventilated space, m ³
\bar{x}	Distance to the nozzle which direction tangent to the jet centerline, m
Δx	Separation of the particle images, pixels
\bar{y}	Distance to the jet centerline which direction normal to the jet centerline, m
Z	Floor elevation (m)
Z_0	Aerodynamic roughness length, m
<i>Greek symbols</i>	
ρ_f	Density of the air, kg/ μ m ³
ρ_p	Density of the particles, kg/ μ m ³

μ Dynamic viscosity of the air, $\text{kg}/\mu\text{m} \cdot \mu\text{s}$

τ_p Relaxation time of the particles, μs

σ_1 Empirical constant

σ_2 Empirical constant

Subscripts

i Interior air

o Outside air

s Sub-scale model

w Envelope

z Zones

ACRONYMS

CCD	Coupled Charged Devices
CFD	Computational Fluid Dynamics
CMOS	Complementary Metal Oxide Semiconductor
HVAC	Heating, Ventilation, and Air conditioning
IA	Interrogation Area
LDV	Laser Doppler velocimetry
LSM	Least squares matching
NRMSD	Normalized Root-Mean-Square Deviation
PIV	Particle Image Velocimetry
POD	Proper Orthogonal Decomposition
PSV	Particle Streak Velocimetry
PTV	Particle Tracking Velocimetry
RANS	Reynolds-Averaged Navier-Stokes
RMS	Root mean square
ROI	Region Of Interest
SRS	Stanford Research Systems
TKE	Turbulence Kinetic Energy
UGA	Universal Gas Analyzer

1 INTRODUCTION

1.1 Background

Understanding the movement of air inside and around buildings is important, as it has a significant influence on people's comfort, health and safety, and on the efficiency and effectiveness of space heating, cooling, and ventilation [1][2]. Air movement through or around buildings results from the pressure difference between the indoors and outdoors or one area and another area, which can be caused either by natural forces, like the wind or stack effects, or by mechanical forces, like fans. Ventilation, one kind of air movement, can be used for the purposes of promoting indoor air quality, thermal comfort, or dehumidification by regulating some indoor air parameters, such as air speed, temperature, relative humidity, and chemical species concentrations in the air [3][4]. Not only indoor airflow, but outdoor wind conditions are also important to prevent uncomfortable or dangerous situations [1][5]. In terms of ventilation and outdoor wind, the performance of air flow movement can be assessed in terms of air velocity, air temperature, airflow pattern, air pressure, the distribution of contaminant concentration, global ventilation effectiveness, air distribution effectiveness, airflow rate through the openings of buildings, local age of air, and so on[1][4-9]. Among all the parameters that evaluate the performance of outdoor wind or ventilation and air distribution systems, the airflow patterns (such as trajectory, impingement, separation, circulation, reattachment, buoyancy, vortices, etc.) and airflow field (such as velocity and temperature) are some of the most widely discussed issues, according to various studies [6][7]. Knowing the airflow pattern, wind speed, and pressure around buildings is of importance for designing durable building structures and envelopes [1] and providing safe and comfortable wind environments [5]. Air motion's responsibility for transporting heat and pollutants makes it one of main factors influencing the indoor environment quality [7]. Furthermore, the air distribution

system plays an important role in minimizing energy consumption while simultaneously promoting indoor environment comfort [8].

Numerical simulations and experimental measurements are normally used to predict and evaluate the performance of outdoor wind, ventilation, and air distribution systems. Numerical simulations using computational fluid dynamics (CFD) have become more and more popular for dealing with the performance of outdoor wind, ventilation, and air distribution system in buildings due to the rapid development of computer calculation capacity and speed. Compared to experimental methods, the CFD model can provide both global and detailed airflow information with less time consumption and at relatively low cost by solving a series of equations for the conservation of mass, momentum, energy, and species concentrations. For pedestrian level wind, CFD simulation models are built using the 3D steady Reynolds-Averaged Navier-Stokes approach. Large eddy simulation (LES) is used less often, as it is more complex and time consuming.

Although numerical simulations are very helpful for prediction, assessment, or the design of air motion inside or around a building, CFD results cannot be fully trusted, as they may vary greatly when using different models due to the simplified assumptions and limited understanding of boundary layer conditions [9]. Therefore, conducting numerical simulations always relies on high-quality experimental data to provide accurate measurement data such as boundary conditions and to validate simulation results. Overall, to obtain more precise and reliable information on airflow patterns and velocity distributions, experimental measurement is still necessary to be conducted as the fundamental step in air motion studies.

Due to the fact that the air flow inside and around a building is complex and normally characterized as three-dimensional, having high turbulence levels, and unsteady, it is not easy to obtain accurate and complete airflow field information in building environment measurements. According to Sun

and Zhang's work [10], the most common modern airflow measurement techniques have been summarized and can be divided into point-wise and global-wise in general. Point-wise methods, such as hot-wire anemometry, pitot tubes, and laser Doppler velocimetry, can provide quantitative velocity data points at discrete locations in the flow field with the moving of a probe. Based on different principles of measurement, point-wise techniques can be categorized into: thermal anemometers, including hotwire anemometry, hot-film anemometry, and hot-sphere anemometry, which measure air motion velocity through its relationship to the convective cooling of electrically heated sensing elements [11]; pitot tube and rotating vane anemometers, which are able to sense air speed from pressure differences [10]; ultrasonic anemometry, which is typically used to collecting meteorological data by sensing variations in sound wave speed; and laser Doppler velocimetry (LDV), which obtains fluid velocity data by detecting Doppler shifts. The global-wise techniques, which include particle tracking velocimetry (PTV), particle streak velocimetry (PSV), and particle image velocimetry (PIV), can provide spatially continuous velocity information over the whole flow field based on optical principles. Some other global-wise measurement techniques used in wind tunnels have been summarized by B. Blocken, T. Stathopoulos, and J.P.A.J. van Beeck [5]. For examples, Irwin probes, which allow measurements at numerous locations, can be very easy to use; scour techniques, which measure wind speed by examination of erosion/scouring patterns of some particulate material (often sand) created by outdoor airflow, can provide velocity information over the whole surface area; and infrared thermography can measure the root-mean-square, peak, and spectrum values of the temperature and wind speed over an area based on the relationship between heat transfer and flow conditions near the building surface [5][12].

The traditional point-wise method, as it can only acquire the flow velocity data at the single point of the probe sensor, has difficulties describing the detailed full-scale airflow of the indoor

environment. Other difficulties also remain for point-wise velocimetry techniques, such as the measurement of low air velocities, the direction of airflow, high turbulence intensity, and so on[9]. For thermal-based anemometers, the buoyancy effect and free convection will affect the results' accuracy when measuring the low speed airflow field. For the anemometers with probes, the sensing head will unavoidably create perturbations to the airflow field that are hard to evaluate. With (LDV), low velocity airflow can be accurately measured without disturbing the flow field, but it is expensive and time consuming to measure point by point.

Therefore, nonintrusive, accurate, and fast area measurement techniques like optical velocimetry are needed and regarded as alternative tools for measuring indoor and outdoor airflow. Optical velocimetry can measure the airflow velocities and other related information in a global domain without low velocity limitations and disturbing the flow field. As the most widely used method for optical velocimetry, PIV has been used and developed for the investigation of air and water flows for the past 30 years. The progress made in the recent past has already brought PIV to a state where it is routinely applied in aerodynamic research and related fields [13][16].

Particle image velocimetry experiments can be conducted in both full-scale and sub-scale models. In general, sub-scale models are very suitable for PIV measurements as the dimensions of sub-scale models are similar to the field of view of typical PIV systems [7]. However, it is essential for sub-scale models to be built using transparent materials to allow camera and laser shooting. In addition, the boundary conditions for the experiment must be modified according to the dimensions of the model and scaling theory.

In summary, it is necessary to conduct PIV measurements and analysis for many building ventilation performance studies.

1.2 Motivation

The reviewed publications revealed that PIV techniques are one of the most widely-used velocimetry methods for indoor ventilation problems. It is necessary to learn the PIV technique and apply it to different building environment problems as it can provide high quality quantitative results that are crucial for creating a thermally comfortable and healthy environment. Also, it is essential to learn to combine the PIV technique with the analytical model, the empirical model, the CFD model, the multizone model, and other experimental methods, as the PIV technique has its limitations. The analytical model is normally used to provide quick estimates of ventilation performance and reflect the most important features of system performance under certain assumptions [4], so it cannot provide the most accurate and detailed flow information. The analytical model can, however, provide a global guide for PIV study of ventilation problems and validation data for PIV experimental results. Very similar to the analytical model, the empirical model can be an effective way to predict ventilation performance in buildings, but needs experimental data to determine the coefficients. With highly accurate PIV data, empirical models can be developed and ventilation performance of buildings under different parameter inputs can be predicted simply and without repetition of the PIV tests. As one of the most important tools in ventilation research, CFD can provide accurate and reliable simulation results, but only with verification and validation studies of the CFD model. As some environmental conditions cannot be achieved in experiments, CFD simulations need to be performed to provide more data for ventilation performance studies. The multizone model can quickly obtain air exchange rates and airflow distributions in buildings, but it has limitations due to the assumptions used. As it is hard to conduct full-scale PIV tests in large buildings, a multizone model validated by PIV experimental data can be used to analyze ventilation performance for large-sized buildings. Fig. 1-1 shows the

overall structure of the thesis and relationship between PIV and other assessment models for predicting ventilation performance.

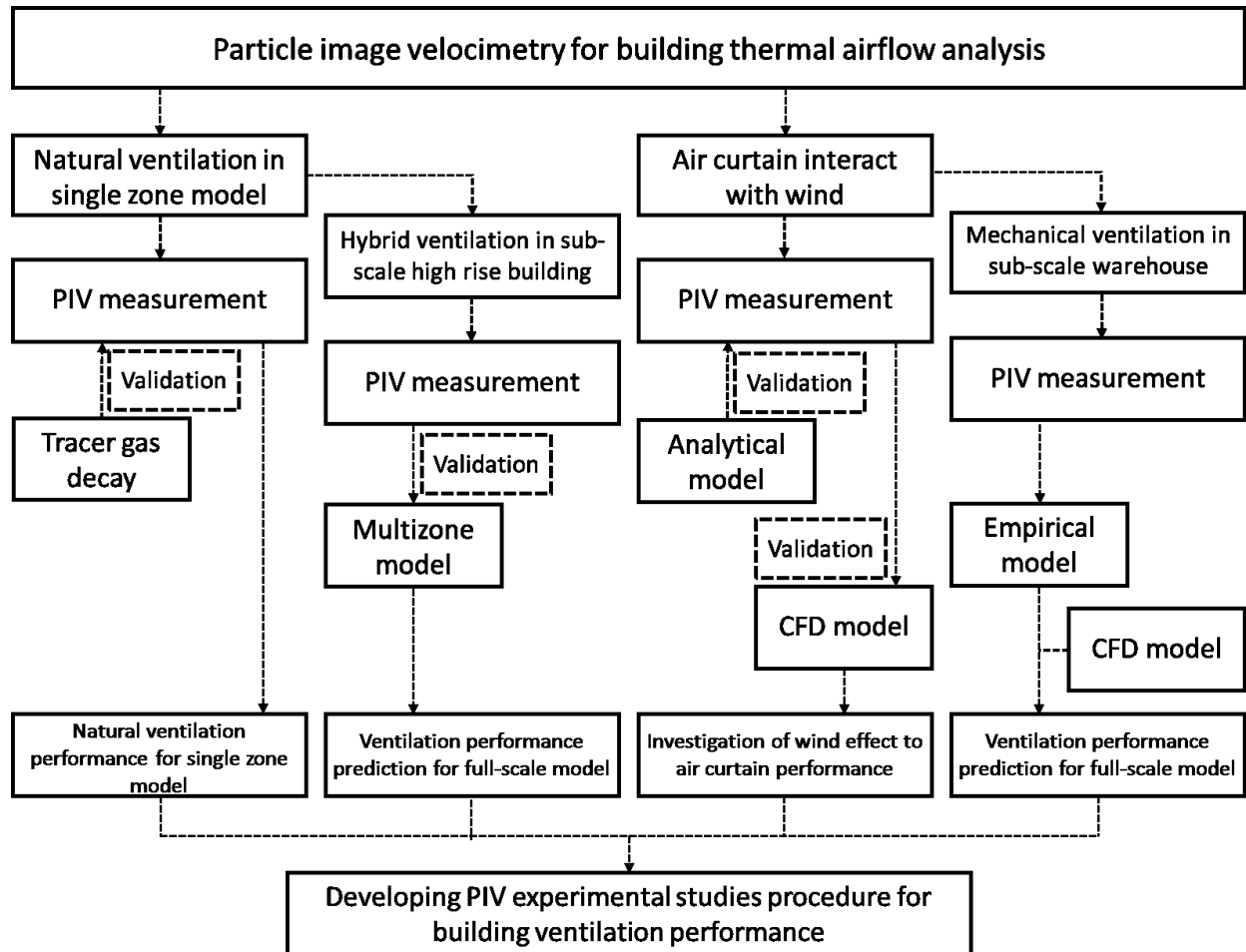


Figure 1-1. Illustration of the parts and overall framework of the research.

1.3 Objectives

Based on the background of air movement measurement techniques and literature reviews about PIV application, the general scope of this research involves studying the application of the PIV techniques in regards to the measurement of building ventilation performance.

The general objectives of this research are:

- to experimentally study the typical problems to which PIV can be applied according to previous researchers' studies,
- to investigate and discuss some of the factors that would affect the accuracy of PIV results, and,
- to develop the PIV measurement and analysis procedure and discuss about how to combine the PIV technique and other numerical models.

Based on the general scope and objectives proposed, four specific tasks are formulated:

Task 1: Study the thermal effects of airflow distribution and natural ventilation of a one-zone building model using PIV methods.

Task 2: Use PIV experimental techniques and CFD numerical simulations to evaluate the performance of air curtains under different wind speeds and directions, and the interactions with an air curtain jet considering different supply speeds, angles, and pressure differences across the air curtain.

Task 3: Study the natural and hybrid ventilation performance of a sub-scale high-rise building model using the PIV technique and PIV data for multizone model validation.

Task 4: Conduct PIV experimental measurements of flow fields for a mechanical ventilation system in warehouse and use the data to develop empirical multi-jet flow models.

2 LITERATURE REVIEW

This chapter aims to provide a review of PIV measurements and analysis for ventilation devices' airflows, airflow around persons, indoor airflows, and outdoor airflows. Also, PIV-related errors and uncertainty analyses are considered and discussed.

2.1 PIV for ventilation devices

2.1.1 External airflow of ventilation devices

Per-Ake Elvsen and Mats Sandberg [15] used PIV techniques to visualize the trajectory and entrainment of the flow discharged by an air diffuser with 20 nozzles. It was shown from the average flow vectors maps obtained from PIV that there was a small entrainment in the jet at the upper part of the flow.

Amina Meslem et al. [16] studied the twin cross-shaped jet and twin circular jet supplied through a lobed diffuser using the PIV method to acquire the instantaneous spatial distributions of the flow velocities. Three PIV systems were employed according to the different flow field conditions: a classical two-component PIV system, a stereoscopic time-resolved PIV system, and a large-scale classical stereoscopic PIV system. Cold paraffin oil droplets 1-4 μm diameter provided by a liquid seeding generator were used as tracing seeds in the experiments. The conclusion was that compared to the reference circular shape, an integration of the cross-shaped geometry can be a better method of passive control of air diffusion systems for buildings in comparison with the mixing efficiency, entrained flow rate, global flow uniformity and throw flow length of the jets.

Lupita D. Montoya et al. [17] conducted PIV experiments to measure the flow velocity vector fields in a closed chamber with synthetic jet actuators improving the indoor air quality. The results

were used to demonstrate the effectiveness of synthetic jets in controlling the airflow field, removal of particulate contaminants, and aerosol dispersion.

Guangyu Cao et al. [20][21] investigated turbulent attached jet flow behaviors in the entrainment process of ambient air downstream from a jet slot in a room with an active chilled beam located at the ceiling using PIV techniques. The PIV system was able to achieve the visualization of the flow field and the measurement of the instantaneous and time-averaged velocity vector fields. Also, the detailed mean and instantaneous jet flow at high turbulence intensity and low Reynolds numbers were able to be visualized and measured by a PIV system, as shown in Fig. 2-1. The PIV accuracy was discussed by comparing its results with the flow velocity at a distance of 0.3 m from the jet slot as measured by an anemometer.

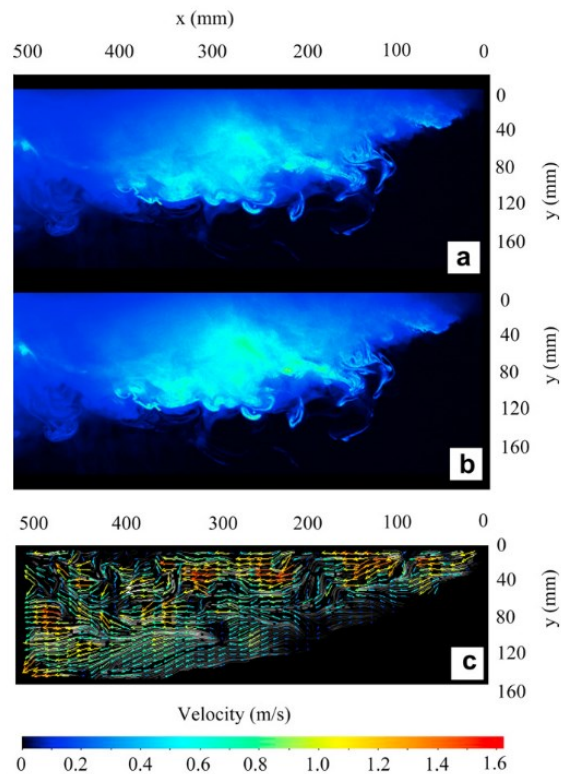


Figure 2-1. Jet visualization and the corresponding instantaneous vector field by PIV pair-photograph at a slot velocity of 0.8 m/s. (a) Laser sheet pair-image one; (b) laser sheet pair-image two; (c) instantaneous velocity vector field.

E. Nino et al. [20] investigated using PIV techniques the fluid dynamic characteristics of a rectangular air jet, simulating an air curtain, which was generated by a rectangular nozzle with a 0.02 m^2 discharge area. From the measurement results, the main characteristics of the air curtain jet can be inferred as a homogeneous velocity distribution in the exit section of the nozzle and the formation of an instable vortex.

Amina Meslem et al. [21] measured using PIV techniques the flow field of a turbulent twin cross-shaped jet generated from a perforated panel diffuser, and the results were used to validate various numerical models. The results showed that the SST $k-\omega$ model was the most appropriate tool for the optimization of jet induction on a lobed perforated panel for HVAC applications.

Ilinca Nastase et al. [22] used PIV techniques to study the jet flow issued from two kinds of grilles: a commercial grille with straight ailerons and grille with lobed ailerons. The conclusion was made according to the measurement results that the air flow generated from the grille with lobed ailerons offered a larger induction and a longer throw, and a better jet flow distribution in the occupied zone.

Dilek Kumlutas et al. [23] carried out an analysis of fluid flow characteristics of split air conditioners (SACs) by numerical and experimental methods. Stereo particle image velocimetry (SPIV) measurements were conducted to capture the flow velocity distributions in nine measurement planes at the outlet of a SAC device with a straight cross-flow fan (CFF). The measurement results were also compared with CFD simulation results, which showed that they were concordant within acceptable limits.

2.1.2 Internal airflow of ventilation devices

N. Chami and A. Zoughaib [24] conducted PIV experiments to measure the buoyancy-driven air flow rate inside of tilted differentially heated thermosyphons. A numerical CFD model representing natural convection was also developed and validated by PIV measurement results.

Cristina Sanjuan et al. [27][28] studied the fluid dynamic behavior of open joint ventilated façades, using PIV methods to measure the airflow generated inside of the naturally ventilated cavity. Various CFD models were developed, and according to the comparison of the PIV measurement results and the numerical results, the RNG k-epsilon turbulence model and the discrete ordinate radiation model showed the best fitting velocity profiles. The results from the selected numerical model showed that the ventilation air flow inside the cavity is enhanced by incident radiation and the height of the façade.

2.2 PIV for airflow around persons

David Marr et al. [52][53] studied the flow transport phenomenon occurring around persons in the indoor environment as a result of breathing and its level of anisotropy by using a time-resolved PIV system to obtain quantitative velocity vectors in the breathing zone of a thermal manikin. The measurement results showed that the airflow in the breathing zone is highly anisotropic, so that the common isotropic assumptions made in this environment are not admissible.

They also conducted stereo PIV experiments to measure flow along the inlet of an isothermal ventilation system as it interacts with the buoyancy effects of the standing thermal manikin [29]. Particle image velocimetry results suggested an increase in both integrated correlation length scale as well as a wide range of turbulence intensities in the indoor environment.

Özcan, O. et al. [30] employed the PIV technique to obtain the mean velocity and vorticity data of the flow around the head of a real-life size thermal manikin under the two cases of “no breathing” and “continuous exhalation through nose” within a special chamber providing stationary convective flows around the manikin. The mean velocity fields and mean vorticity fields of flow under the two cases were compared.

A.D. Eisner et al. [31] carried out a PIV experiment to obtain the qualitative images of the flow induced by foot motion. A time sequence of images was acquired using a PIV system and was able to help elucidate how foot motion affects air transport and how walking affects contaminant dispersion.

Shengwei Zhu et al. [32] investigated the transport characteristics of saliva droplets produced by coughing within a calm indoor environment with experimental and numerical analysis. Particle image velocimetry was used to measure the velocity distribution around the mouth of the coughing subject as shown in Fig. 2-2.

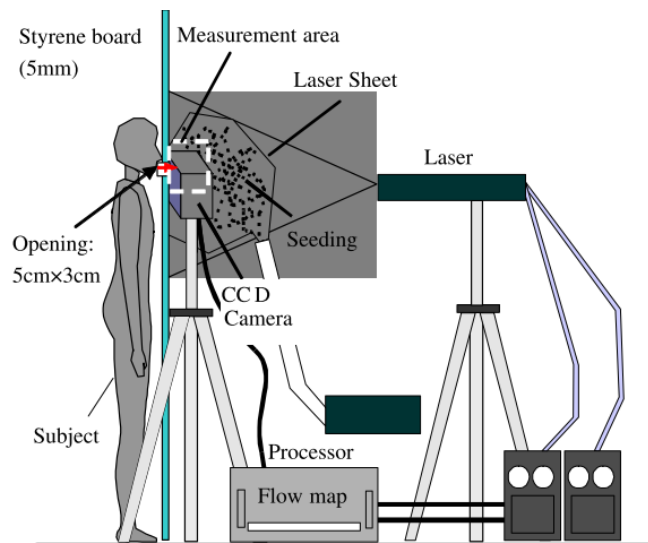


Figure 2-2. Particle image velocimetry measurement setup.

Brent A. Craven and Gary S. Settles [33] characterized the buoyancy plume velocity field around a volunteer in a temperature-stratified indoor environment by using a PIV system. The PIV data generally agreed well with the simulation results using a simplified model of a person. In summary, the results showed that higher levels of temperature stratification have a significant effect on plume behavior.

C.Y.H. Chao et al. [34] measured expiration air jet flow velocities during coughing and speaking in close proximity to the mouths of volunteers by using PIV techniques. The average expiration air velocity was 11.7 m/s for coughing and 3.9 m/s for speaking.

Meg VanSciver et al. [35] measured the cough flow field produced by person subjects using PIV experiments. Fog generated by an evaporation type fog generator was used to seed the volume of the enclosure.

Soon-Bark Kwon et al. [36] studied the pathway of airborne pathogens by analyzing the initial velocity and the angle of exhaled airflow from the coughing and speaking of human subjects measured using a PIV system.

2.3 PIV for indoor airflows

2.3.1 Sub-scale model testing

Stephane B. Poussou et al. [37] performed PIV experiments using a 1:10 scale water-based model to investigate the effects of a moving human body on flow and contaminant transport inside an aircraft cabin. From the measurement results, a symmetric downwash flow was observed along the vertical centerline of the moving body in the case without a cabin environmental control system (ECS), while the evolution of this flow pattern was profoundly perturbed by the flow from the ECS.

M.Z.I. Bangalee et al. [38] studied the effect of the number of windows and the window configuration on natural cross-ventilation performance by performing PIV tests in the uniform flow field of a water channel to visualize the flow structure and measure the velocity vector fields. Spherical hollow glass particles of diameter 9-13 μm and density 1.1 g/cm^3 , uniformly fed into the isothermal flow, were used as tracer seeds in the PIV experiment.

P. Karava et al. [39] investigated wind-driven cross-ventilation flow characteristics by conducting PIV experiments for a sub-scale generic single-zone model in a wind tunnel. The results showed that indoor airflow patterns with cross-ventilation are complex and cannot be predicted by simplified macroscopic models such as the orifice equation. R. Ramponi and B. Blocken [40][33] used the results obtained from detailed wind tunnel experiments with PIV to validate the CFD simulation. The results showed a close qualitative agreement between the PIV measurements and the CFD simulation, both in the outdoor wind flow and indoor air flow.

V.A. Reyes et al. [42] studied the air flow distribution of natural ventilation in a 1:16 building-wind tower model by conducting PIV experiments in a wind tunnel. A dynamic similarity test between the real and the scaled model was investigated by numerical studies. Velocity data were obtained from several sections in order to reconstruct the whole distribution of the flow in the building-tower configuration, assuming a steady state.

M.V. Cruz-Salas et al. [43] performed flow velocity measurements in a water tunnel by using stereoscopic PIV to study the natural ventilation performance of a room with a windward window and different wind exchangers, as shown in Fig. 2-3. To reduce the thickness of the laser light sheet, a cylindrical lens made of a 6-inch diameter transparent acrylic tube, filled with water and sealed on both ends, was placed between the mirror and the bottom of the water channel test section. To reduce light reflections, a matte black adhesive paper mask was placed on the glass.

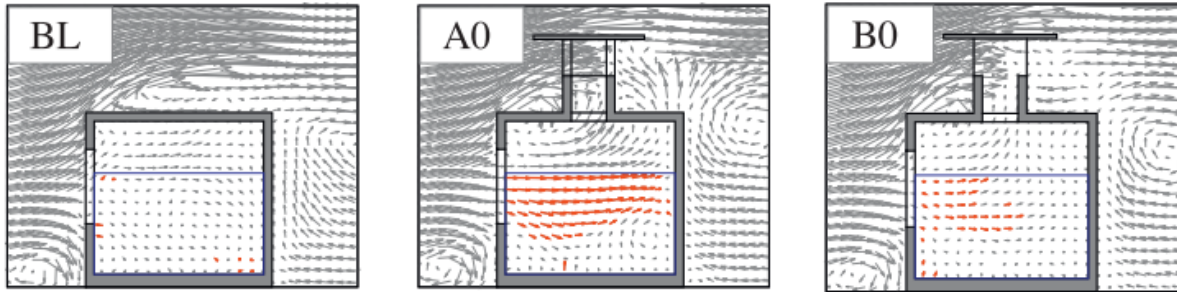


Figure 2-3. Average velocity field on the central plane for three cases.

T. van Hooff et al. [44] used PIV techniques to measure the airflow field of isothermal forced mixing ventilation driven by a transitional plane jet in a confined space. In this study, PIV was used to obtain the time-averaged velocity vector field, turbulence intensity, and vorticity to study the time-averaged flow field. Also, the instantaneous flow field was investigated by the analysis of instantaneous velocity vectors and vorticity structure with the Okubo-Weiss function Q criterion and Strouhal number.

J.D.Pisner et al. [45] studied the influence of obstacles on indoor air flow patterns produced by a mechanical ventilation system using PIV, LAD experimental methods, and Laminar, $k-\epsilon$ turbulence, and RNG $k-\epsilon$ turbulence numerical methods. The PIV measurements demonstrated a novel Bragg cell shuttering mechanism for the first time in an indoor airflow.

2.3.2 Full-scale model testing

Lingying Zhao et al. [46] carried out large-scale PIV measurements in a full-scale room with dimensions $5.5 \times 3.7 \times 2.4$ m under two typical ventilation schemes: cross-flow ventilation and return flow ventilation. Detailed experimental data and flow patterns were able to be obtained by a PIV system and used to validate numerical models and analyze ventilation strategies.

Xiaodong Cao et al. [47] performed large-scale PIV experiments to characterize the mixing air distributions inside a partially transparent aircraft cabin mockup by measuring the global flow field combined with five large sub-regions, each with a size of 975 mm \times 650 mm, as shown in Fig. 2-4. The distributions of velocity, vorticity, and turbulence intensity under the isothermal condition and cooling condition were obtained from PIV data and compared in detail. The results showed that the cabin airflows were of low velocities and high turbulence levels.

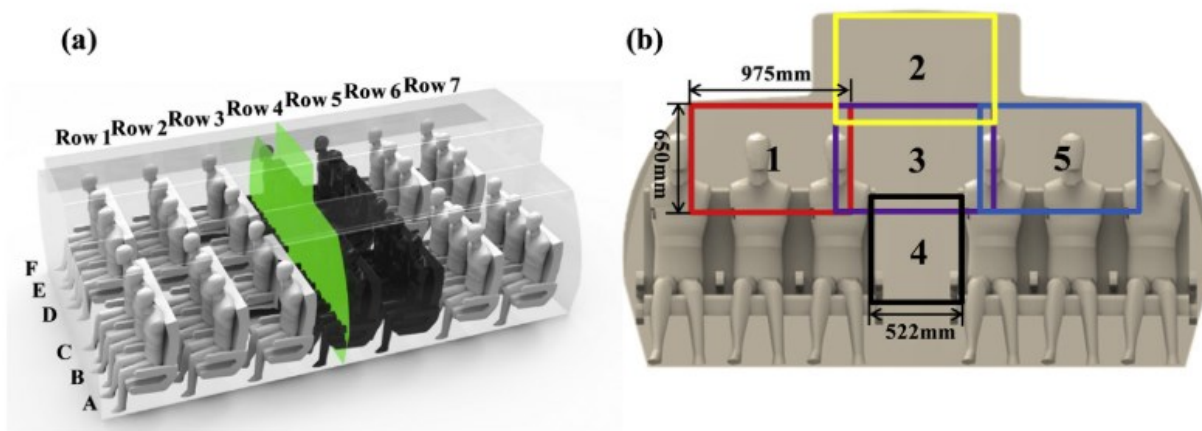


Figure 2-4. (a) Measured cross section of the cabin mockup; (b) Sub-regions in the measured cross section.

Gero Günther et al. [48] investigated the flow and heat transport in a generic aircraft passenger cabin and a sleeping bunk using PIV as well as thermography. Neutrally buoyant helium filled soap bubbles, which feature a high scattering efficiency, were used as tracer particles for the large scale PIV experiment with a rather high spatial resolution. Particle image velocimetry results were also used for validating numerical simulation results and achieved satisfactory agreement.

Yigang Sun et al. [49] developed a stereoscopic PIV (SPIV) system suitable for full-scale three-dimensional airflow measurement. An algorithm for SPIV in the particle streak mode is presented in this study.

Lone H. Mortensen et al. [50] conducted a PIV measurement in a full scale chamber with internal dimensions of $3.6 \times 4.5 \times 2.5 \text{ m}^3$ to investigate the airflow pattern in a gap between a cold wall and a piece of furniture. The results indicated that the flow rates behind the furniture would increase with an increased distance between the closet and the wall, and that even higher airflow rates were seen when the furniture was raised to a higher position.

Marcello Caciolo et al. [51] examined the characteristics of single-sided natural ventilation airflow generated by stack and wind effect under different outdoor conditions in a full scale building with several measurement techniques: two dimensional (2D) PIV, thermal anemometry, and the tracer gas technique. The PIV technique was used for flow visualization using smoke and velocity measurement on a vertical plane orthogonal to the opening in front of it.

Huawei Sun et al. [52] used PIV data to evaluate a RNG k- ϵ model of airflow in a full-scale test room with different inlet Reynolds numbers of 2,300, 5,500, and 16,000.

Mohammad H.Hoshi and Byron W.Jones [53] studied the airflow characteristics around a standing person in a simple large-scale room under realistic and well-documented environmental conditions by conducting PIV experiments on a total of 14 measuring planes.

2.4 PIV for outdoor airflows

Kyung Chun Kim et al. [54] investigated the flow characteristics around a three-dimensional rectangular prismatic building by using PIV techniques. In this study, PIV measurements were able to reveal detailed flow structures such as local eddy structures and correctly estimate critical dimensions such as the location of reattached points. The mean velocity field and turbulent kinetic energy could be obtained from instantaneous PIV velocity data, and the results could be used for verification of CFD models and to provide turbulent boundary layer conditions.

Zifeng Yang et al. [55] conducted PIV experiments to quantify the characteristics of wake vortex and turbulent flow structures around a high-rise building model in tornado-like winds. The PIV measurement results revealed clearly that a tornado-like vortex is a very complex, highly turbulent, three-dimensional vortex flow and the wake vortex and flow structures around the test model were found to become quite unsymmetrical in the face of the approaching flow. Three-dimensional views of tornado-like wind and vortex structures around the building model could be reconstructed based on the PIV measurement data at different elevation planes, as shown in Fig. 2-5.

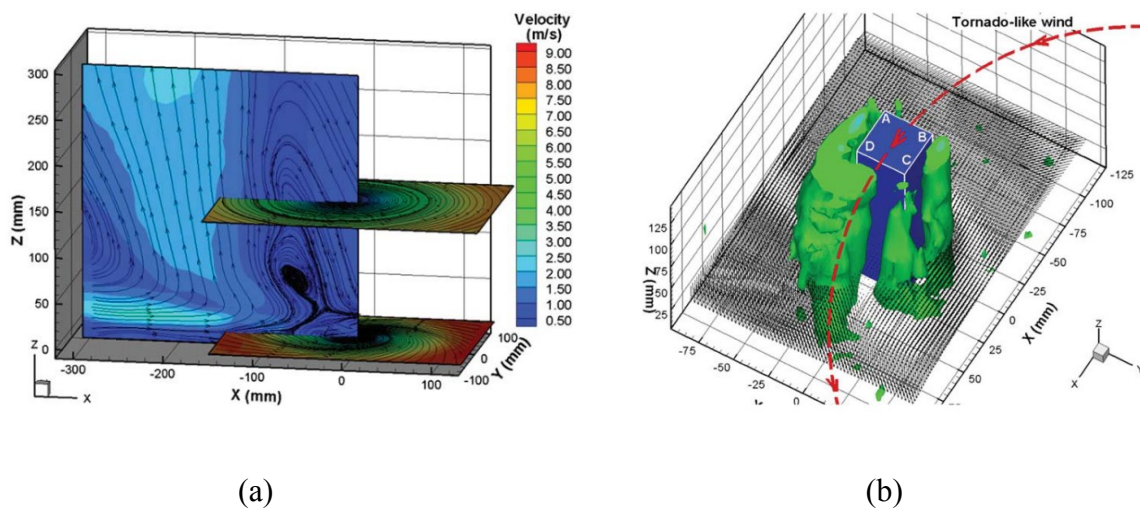


Figure 2-5. (a) The perspective view of the tornado-like vortex. (b) Reconstructed 3-D views of vortex structure around the test model.

Jonas Allegrini et al. [56] carried out PIV measurements in wind tunnel at different Reynolds numbers (9,000-30,700) and different leeward walls, windward walls, and ground temperatures (70-130 °C) to study the influence of buoyancy on flow in a scaled urban street canyon with heated surfaces. The velocity and turbulent kinetic energy fields were obtained and analysis was carried out with the PIV system.

Peng-Yi Cui et al. [57] studied the basic phenomena of air flow, heat, and mass transfer passing through different scale urban areas (street scale model and indoor scale model) with a scale ratio of 1:100 using several experimental methods: PIV, T-type thermocouples, and a SF6 quantitative detector. The PIV measurement results showed that for the investigation of mixed convection in the street canyon wind tunnel, if the value of the Reynolds number is in the range of Reynolds-independence determined by forced boundary layer flow, the only criterion for the flow pattern of the external flow is the Richardson number.

Yoshihide Tominaga et al. [58] employed the PIV technique to obtain the instantaneous and time-averaged flow field around an isolated gable-roof building model with a roof pitch. The PIV results of time-averaged velocity distributions were compared with the results obtained by a split fiber probe. Both results were acceptably in agreement except for the wake region behind the building.

Yan Zhang et al. [59] used the PIV technique to quantify the turbulent flow characteristics of microburst-like wind and investigate the flow structure interactions of gable-roof buildings in microburst-like wind. In order to ensure a reasonable spatial resolution of the PIV measurements, 14 different measurement windows were combined to reveal the global features of the microburst-like wind.

2.5 PIV errors and uncertainties

Although PIV can achieve relatively high accuracy in experimental results, there are errors and uncertainties that are hard to avoid because of the experimental conditions and the processing methods. One of the challenges in the application of PIV is determining errors and uncertainties.

As PIV measurements can be seen as a chain of error-producing steps [60], it is hard to estimate the displacement error that is an initial uncertainty source for PIV applications. At the beginning of the process, deviations between the measured velocities and real velocities are directly determined by the density, size, mass, and shape of the tracer particles. Then, the image acquisition quality may affect the accuracy of the results. After the acquired images are imported into the computer, the evaluation methods also produce errors. Moreover, the expertise of the researcher also influences the measurement accuracy. Overall, PIV measurement accuracy is a combination of a variety of aspects extending from the recording process all the way to the methods of evaluation.

Error types that may affect the measurement accuracy in the digital evaluation of PIV recording are discussed in a number of papers [13][63-66]. Generally, the errors consist of systematic errors and statistical errors [47]. Systematic errors include all errors related to the tracking behavior and seeding density of the particles, the random displacement error, the background noise, the size of the particle images, the correlation method, and so on. The main statistical error associated with PIV measurements is the random sampling error. However, it is not always easy to completely separate the systematic errors from the statistic errors. Therefore, in practice, the total error is normally expressed as the sum of a bias error and a random error or measurement uncertainty root-mean-square (RMS) error. H Huang et al. [61] summarized the major errors in two-dimensional digital particle image velocimetry as the outliers, the mean bias, and RMS errors. Outliers are the

invalid velocity vectors resulting from poor correlations. Mean bias errors are affected by inadequate pixel resolution and the numerical algorithm for computing the centroid. Root-mean-square errors, which reflect the deviation of the particle displacements from their mean values, arise due to improper particle seeding, strong velocity gradients, and three-dimensional flow movement. A. K. Prasad et al. [63] discussed two kinds of error encountered in PIV interrogation: mean bias error and random error. They concluded that mean bias errors arise when the particle image diameter is smaller than the pixel size due to the finite numerical resolution of the correlation function. Conversely, when the particle image size is larger, the random errors will become significant.

It is complicated to assess each kind of error quantitatively. Conclusions can be made about the overall accuracy of PIV measurements in building environment studies. In an investigation of turbulence air flow behavior of an attached plane jet discharged from an active chilled beam in a room, Guangyu Cao et al. [20][21] discussed about how the particle seeding distribution concentration, PIV interrogation windows, and spatial resolution may affect the measurements. The PIV results were validated using conventional anemometers, which showed that the difference between the results obtained by the anemometer versus PIV was up to 14% for the jet slot velocities. The difference in results between measurement methods for high turbulence intensity jet flow was larger than 20% in the inner layer and outer layer, especially at high supply jet velocity, while the measured maximum jet velocities were closer, with less than a 20% difference. Jiayu Li et al. [64] discussed the relationship between the normalized root-mean-square deviation (NRMSD) of the time-averaged velocity and the turbulence kinetic energy (TKE) and the sampling quantity when conducting PIV measurements. The results showed that 1,000 samples were sufficient to minimize the statistical error for large-scale PIV measurements.

Amina Meslem et al. [21] estimated PIV displacement errors by using the theoretical analysis of Westerweel [65]. The results showed that the maximal displacement error for the 2D PIV measurements was 1.4% for both the longitudinal and vertical directions. The accuracy of the vorticity field was assessed by the method proposed by Fouras and Soria [66], which depends on the spatial resolution of the velocity vector fields. The results showed that the absolute value of the bias vorticity error was 1.2%, and the random vorticity error was estimated at about 3.5% at the 95% confidence level. Also, the estimated error for the turbulent kinetic energy was estimated at about 3.6%. An accuracy of 5% to 10% is estimated for the measurements using the two-component technique, as mentioned in a study by Yigang Sun and Yuanhui Zhang [10].

3 PIV METHODOLOGY AND APPLICATION CASES

This chapter aims to provide information on hardware, software, and algorithms for PIV systems and measurement procedures.

3.1 PIV system components

The invention and development of PIV application in experimental fluid mechanics has been a topic of study since 1991 [67]. Overall, PIV is a technique to achieve quantitative measurement of instantaneous turbulent fluid flow velocity fields. Particle image velocimetry measures the velocity vector of an entire flow field at a given point in time by acquiring and processing images of tracer seed movements. The movement of tracer seeds represents the flow movement. The basic principle of this technique is based on the idea that the speed of particle seed movement is equal to the displacement divided by the time interval. The typical experimental setup of a PIV system consists of several sub-systems. The particles in the fluid are illuminated by a sheet of light at least twice within a time interval. The light scattered by the particles is recorded on a double frame by a digital camera, which is located at a 90° angle to the light sheet. Then, the images are transferred to a computer that can handle the great amount of data for automatic analysis. The displacement of the particles between light pulses is determined by the computer. Further analysis and post-processing for the acquired images is also required. Fig. 3-1 shows a typical setup for a PIV experiment in a wind tunnel [13]. As we can see in the figure, tracing seeds that are released into the flow field are illuminated twice by a multi-pulsed laser system. The light scattered by the tracer particles is recorded through an image recording system synchronized with the laser system. Then, the output data of the digital camera is transferred to the computer, which is used for controlling the system and for further data analysis. For evaluation, the recorded PIV images are divided into small

subareas called interrogation areas. The local displacement vectors for the images of the tracer particles between the first and second pulses are determined for each interrogation area by statistical methods. The velocity vectors are calculated by the displacement, taking into account the time delay.

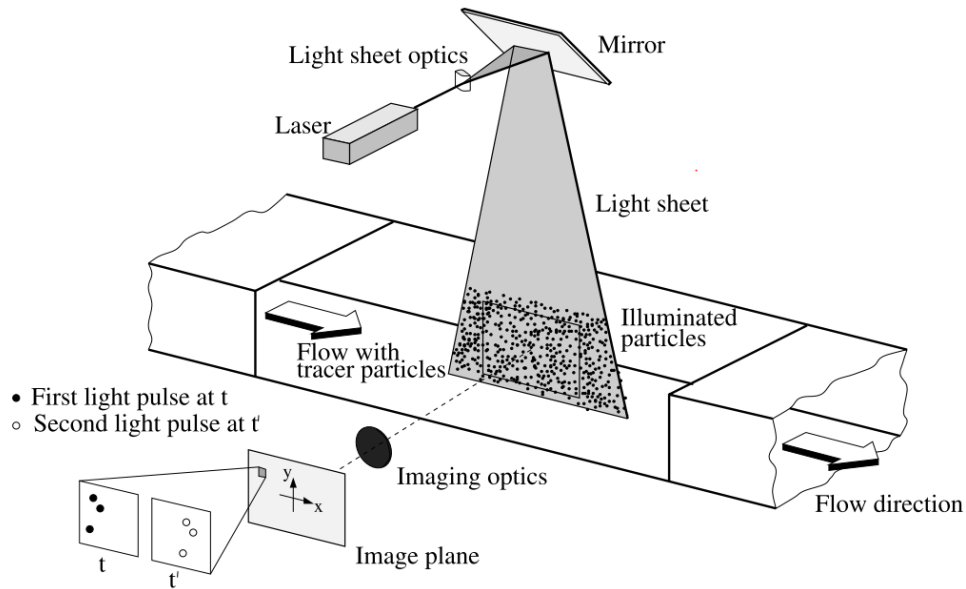


Figure 3-1. Schematic of a 2D PIV measurement system in a wind tunnel [13].

3.1.1 Illumination system

The function of the illumination system is to visualize the particle seeds in the flow field to allow the camera to record clear images of the particles and prevent the particles outside the measurement volume from forming noise. The most widely used illumination system for the indoor airflow measurements is the double-pulsed Nd:YAG laser system with an articulated delivery arm to generate a green light sheet of 532 nm wavelength [7][10]. The same laser used in the PIV study is shown in Fig. 3-2 [112]. An optics cylindrical lens was equipped on the laser to adjust the thickness of the light sheet and the light generation angle. The thickness of the laser sheet in the

measurement area is normally about 1-3 mm [10]. It is important to keep a relatively thin light sheet on the camera focus plane to guarantee high quality particle movement images. Nevertheless, in a strong three-dimensional flow field, particles captured in the first frame taken by the camera may move out of the measurement field and cannot be seen by the camera in the second pulse if the laser sheet is too thin. To avoid this error, the light sheet should be oriented parallel to the direction of flow concerned.



Figure 3-2. Double-pulsed Nd:YAG laser system [112].

The time delay between the pulses, Δt , is another important parameter for PIV illumination systems, because it needs to be long enough to capture the displacement of the tracer particles and short enough to keep the displacement inside the interrogation area between the subsequent illuminations. According to Guangyu Cao et al. [20,21], the separation of the particles, Δx , should be larger than the accuracy of peak detection and smaller than a quarter of the selected interrogation window size d_{int} , and expressed as:

$$pixel < \Delta x < \frac{1}{4} d_{int}. \quad \text{Eq. 3-1}$$

Then, the time interval Δt can be decided depending on the distance of particle movement and expected maximum flow field velocity U_{max} :

$$\frac{pixel}{U_{max}} < \Delta t = \frac{\Delta x}{U_{max}} < \frac{1}{4} \frac{d_{int}}{U_{max}}. \quad \text{Eq. 3-2}$$

3.1.2 Image recording devices

The most common image recording devices used in airflow measurements are coupled charged device (CCD) cameras and complementary metal oxide semiconductor (CMOS) cameras. For this study, a CCD camera (Dantec FlowSense EO) with a 1600 pixels \times 1200 pixels resolution was used for the PIV measurements. The technical specifications are shown in Table 1. The camera was equipped with a 60 mm lens, Nikon (60 mm F/2.8 AF NIKON), as shown in Fig. 3-3. The CCD camera was suitable for the small-scale flow that was the focus of this research. However, for future work, if large-scale measurements need to be conducted, a CCD camera with a high resolution is necessary for capturing the complete full-scale flow pattern.

Table 1. Technical specifications for CCD camera.

Camera	Speed (fps)	Res. (MP)	Sensor resolution (Pixel x Pixel)	Interframe time (ns)	Pixel size (μm)	Pixel depth
FlowSense EO 2M	35	2	1600 x 1200	200	7.4	8/10/12/14



Figure 3-3. FlowSense EO CCD camera.

3.1.3 Tracer particles

Tracer particles play a key role in indoor PIV measurements as the velocities of tracer particles are used to represent the real airflow velocities.

Generally, it is desirable that tracing particles should be non-toxic, non-corrosive, non-abrasive, non-volatile, and chemically inert. The seeds should be small enough to track the airflow movement but also large enough to scatter the laser light for image acquirement. The density of tracer particles is also crucial because an inappropriate density may cause errors of measurement.

First, the influence of gravitational forces can cause errors, especially in studying buoyancy driven flow considering that the densities of most widely used particles are much larger than the air density. The gravitationally induced velocity can be derived from Stokes' drag law [7]:

$$u_g = d_p^2 \frac{(\rho_p - \rho_f)}{18\mu} g, \quad \text{Eq. 3-3}$$

where g is the gravitational acceleration, ρ_f and μ are the density and dynamic viscosity of the air, and ρ_p and d_p are the density and diameter of the particles. From the equation, it can be seen that to achieve the relatively small velocity lag between the particles and airflow induced by gravitational effect, the diameter of the particles should be small enough and the densities of the seeds should be as close to the air density as possible.

Secondly, the initial velocity of the tracer seeds u_{p0} , when supplied into the airflow, can generate some perturbations in the original airflow field. The difference between particles velocity u_p and air velocity u_f is determined by the time t and the relaxation time of the particles τ_p :

$$u_f - u_p = u_g + (u_f - u_{p0} - u_g) \exp\left(-\frac{t}{\tau_p}\right). \quad \text{Eq. 3-4}$$

The relaxation time of the particles τ_p is expressed as:

$$\tau_p = d_p^2 \frac{\rho_p}{18\mu}. \quad \text{Eq. 3-5}$$

This indicates that the effect of the initial velocity of particles can be neglected when t is much larger than τ_p .

In addition, the scattering characteristics of seeds that determine the measuring area need to be considered. The cross section C_c , which is related to particle diameter and laser wavelength for spherical particles, can be used to quantify the scattering characteristics of seeds.

Table 2 shows the diameter and scattering cross section of the particles used in the experiments in this study. A balance should be found between the tracking behaviors and scattering characteristics when deciding the size of the seeds.

Table 2. Particle seeds diameter and scattering cross section.

Material	Particle diameter d_p (μm)	Scattering cross section C_c
Oil fog	1	$\approx 10^{-12} \text{m}^2$
Oil	1-2	$\approx 10^{-12} \text{m}^2$
Aluminum oxide (Al_2O_3) 96 g/mol	≤ 10	$\approx 10^{-9} \text{m}^2$

Fig. 3-4 shows the particle seeds used in the experiments and the corresponding generators. The aluminum oxide powder in Fig. 3-4 (a) was used in the experiments. During the experiments, the aluminum oxide powder was put in a mixing box and driven by high speed compressed air.

Fig. 3-4 (b) shows the atomization nozzle generator for the oil droplets. Pressurized air can be supplied into the generator by the hole on the side and draw up the liquid to produce air bubbles containing atomized droplets. The droplets are released into the airflow with the spray after the bubbles rise to the liquid's surface. The rate of generation can be controlled by the switch on the top of the generator. The supply rate of the atomizer is controllable and continuous, but it has a high pressure and high initial velocity, which should be considered in the experiments.

Fig. 3-4 (c) shows the fog fluid and generator used in the experiments. The fog machine drove the fog fluid into a heat exchanger. Then, the vaporized solution was discharged through the nozzle into the airflow. It was condensed into aerosol after mixing with the cool air. The discharging rate into the airflow was unstable and discontinuous, but with a lower initial velocity.



(a)

(b)

(c)

Figure 3-4. Tracer particles and generators: (a) aluminum oxide powder; (b) oil droplets and the associated generator; (c) fog fluid and fog machine.

3.2 Experimental procedure

3.2.1 Preparation

After preparing all the devices needed for the PIV system, including the camera, laser, computer, and tracer seeds based on the requirements, the testing model was designed for PIV measurements. For measuring the indoor flow, the enclosures of the field of view must be transparent so that the particles can be illuminated by the laser and the movement of the seeds can be recorded by the camera.

As shown in Fig. 3-5 (a) below, the airflow field of interest can be illuminated by the laser sheet through the transparent slot on the side wall of the chamber model. At the same time, the tracer particles' movement can be captured through the transparent façade.

The camera, laser, and model should be set up with high precision for accurate measurements. For the device setups, a water balance was used to help achieve the horizontal and vertical positions of the laser, camera, and model being tested. The camera and laser were placed with a high precision using a horizontal/vertical guide rail or a tripod for this research. Fig. 3-5 (b) shows the traverse used in the experimental study.

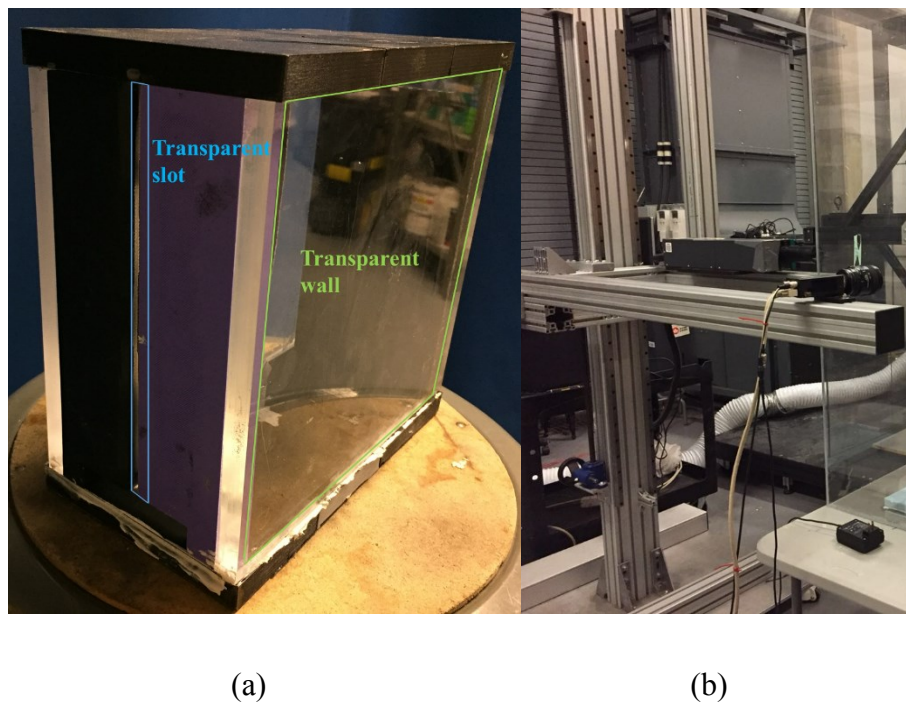


Figure 3-5. (a) Model designed for PIV experiments; (b) traverse used in PIV experiments.

3.2.2 Setup and calibration

Before adjusting the laser light sheet, goggles were worn to protect the eyes from green laser light.

The laser power was adjusted to the minimum required for light sheet alignment. Then, the optics

lens were rotated to generate the laser sheet in the measurement plane and the light sheet thickness was adjusted by moving the lens focus after turning on the laser. To achieve the appropriate laser sheet location and thickness, a piece of black paper was used in front of the laser sheet. For illuminating the particles, the laser sheet should be oriented overlapped to the plane of flow concerned. It is also important to select a suitable height for the light sheet and the distance between the laser optics and the field of view based on the size of the field of view. Finally, it is essential to check and minimize the reflection on the model's surface.

The digital camera should be located at a 90° angle to the light sheet so that the light scattered by the particles can be recorded. Calibration of the camera is essential for the PIV software, as the system must know the dimensional information of the measurement field. A target was put in the measurement field for the calibration. As shown in the Fig. 3-6, a standard ruler will normally be chosen as the calibration target. Then, the position or altitude of the camera as well as its focus was refined until a clear view of the ruler could be seen in the computer. Then, after the camera and laser sheet were properly aligned for acquiring pictures, an image of the calibration target in the field of view was recorded and saved. The scale factor, which indicates the proportional relation between real length in the physical world and how many pixels correspond to that length, was determined automatically based on the real length of the calibration ruler.

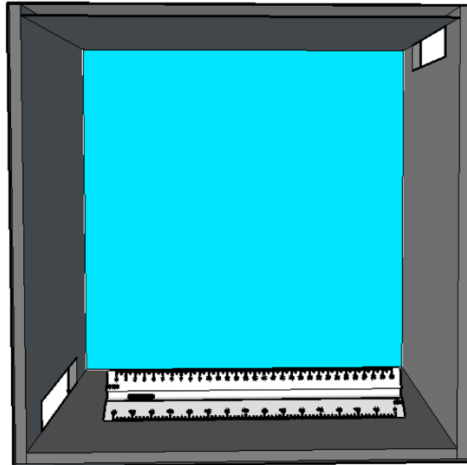


Figure 3-6. Calibration target.

3.2.3 Data acquisition

Before beginning data acquisition, flow visualization should be conducted before to check the particle tracking behaviors in the flow field. The power of the laser can be increased in small steps to keep the camera image from being saturated during the image visualization until the illuminated particles show the best definition. Generally, the seeds' concentration in the flow and the camera aperture focus should be adjusted to achieve optimal visualization. An extremely high concentration of particles with a poorly adjusted camera aperture may lead to a lower spatial resolution of the measurements [68]. Different photographs of the flow with seeded particles are displayed in Fig. 3-7 and show a comparison between different concentrations of particle seeds.

Also, the reflection on the model can be a huge source of error in the results, as shown in Fig. 3-8. Black tape or black paint can be used on the reflecting parts of the model according to the captured images.

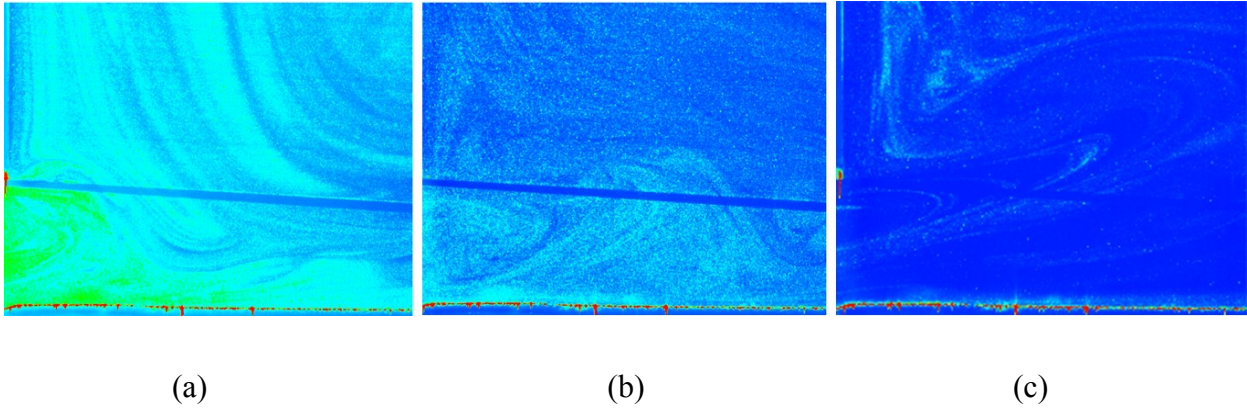


Figure 3-7. Photographs of the flow with seeded particles: (a) an excess of particles in the flow; (b) acceptable particle seeding; (c) insufficient particles in the flow.

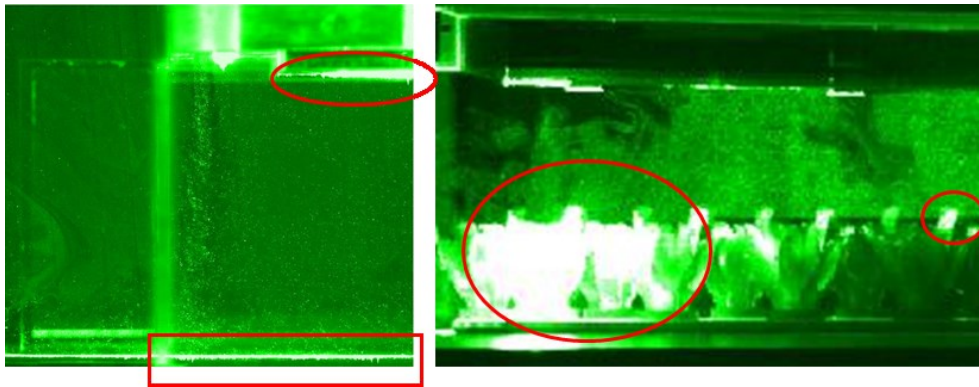


Figure 3-8. Reflection on the models.

Before capturing the images, several parameters were decided. The time interval discussed previously was checked in the images acquired in the preliminary test. As shown in Fig. 3-9, the separation of the particles should be about one quarter of the selected interrogation window size.

The trigger rate and number of images was set based on the application. Jiayu Li et al. discussed the relationship between the relative statistical error and the sampling quantity [64]. For our study, which considered the time-averaged flow, the number of captured images was decided by comparing the same flow analyzed using different number of captured frames. Then, the minimum

number of recordings that could present the time-averaged flow field was used for the experimental investigation.

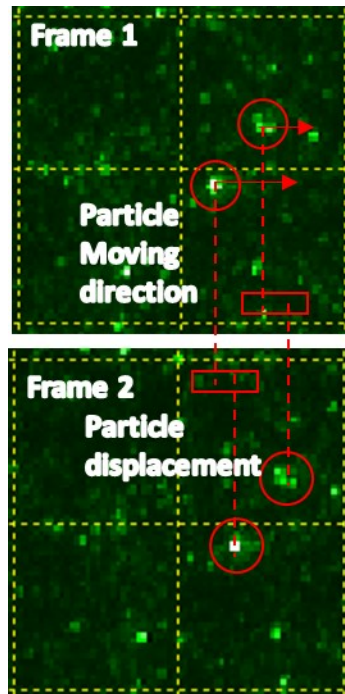


Figure 3-9. Photographs of particles separation between two frames.

3.2.4 Data processing

3.2.4.1 Pre-processing

The correlation signal of the data is strongly affected by the variation in image intensity. The non-uniform laser sheet, pulse-to-pulse variation, and so on could create noise in the correlation signal. Therefore, selecting the proper pre-processing method for the particle images is very necessary to removing the background noise in the images. There several common functions were used in this thesis.

ROI extract

This method can be used to extract a region of an image. This makes the time that it takes to process the images shorter.

Image masking

This method is used to mask the velocity vector field that is not of interest or has background noise out of the original acquired images. The vector fields that have been masked can then be hidden from the whole vector map and excluded from further analysis by simply tagging them with the status code “outside,” “disabled,” or “rejected” in the PIV software.

Fig. 3-10 below shows examples of image pre-processing.

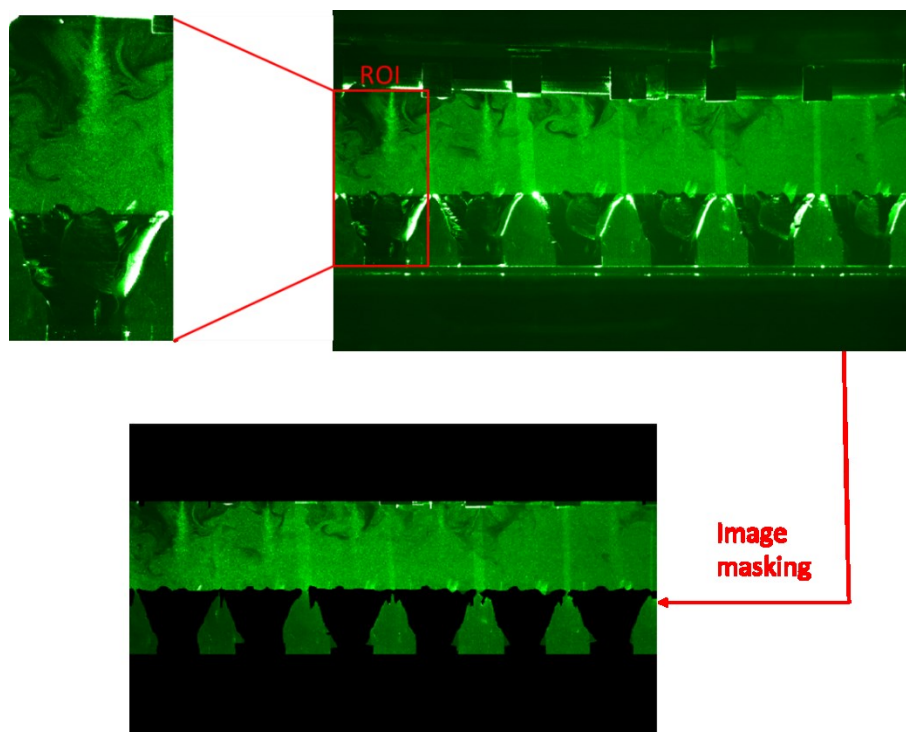


Figure 3-10. Pre-processing of PIV images.

3.2.4.2 Image evaluation

The digitized images were processed automatically using image processing programs. The main objective of the statistical evaluation of PIV recordings is to determine the displacement between the particle images in the two frames. There are varied evaluation methods for the PIV data. Fig. 3-11 shows the evaluation results using three different correlation methods.

Recently, the most widely-used evaluation method is adaptive correlation. The adaptive correlation method calculates velocity vectors with an initial interrogation area (IA) of size N time the size of the final IA, and uses the intermediary results as information for the next IA of smaller size, until the final IA size is reached [69]. The interrogation area is a sub-area in the recorded images used for further evaluation, and its dimensional settings directly determine the spatial resolution and accuracy of the measurements. According to the reviewed papers, the size of interrogation area is typically set to $32 \text{ pixels} \times 32 \text{ pixels}$ or $64 \text{ pixels} \times 64 \text{ pixels}$ with an overlap of 25% or 50%.

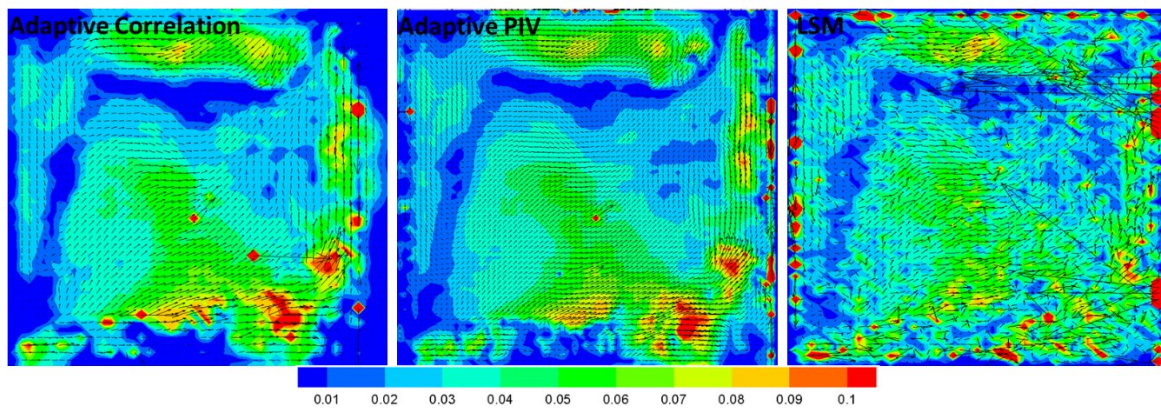


Figure 3-11. Image evaluation results

Another advanced automatic correlation algorithm is called adaptive PIV. The method will iteratively adjust the size and shape of the individual interrogation areas (IA) in order to adapt to local seeding densities and flow gradients [69]. Generally, a higher accuracy and resolution can be

achieved by adaptive PIV than adaptive correlation, but adaptive PIV is more time consuming and requires far more computing resources.

Two-dimensional (2D) least squares matching (LSM), a gray-level tracking technique, is another method for determining 2D velocity fields in highly seeded flows in air. In contrast with correlation based techniques, LSM performs translation, deformation, and rotation of the interrogation area [70], which helps to obtain more accurate calculation of the results. However, it has received much less attention due to its much longer computing times and the requirement of extremely high quality particle images.

Although adaptive PIV and LSM have many advantages, they are used less often in indoor PIV experiments [7]. For our studies, as shown in Fig. 3-11, similar results can be obtained through three different evaluation methods. As a result, adaptive correlation should be used with less computer resources and less time consuming.

Additionally, validation can be added to the correlation to fine tune the processing and remove spurious vectors. Peak validation can help identify invalid vectors, but is unable to produce an estimate of what the correct vector might be. Consequently, the invalidated vector will simply be substituted with zero, which in many cases can be quite far from the truth. Therefore the peak validation is always combined with a local neighborhood validation, which is based on neighboring vectors to obtain a realistic estimate of what the spurious vector should have been. Fig. 3-12 shows the results after peak and local neighborhood validation.

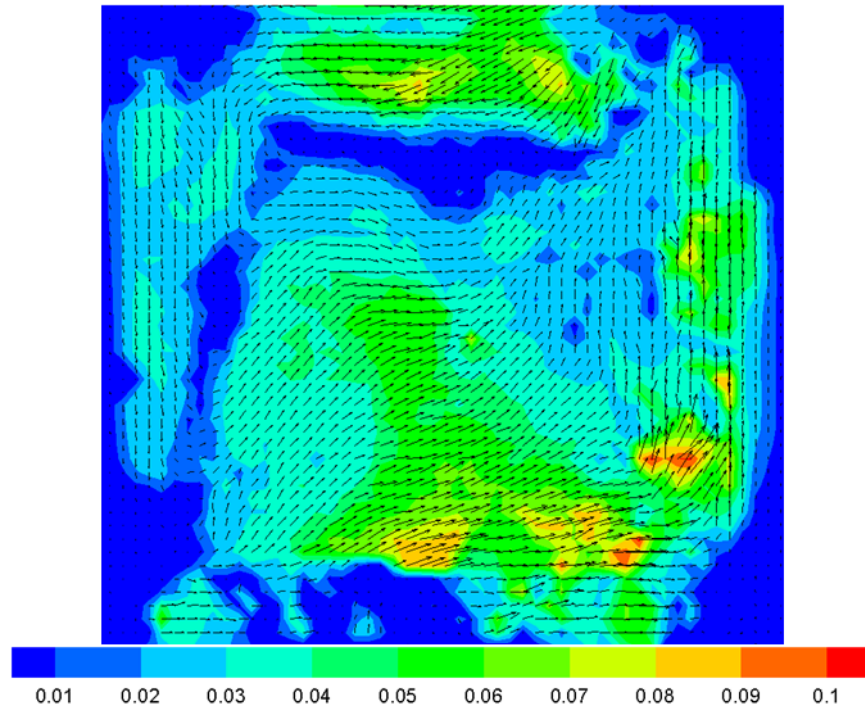


Figure 3-12. Image evaluation results with peak validation and local neighborhood validation.

After correlation, an average filter is always used to filter out vector maps by arithmetic averaging over vector neighbors. After that, there are still hundreds of velocity vector images, with which it is difficult to describe the fluid mechanical features. Techniques like time averaging, which is used in order to extract the information about the mean flow and its fluctuations; conditional sampling, which is used in order to distinguish between periodic and non-periodic parts of the flow; and vector field operators, like vorticity and divergence, used to detect structures in the flow are applied to reduce the amount of data [13]. The images evaluation procedure used in this PIV study is shown in Fig 3-13.

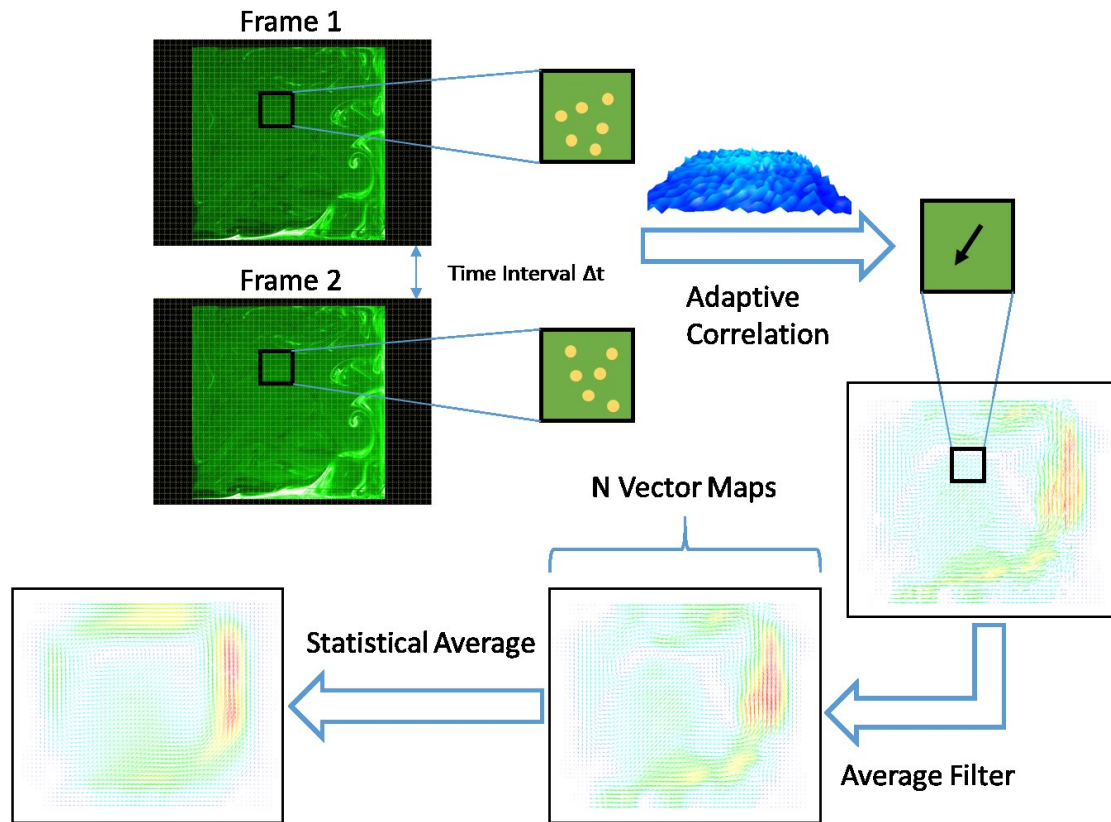


Figure 3-13. Schematic representation of the evaluation procedures of the PIV results.

3.2.4.3 Post-processing

It is obvious that the post-processing of PIV data is essential as more investigation is needed to describe the flow field characteristics. It is discussed in a book by Markus Raffel et al. [13] that the following steps are needed for post-processing of results after the evaluation and analysis of raw data. Uncertainties and errors in the raw data is needed to estimate the accuracy of PIV measurement. Analysis of the information is another challenging task in the PIV technique. To investigate the turbulence flow, more unsteady analysis techniques can be used for the post-processing of the PIV data, for example, spectrum analysis, wavelet analysis, proper orthogonal decomposition (POD), and stochastic estimation [71]. Additionally, other visualization and

analysis tools such as Tecplot can be used for the presentation and animation of the information to provide an easier way of understanding the features of the flow field. Fig. 3-14 shows examples of the post-processing of PIV results. Fig. 3-15 provides a flow chart of the entire methodology with the main steps of the PIV experiment.

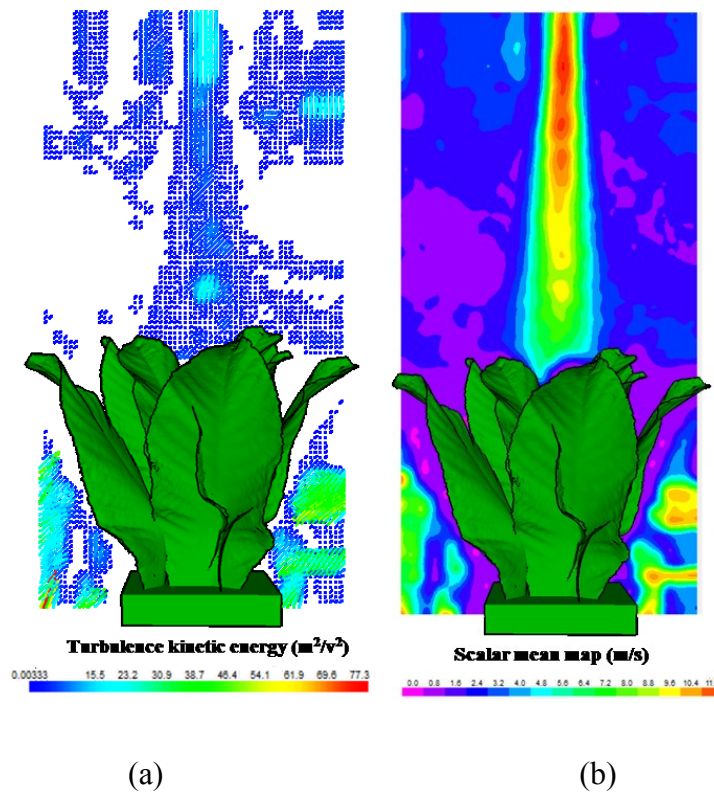


Figure 3-14. Examples of post-processing: (a) turbulence kinetic energy of the flow around the plant; (b) scalar mean map of the flow around the plant.

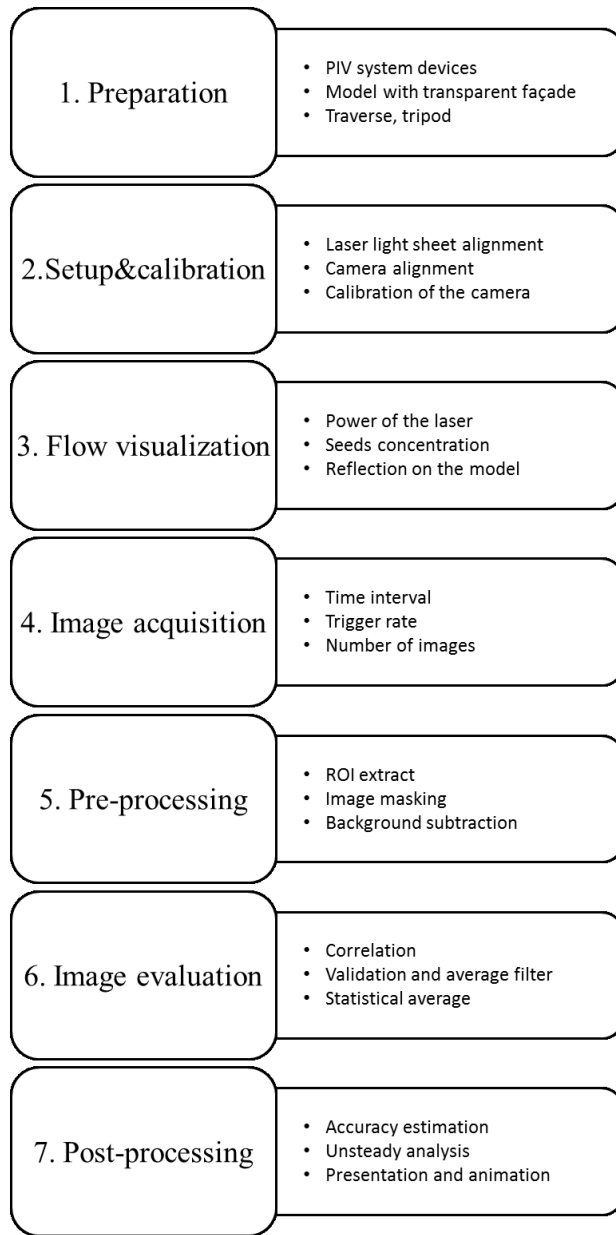
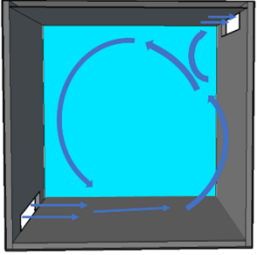
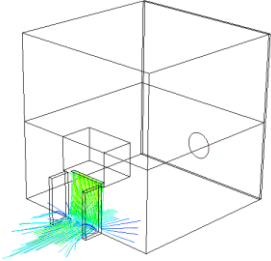
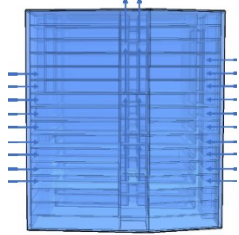
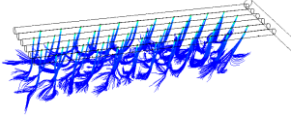


Figure 3-15. Flow chart of the main steps of the PIV experiment and associated critical parameters.

3.3 PIV application cases

To develop the whole PIV measurement and analysis procedure, research on four problems in the building field was conducted in the following chapters. The aim of this thesis was to apply the PIV technique in common building field problems. First, natural ventilation in a single-zone model was studied, as this is a relatively simple case and presents the basic common phenomenon of building ventilation. Based on this study, measurements of air flow rate of a high rise building model were conducted to investigate the natural and hybrid ventilation of a whole building under real weather conditions. As the basic principle of many ventilation devices and a common method of mechanical ventilation, jet flows were chosen to study experimentally. Air curtain performance in a wind tunnel was investigated as a common present of single jet flow. Based on this study, measurements of a multi-jet mechanical ventilation system in a warehouse were conducted using the PIV technique. Table 3 presents a summary of all the PIV experimental cases conducted. In total, 93 cases related to four problems were studied, which is explained in the following chapters. Each case's data was captured three times to insure the repeatability of the data measured. In total, 279 PIV experiments were conducted in order to investigate the application of PIV techniques of measurement and analysis in different building airflow field problems.

Table 3. PIV application cases

Case 1. Natural ventilation in single zone model (Chapter 4)							
Measurement plane	Complete indoor flow field			Opening on the bottom			
Insulation material	Wood	Foam	Wood	Foam			
Measurement time after heater on	15, 30, 60, 90 mins			15, 30, 60, 90 mins			
Measurement time after heater off	1, 25, 50 mins			1, 25, 50 mins			
Other conditions	Closed model without ventilation						
Total cases	29 cases						
Simulation cases	N/A						
Case 2. Air curtain interactive with wind (Chapter 5)							
Air Curtain Types	9.6 m/s, 0°	9.6 m/s, 20°	5.7 m/s, 0°	5.7 m/s, 20°	2 m/s, 0°	2 m/s, 20°	
Wind Speed	0, 4, 10 m/s	0, 4, 10 m/s	0, 4 m/s	0, 10 m/s	0, 10 m/s	0 m/s	
Wind Direction	0°, 60°	0°	0°	0°	0°	0°	
Infiltration	11 cases	9 cases	4 cases	2 cases	2 cases	1 case	
Other conditions	With people/ vestibular	With vestibular					
	6 cases	1 case					
Total cases	36 cases						
Simulation cases	50 CFD cases						
Case 3. Hybrid ventilation in high rise building model (Chapter 6)							
Ventilation conditions	Natural ventilation			Hybrid ventilation			
Floor number	4-13 floors			4-13 floors			
Total cases	20 cases						
Simulation cases	2 Multizone cases						
Case 4. Mechanical ventilation in large space warehouse (Chapter 7)							
Measurement plane	Flow field around 12 plants			Flow field around 6 plants			
Total air supply volume flow rate	3.4, 6.8, 13.6, 27.2 cfm						
Total cases	8 cases						
Simulation cases	2 CFD cases						

4 NATURAL VENTILATION IN SINGLE ZONE MODEL

4.1 Introduction

Natural ventilation is an effective method to reduce the energy consumption of buildings and improve air quality. Mechanical ventilation can also achieve indoor air comfort by using energy to obtain a desired ventilation rate and thermal stratification. However, this consumes large amounts of energy and produces greenhouse gas emissions. According to the investigation of Luis Perez-Lombard et al. [72], HVAC systems accounts for almost 50% of the energy consumption in buildings and approximately 10-20% of the total energy consumption in developed countries. It is desirable to study air flow movement and thermal stratification within an enclosure when the building is under natural ventilation conditions considering that natural ventilation performance relies solely on natural conditions and the design of the building.

When air inside of a room is of a different temperature than the outdoor air, pressure gradients across the openings between the indoors and the exterior difference are produced, caused by the air density difference. The temperature difference can be one of the factors driving the exchange of flow in natural ventilation. The ventilation rate depends on the strength and direction of the buoyancy force and the resistance of the flow path. As this process is complex and difficult to predict by theoretical models, experimental methods can be reliable tools for studying the ventilation flow characteristics and thermal distributions.

Considering the conditions in reality, the heat load can be assumed to come from a single or cluster of localized sources, such as an assembly of electronic equipment [73][74][75][76]. For other circumstances, the heat load can be modelled as a distributed source evenly scattered throughout the base of the room [80][81].

For this chapter, the present work is focused on the buoyancy-driven cross-ventilation of a single-zone room with a heated floor that is connected to a cold exterior by two openings.

4.2 Methodology

This investigation studied cross ventilation using experimental methods. The PIV technique was used for measuring the complex air flow inside the building model. Temperature variation was recorded using thermocouples. A tracer gas technique was applied to validate the PIV results.

4.2.1 Experimental design

A 1:50 scaled 3D printed model of the dimensions $20 \times 10 \times 20$ cm ($L \times W \times H$) was designed for this experimental study. There were two openings, each with the dimensions 7.5×1.5 cm ($L \times W$), located on the top and bottom of the model. For the visualization of the camera and shooting of the laser sheet, the façade of the model and part of the side wall was installed with transparent acrylic material as shown in the figure below. The distributed heat source was modelled with two electric bulbs (6W each), combined with a metal sheet above the heater for creating a constant uniform source of buoyancy. Two different insulation materials – wood and foam – were used in the experiment. Schematics of the sub-scale model are shown in Fig. 4-1. The temperatures of five points inside the chamber and the outdoor temperature were measured by thermocouples, and their locations are shown in Fig. 4-2. The temperature measuring points inside the chamber were all set in the middle plane of the indoor space, which was consistent with the PIV measuring plane.

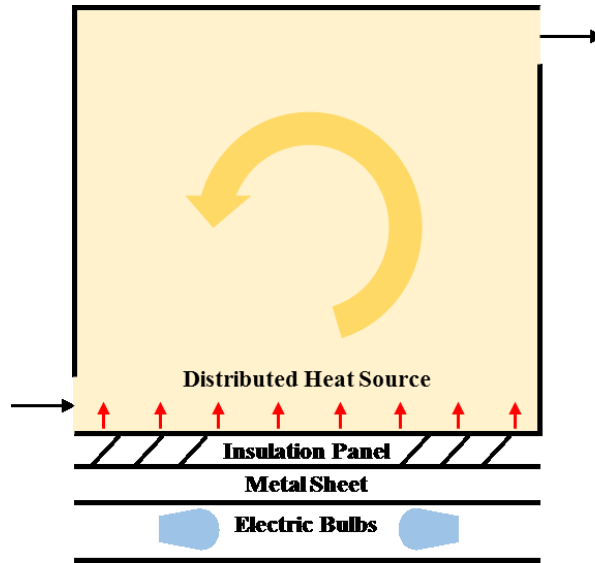


Figure 4-1. Schematics of the sub-scale model with heated floor.

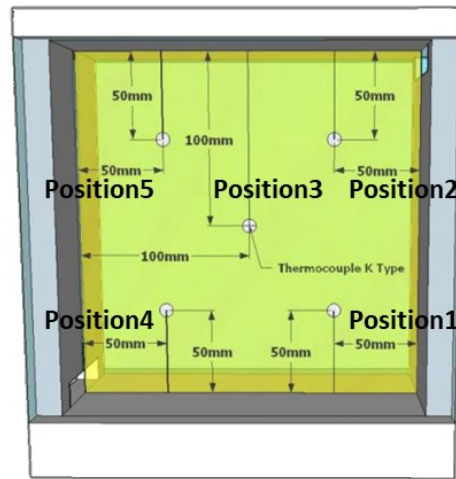


Figure 4-2. Schematics of the thermocouples' locations inside the chamber.

4.2.2 Particle image velocimetry measurement setup

To visualize the airflow fields in the experimental chamber, a 2D PIV system was used in the research. According to the pretest, two PIV measurement planes were set as shown in Fig. 4-3:

one measuring 285 mm by 212 mm ($W \times H$) for the whole field of view and one measuring 160 mm by 120 mm ($W \times H$) at the corner of the left opening. Based on the preliminary test, and considering that the air flow velocity at the opening is less than 0.15 m/s, different seeds were used in the experiment for different fields of view. For the first field-of-view tests, fog was used as tracing seeds. For the second smaller field-of-view tests, oil droplets were used as particle seeds to simulate the detail flow rate across the opening. Tracing seeds were supplied outside the chamber. It is important to note that it was necessary to supply the continually to achieve the required seeding density. However, this might have contributed to some measurement errors because of the initial velocity of the supplied seeds.

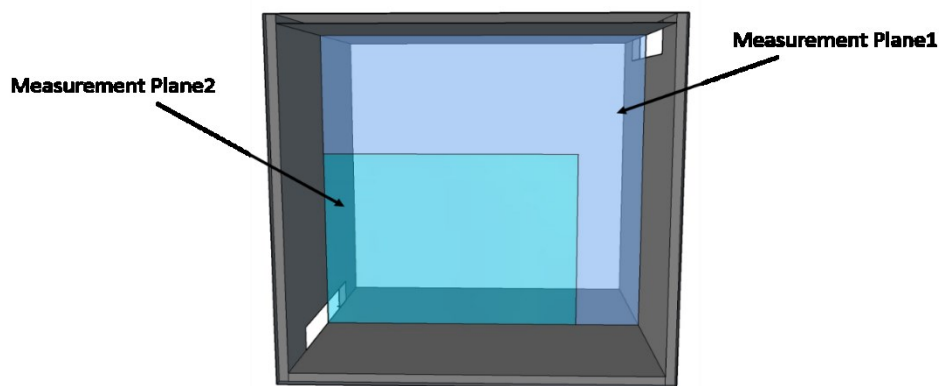


Figure 4-3. Area measured using PIV.

Based on the size of the seeds and the preliminary tests, the time interval between each pair of pictures, Δt , was set differently for the two measurement planes. For each PIV, 100 frame pairs (200 images) were captured. The interrogation area was selected to be 32×32 pixels. More details are shown in Table 4.

Table 4. Setup of PIV data acquisition and evaluation.

	Measurement Plane 1	Measurement Plane 2
Field of view	285 mm by 212 mm	160 mm by 120 mm
Delay time (Δt)	6,600 μ s	1,500 μ s
Sampling frequency	15 Hz	15 Hz
Number of captured pictures	100 frames	100 frames
Interrogation window	32 pixels by 32 pixels	32 pixels by 32 pixels
Overlap	25%	25%
Measured time	7 s	7 s

4.2.3 Tracer gas test setup

Tracer gas techniques are one of most common experimental measurement methods used in ventilation studies. In these techniques, a tracer gas is injected into the zone being studied and its concentration response is measured [79].

The ventilation rate through a building can be measured using tracer gas by one of three methods: tracer decay, constant tracer concentration, and constant tracer injection. For this study, tracer decay was chosen as the measurement method. Tracer decay consists of a short burst of gas being injected into the space to establish a constant concentration within the building. Then, injection is stopped and the concentration decay at a certain position is recorded. The equation is based on the mass balance of the tracer gas in the air:

$$V \cdot \frac{dC_i}{dt} + Q_r \cdot C_g(t) = \dot{m}, \quad \text{Eq. 4-1}$$

where V is the total volume of the ventilated space in m^3 , C_g is the concentration of tracer gas in kg/m^3 at time t , Q_r is the ventilation rate in m^3/s , and \dot{m} is the injection rate of tracer gas in kg/s inside the building volume. This equation neglects the background tracer gas concentration for gases not existing in the air.

Generally, there are two methods to calculate the ventilation rate from the tracer decay curve: the two-points decay method and the multi-points decay method. Because the space in the sub-scale model is limited and it is easy to get uniform well-mixed tracer gas, the two-point decay method can be used for this study. The two-point decay method uses an initial point $C(t_1)$ and a final point $C(t_2)$ of the decay curve to determine the air change rate:

$$Q = V \cdot \frac{\ln \frac{C(t_1)}{C(t_2)}}{t_2 - t_1} \quad \text{Eq. 4-2}$$

It is important to choose an appropriate tracer gas, which should satisfy the following requirements [79]: safe, non-reactive chemically or physically with the environment, and easily measurable. Moreover, the tracer gas should have a density similar to air so that it can mix well with indoor air. Also, it is better that the tracer gas is not one of the constituents of indoor air, so that the concentration of the gas existing in the air will not affect the experiment results.

Table 5 shows tracer gases that have been commonly used in other research since 20th century.

Table 5. Characteristics of tracer gases.

Tracer gas	Density compared to the air	Density compared to the air	Advantages	Disadvantages
Nitrous oxide (N ₂ O)	Demmers et al., 2000 [80]	1.53	Low cost Density relatively close to that of air	Interference with H ₂ O and CO ₂ Toxic at low concentration levels
Carbon dioxide (CO ₂)	S. Van Buggenhout et al., 2009 [81]	1.53	Easily available: very low cost Density relatively close to the air Non-toxic	High greenhouse effect Exists in the air
	Shuqing Cui et al., 2015 [79]			
	Xin et al., 2009 [82]			
	Hwataik Han et al., 2011 [83]			
Sulphur hexafluoride (SF ₆)	Snell et al., 2003 [84]	5.11	Not present in the air Not harmful to human beings	Very heavy Expensive
	Marcello et al., 2011 [51]			
Krypton ⁸⁵ (⁸⁵ Kr)	Alaa Kiwan et al., 2013 [85]	2.93	1 ppm in the air	Heavy Expensive
	M.Samer et al., 2011 [86]			

In this research, CO₂ was chosen as the tracer gas since it can be easily obtained and measured. Also, a high accuracy of the concentration measurements is available given calibration with the background concentration of CO₂.



Figure 4-4. High pressure gas analyzer UGA 100.

The Universal Gas Analyzer (UGA) 100, a mass spectrometer product from Stanford Research Systems (SRS), was used for the measurement of CO₂ concentrations, as shown in Fig. 4-4. The three measuring points at different locations inside the chamber are shown in Fig. 4-5. Considering the small space inside the chamber, three measuring points were enough to ensure the accurate idea of well-mixed environment of the tracer gas before the decay.

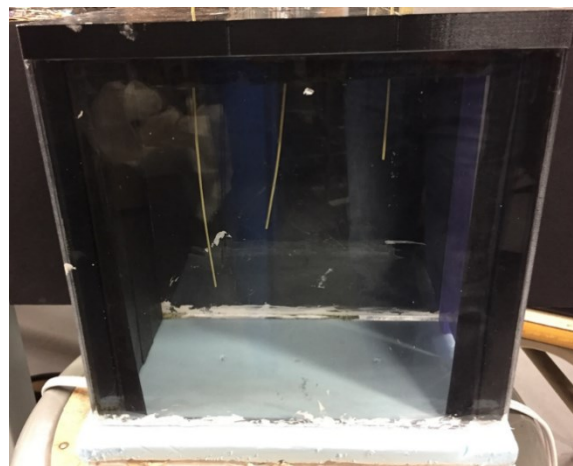


Figure 4-5. Tracer gas measurement setup.

4.3 Results and discussions

4.3.1 Preliminary test and test plan

Fig. 4-6 and Fig. 4-7 show the flow velocity vectors and streamlines inside the model combined with the four measurement planes. The PIV results of the buoyancy-driven flow were obtained under the same conditions in one measurement plane. Comparing the results in Fig. 4-8, it was seen that the flow patterns were similar in the upper parts of the chamber model. A significant difference can be observed at the lower part of the flow field, as the PIV result captured by one measurement plane could not show the high velocity of inflows. As the result, to obtain complete and accurate information on the indoor buoyancy flow, at least two planes of results must be captured with the PIV technique.

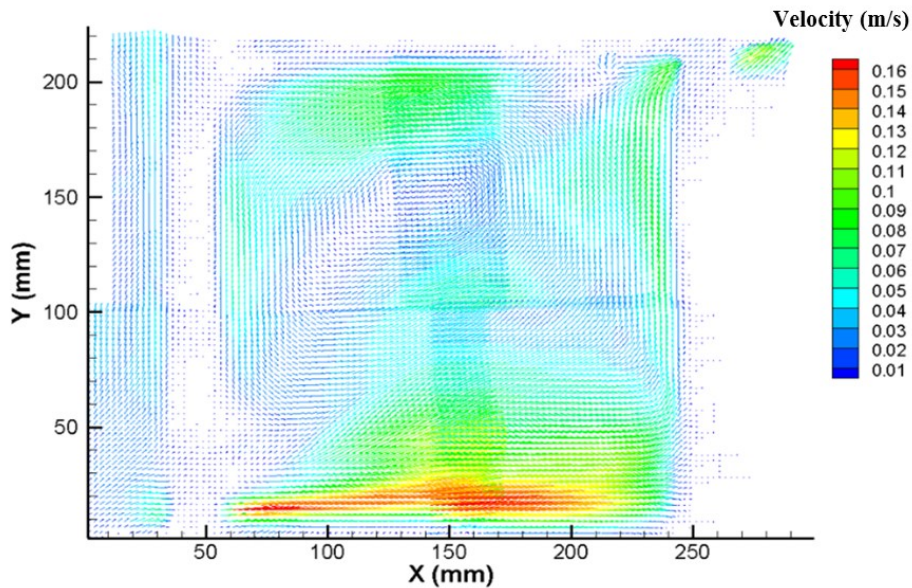


Figure 4-6. Indoor flow field velocity vectors combined with the PIV results of the four planes.

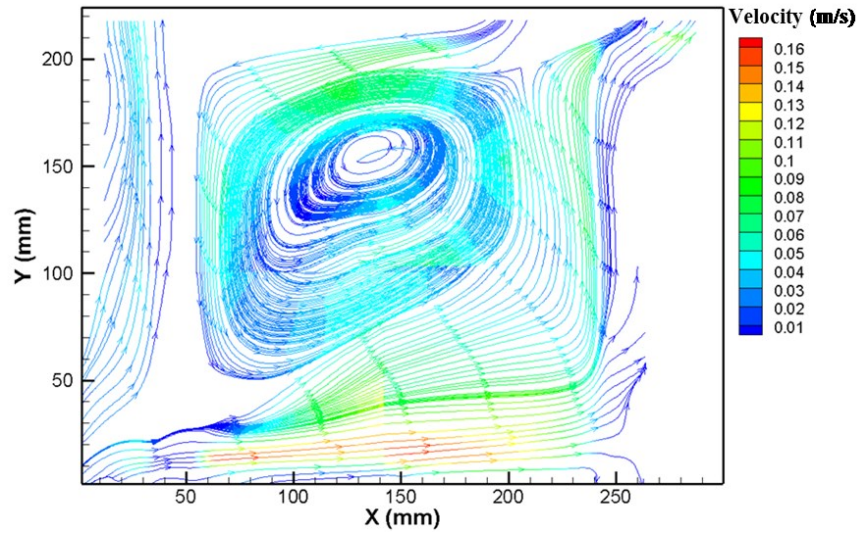


Figure 4-7. Indoor flow field velocity streamlines combined with the PIV results of the four planes.

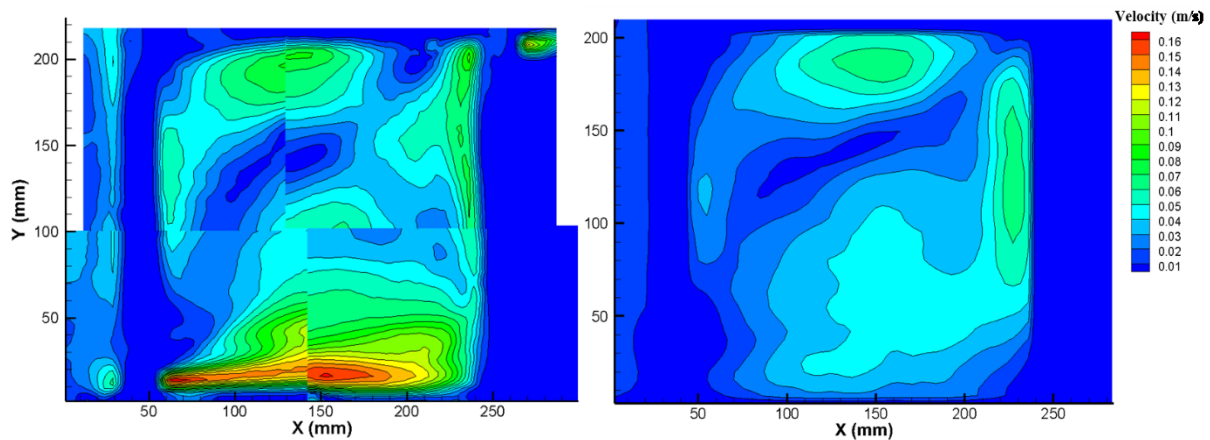


Figure 4-8. Comparison of the velocity contour captured by the four measurement planes versus one measurement plane.

As shown in Fig. 4-9, the temperature variation over time at different positions was measured by thermocouple tests. It can be seen that the outdoor temperature remains stable at about 24 °C, so that the PIV experiments conducted during the entire time period can be considered to have been done under the same exterior temperature conditions. Also, the results show that after about 90

minutes (5,400 seconds), the average temperature change of all five points inside of the chamber was less than 1%, which can be considered to indicate that a steady state of the indoor flow field was reached. Considering the temperature measurement results, the PIV experiments plan was made as shown in Table 3. It can be seen that after turning on the heater, PIV experiments were carried out at 15 mins, 30 mins, 60 mins, and 90 mins to capture the unsteady state flow variation. To investigate the air movement under the power failure condition, three PIV tests were conducted 1 mins, 25 mins, and 50 mins after turning off the heater. Additionally, the indoor flow field of the single-zone model without openings was also studied using the PIV experimental method to compare the natural ventilation effect to the flow movement. The test of air movement in a closed room model was conducted under relatively steady-state conditions (90 mins after turning on heater).

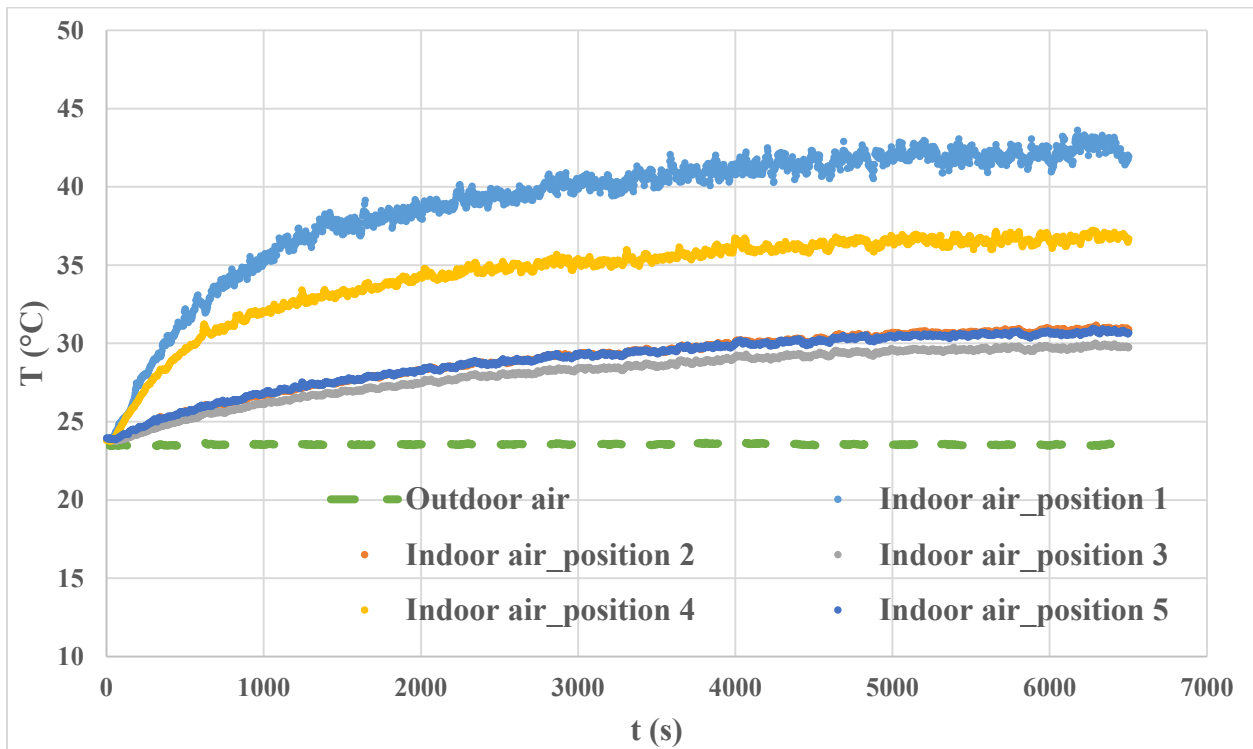


Figure 4-9. Temperature changes after heaters were turned on.

4.3.2 Airflow validation with tracer gas measurement

A tracer gas decay experiment was carried out to validate the airflow rate results obtained by the PIV data. The mean ventilation rate calculated according to the decay curve shown in Fig. 4-10 were about $0.000338 \text{ m}^3/\text{s}$, while the air flow rate obtained from the PIV measurement results in Fig. 4-11 was about $0.000383 \text{ m}^3/\text{s}$. The difference between the results measured by PIV and tracer gas decay is about 11.78%, which is acceptable.

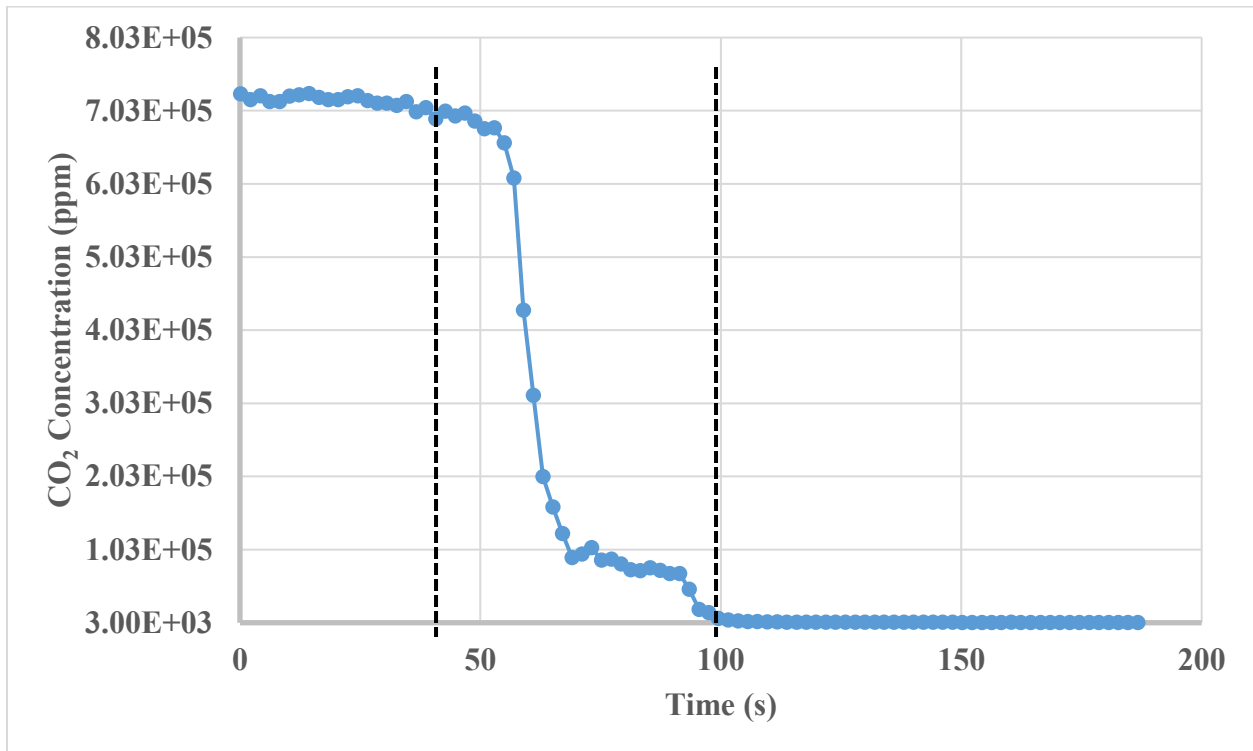


Figure 4-10. CO₂ concentration changes in tracer gas measurement (airflow rate $0.000338 \text{ m}^3/\text{s}$).

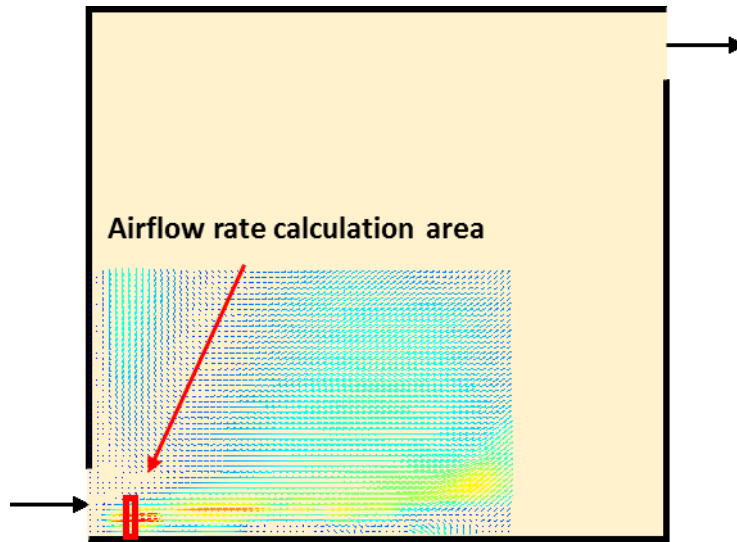


Figure 4-11. Schematic view of airflow rate calculation method using PIV results.

4.3.3 Indoor flow without ventilation

To compare the effect of natural ventilation with the effect of no ventilation in the building model, the steady (90 mins after turning on the heater) indoor flow field when the two openings in the model were closed and heater was on was measured. As shown in Fig. 4-12, a plume rose from the floor and formed two vortices in the upper part of the building model. A relatively high velocity flow was closer to the ceiling, which caused an entrainment between the floor and ceiling. For indoor environment comfort, it is better to promote ventilation at the height where people are present. Considering the human scale of about 1.8 m in height when standing [87], the zone for people in this scaled model is about 36 mm above the floor. As a result, natural ventilation is essential for increasing ventilation performance in the lower part of the building model.

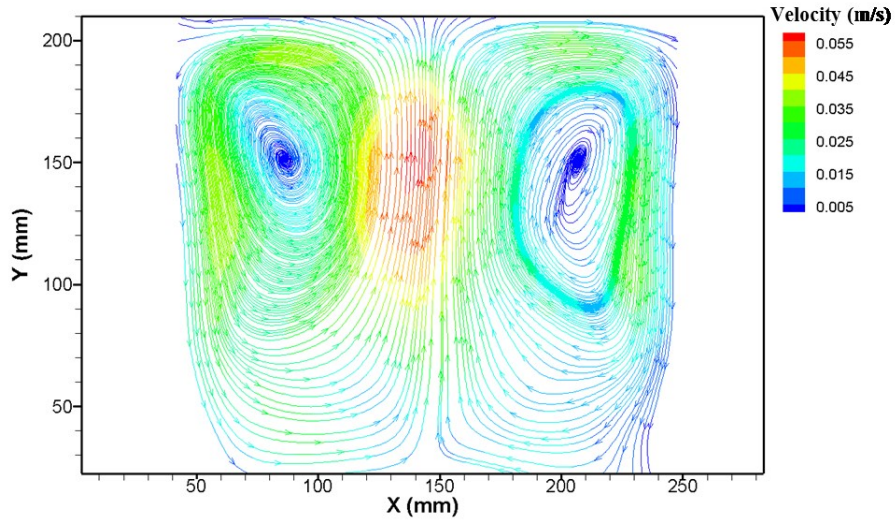
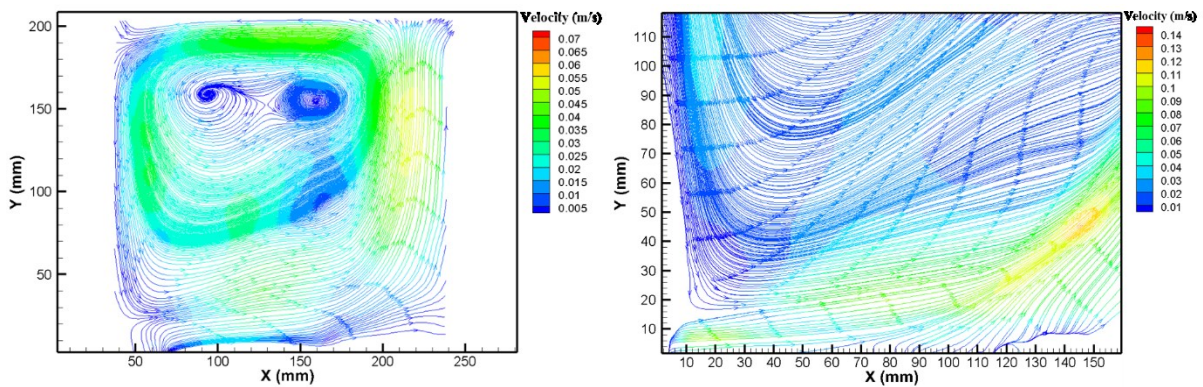


Figure 4-12. Indoor flow field streamlines without ventilation.

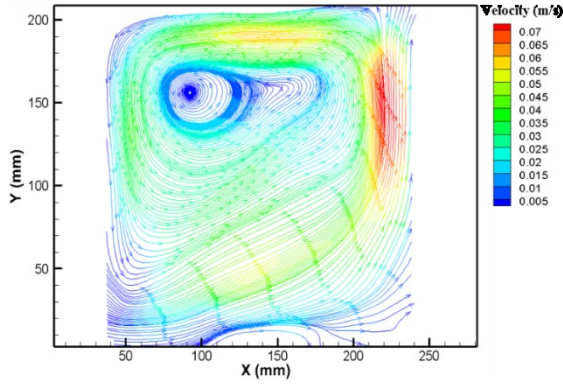
4.3.4 Indoor flow with natural ventilation

The indoor flow field velocity and temperature with natural ventilation was measured using PIV and thermocouples at 15, 30, 60, and 90 minutes after turning on the heater. For simulating the condition that there is as electricity interruption and all indoor heat sources are turned off, flow field and temperature distribution after the heater was off for 1, 25, and 50 minutes was captured. Two insulation materials – wood and foam – were used in the experiments.

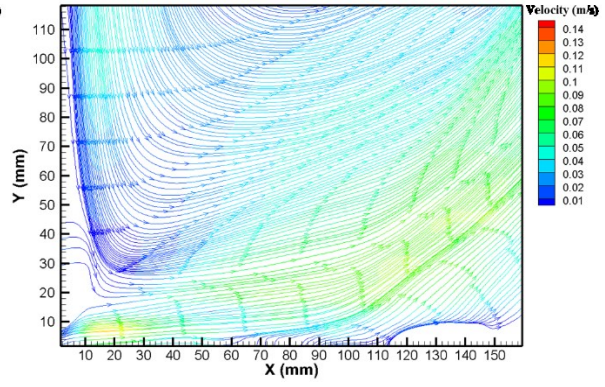


(a) 15 min after heater on, plane 1

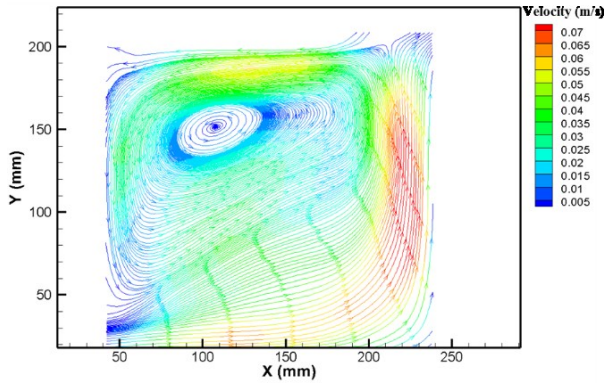
(b) 15 min after heater on, plane 2



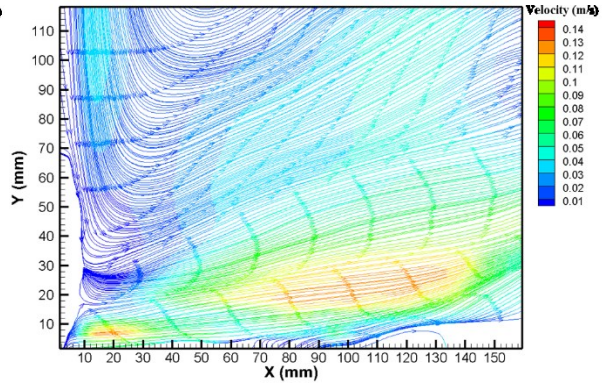
(c) 30 min after heater on, plane 1



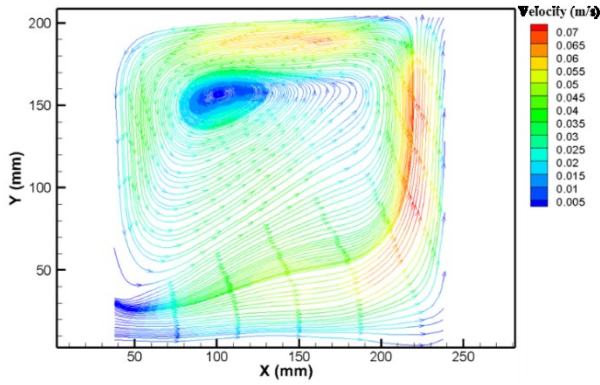
(d) 30 min after heater on, plane 2



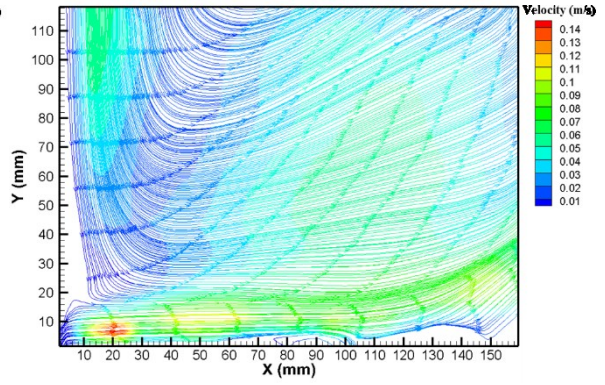
(e) 60 min after heater on, plane 1



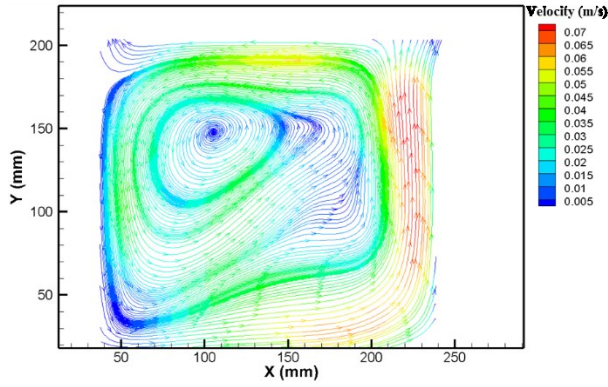
(f) 60 min after heater on, plane 2



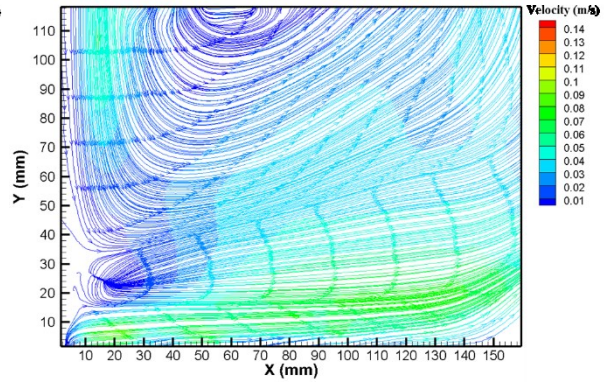
(g) 90 min after heater on, plane 1



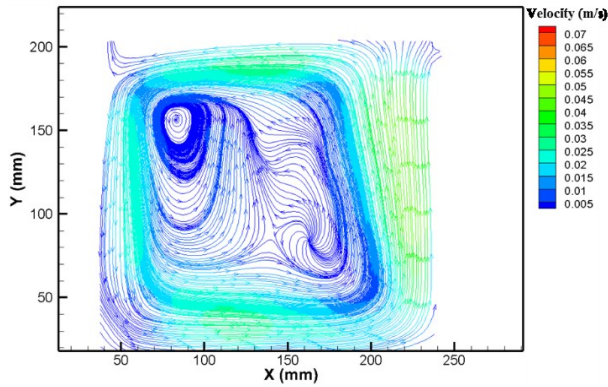
(h) 90 min after heater on, plane 2



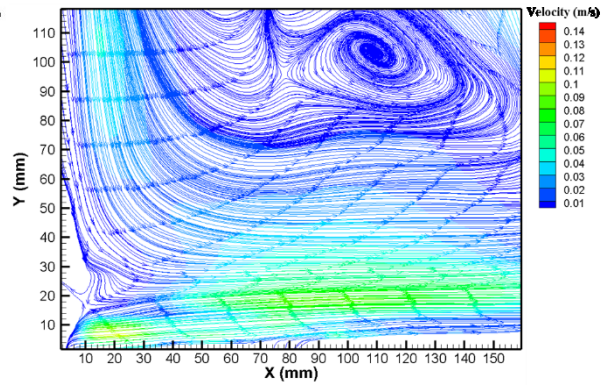
(i) 1 min after heater off, plane 1



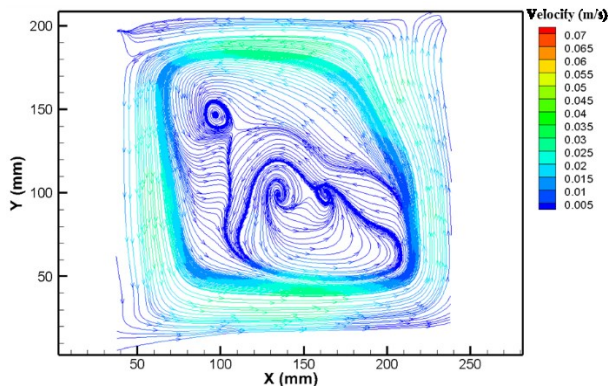
(j) 1 min after heater off, plane 2



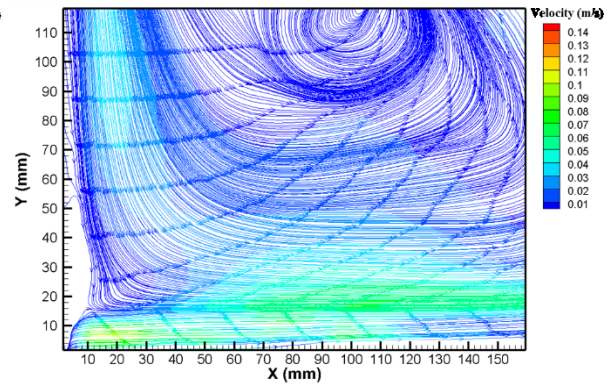
(k) 25 min after heater off, plane 1



(l) 25 min after heater off, plane 2



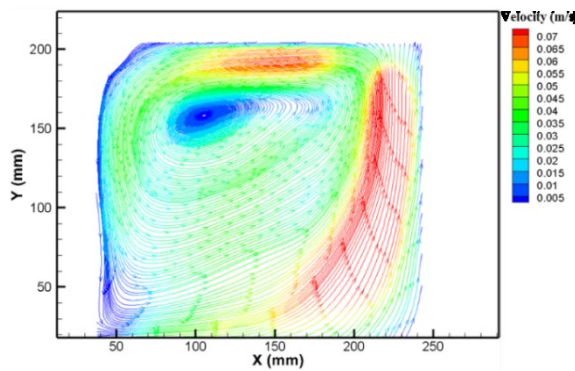
(m) 50 min after heater off, plane 1



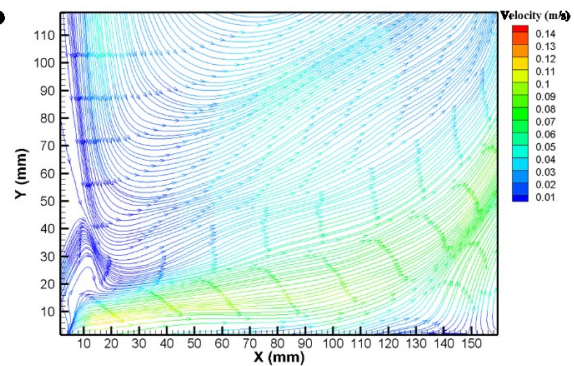
(n) 50 min after heater off, plane 2

Figure 4-13 Indoor flow streamlines with foam base

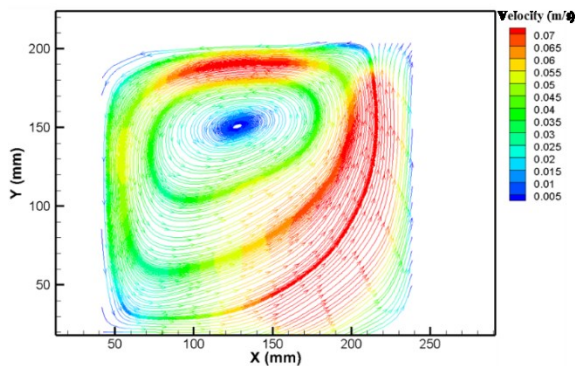
As shown in Fig. 4-13 (a), (c), (e), and (g), after some time, for example, 30 minutes, the interior flow pattern approached a steady state. A vortex was formed at the left corner of the building model, and a relatively high velocity flow went through the inlet at the bottom and up along the side wall. One part of the flow went left and formed a turbulent eddy, while another part of the flow went out of the building. From Fig. 4-13 (b), (d), (f), and (h), it can be seen that the inlet flow velocity increased with time. Fig. 4-13 (i) through (n) shows that the flow pattern changed after the heater was off. The results indicate that after a short time, for example, 15 minutes, the air flow became unstable, and more than one vortex was created at the center of the building model. However, because of the heat storing capacity of the insulation layer, a certain inflow rate was maintained to provide a natural ventilation effect.



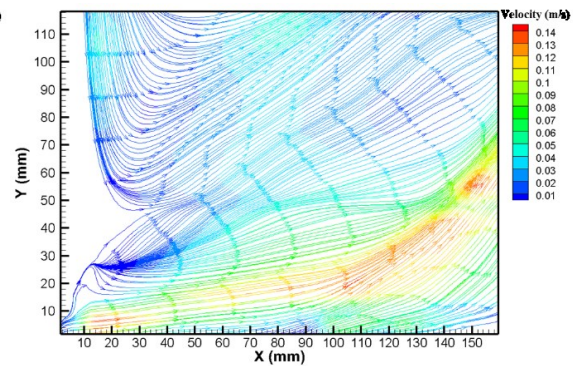
(a) 15 min after heater on, plane 1



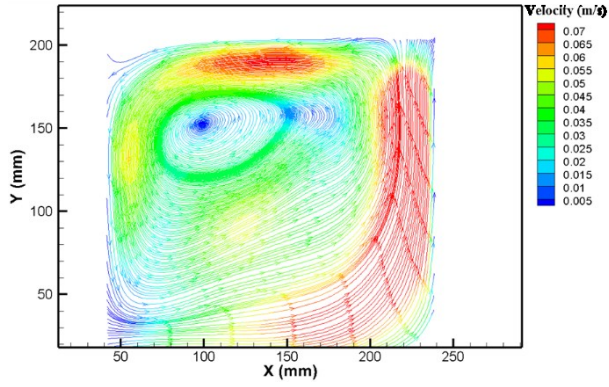
(b) 15 min after heater on, plane 2



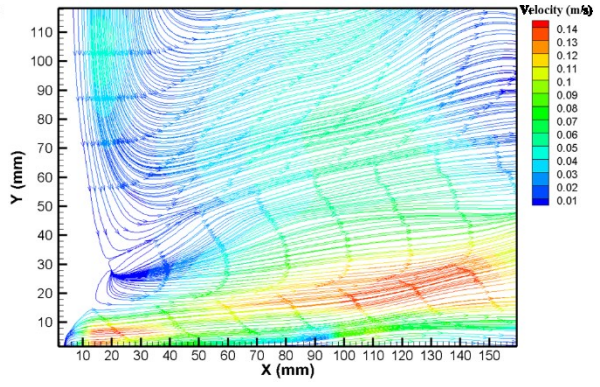
(c) 30 min after heater on, plane 1



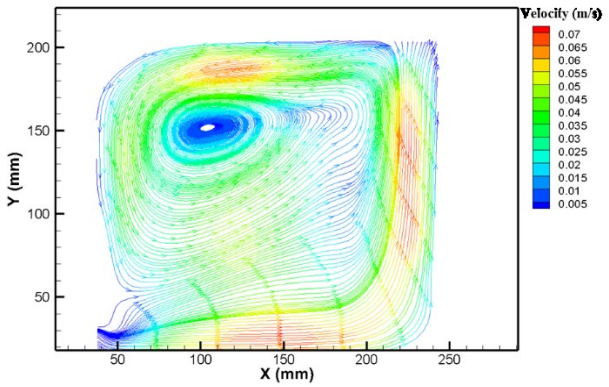
(d) 30 min after heater on, plane 2



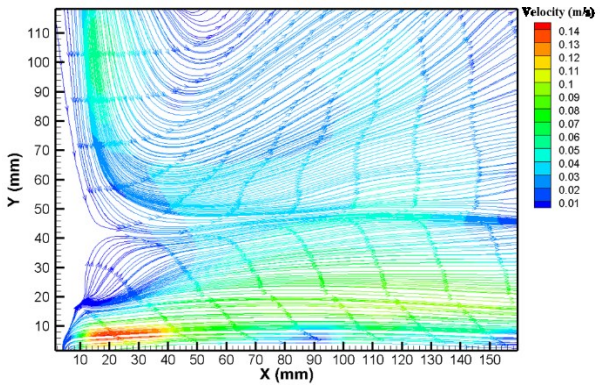
(e) 60 min after heater on, plane 1



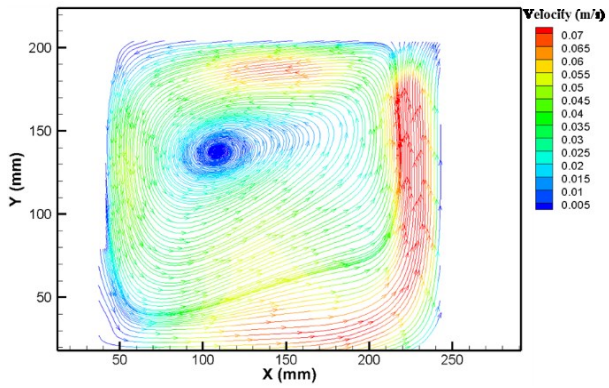
(f) 60 min after heater on, plane 2



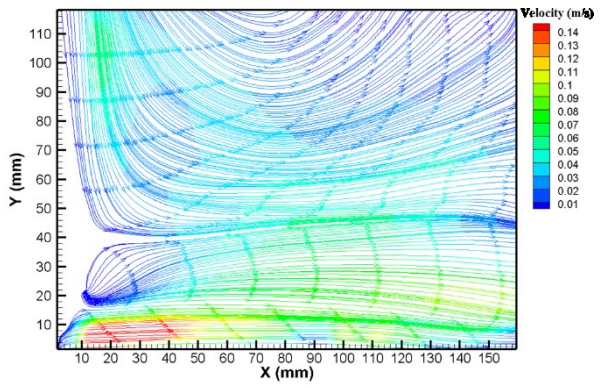
(g) 90 min after heater on, plane 1



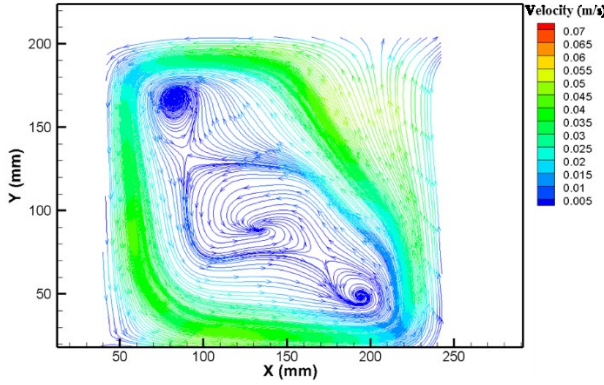
(h) 90 min after heater on, plane 2



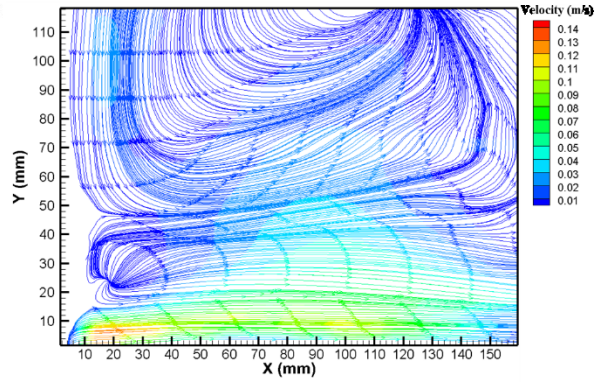
(i) 1 min after heater off, plane 1



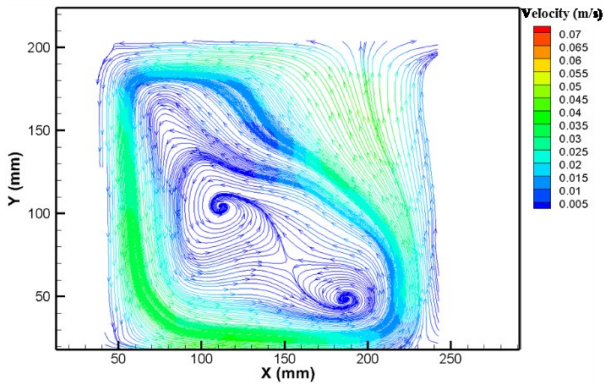
(j) 1 min after heater off, plane



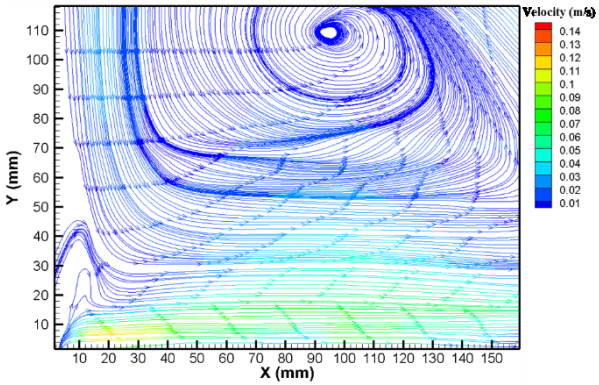
(k) 25 min after heater off, plane 1



(l) 25 min after heater off, plane 2



(m) 50 min after heater off, plane 1



(n) 50 min after heater off, plane 2

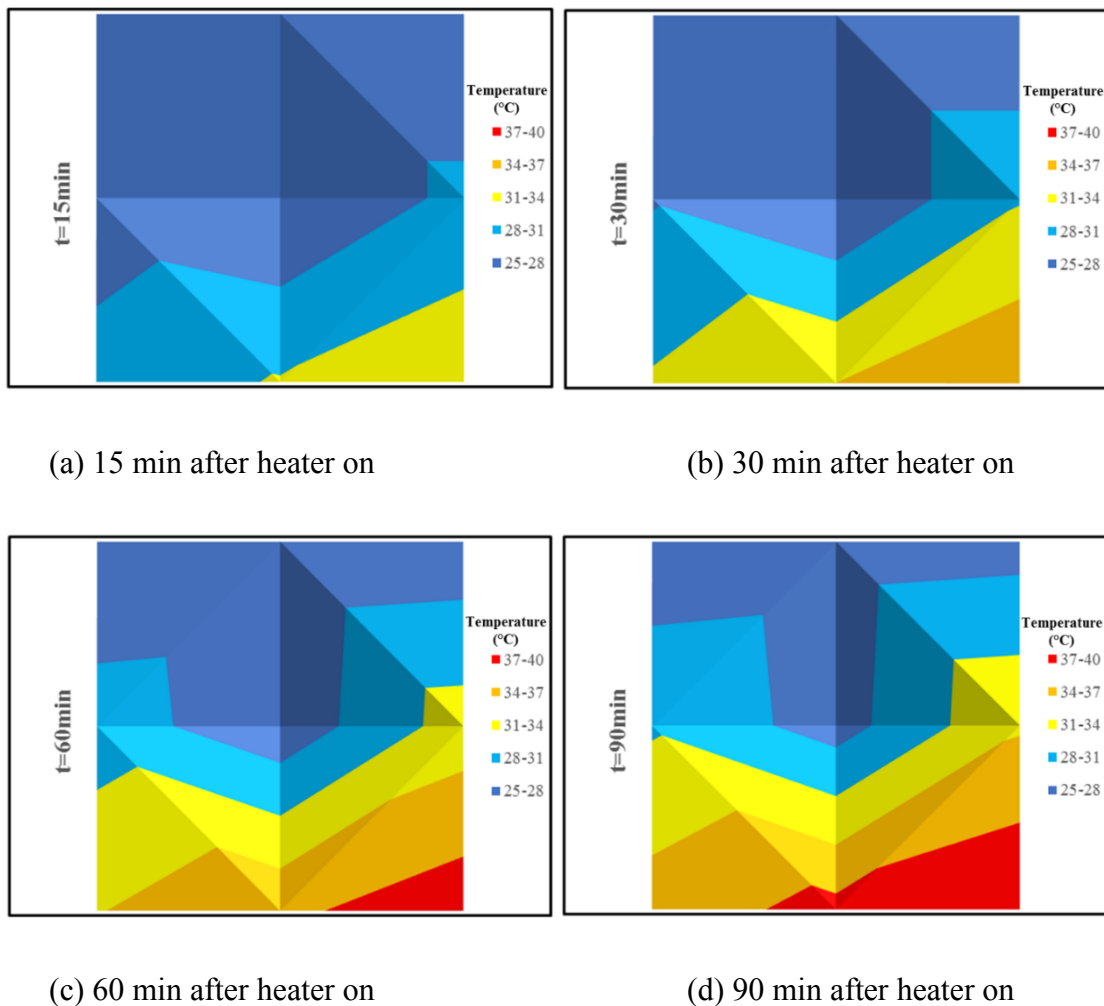
Figure 4-14 Indoor flow streamlines with wood base

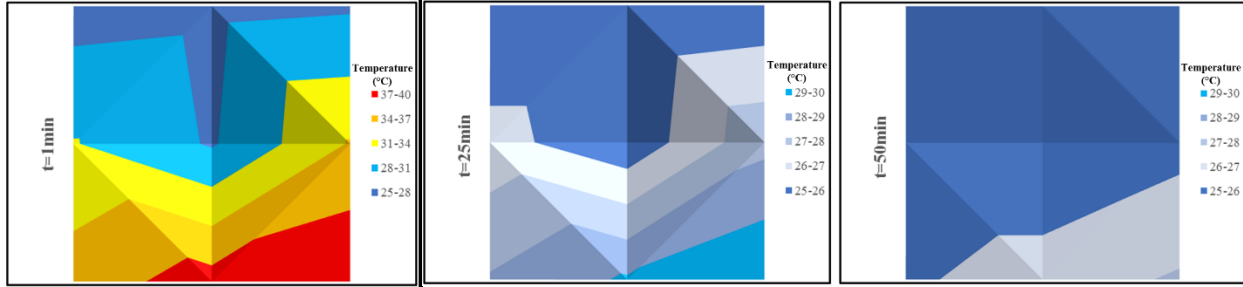
Compared to the indoor natural ventilation with the foam base, the flow field pattern with wood base did not change much as shown in Fig. 4-14 (a) through (n). However, a higher indoor flow velocity can be observed from the results in both heater on and off conditions.

Temperatures inside the single-zone model were measured by thermocouples during the heating process and the heater-off condition. Fig. 4-15 and Fig. 4-16 show the temperature changes with a foam base and a wood base. It can be seen from Fig. 4-15 (a) through (g) that the temperature rose with the heater on, especially at the floor where the heat source was located. After the heater was

turned off, the temperature decreased after a short time, and because of the insulation materials, the temperature near the floor was higher than the indoor air close to the ceiling.

Fig. 4-16 indicates a similar temperature changing process, but with a relatively higher temperature distribution especially at the lower part of the building with the wood insulation base, which agrees with the flow field results measured by PIV that the wood material had a better heat storing capacity than the foam material.



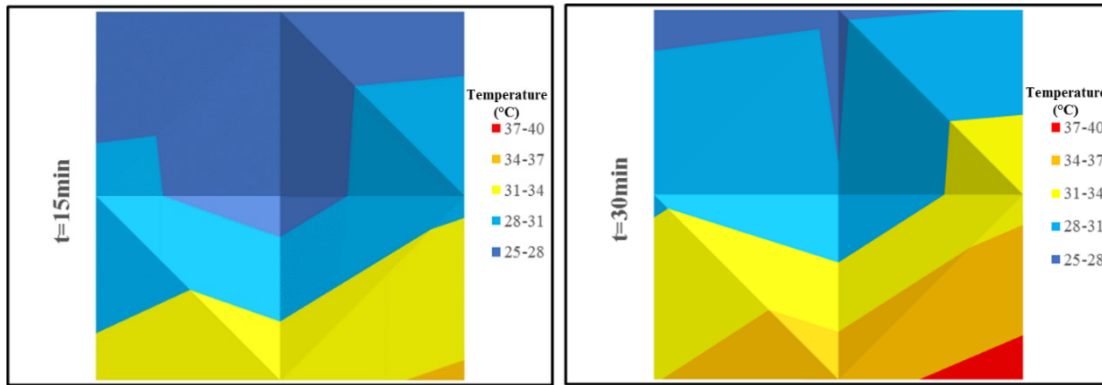


(e) 1 min after heater off

(f) 25 min after heater off

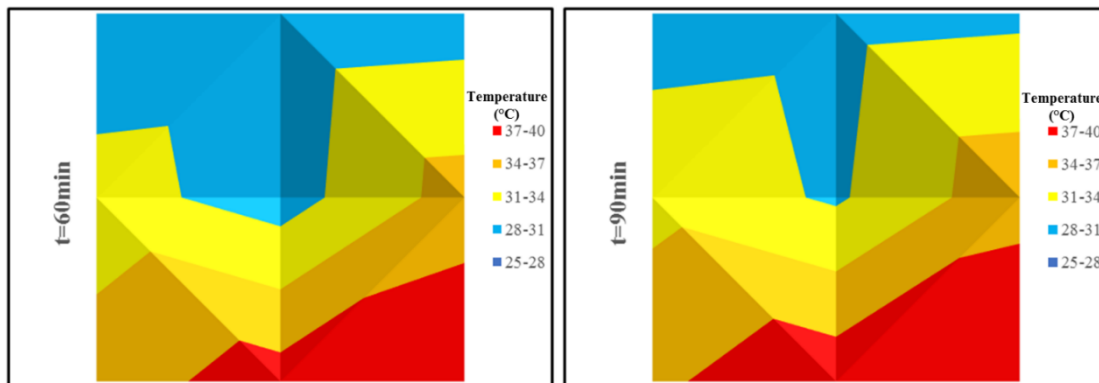
(g) 50 min after heat off

Figure 4-15 Temperature (°C) distribution with foam base



(a) 15 min after heater on

(b) 30 min after heater on



(c) 60 min after heater on

(d) 90 min after heater on



(e) 1 min after heater off

(f) 25 min after heater off

(g) 50 min after heat off

Figure 4-16 Temperature ($^{\circ}\text{C}$) distribution with wood base

4.4 Conclusions

The indoor flow field velocity and temperature with natural ventilation in a single-zone building model was measured by a PIV system and thermocouples 15, 30, 60, and 90 minutes after turning on a heater. Also, for simulating the condition that there is an electricity interruption and all indoor heat sources are turned off, flow field and temperature distributions after the heater was turned off at 1, 25, and 50 minutes were captured. Two insulation materials, wood and foam, were used in the experiments. The PIV flow rate was validated by a tracer gas decay result. The comparison results showed that the difference between the two experimental methods was less than 12%, which is acceptable.

To investigate the natural ventilation effect on the air movement inside the room, the indoor flow pattern with all openings closed was also measured using the PIV technique. The results showed that natural ventilation enhanced the air movement at the human height on the bottom of the building model.

Comparing the flow velocity and temperature variation with different floor insulation materials, it can be seen that in the model with a wood base, the air velocity and temperature was higher than in the model with a foam base. The conclusion can be made that the wood material has better heat storing capacity than the foam material used in our studies.

With PIV measurements, it is possible to capture the whole air flow field of the sub-scale building model. To obtain more accurate and reliable data, it is better to choose a smaller measurement plane to fit the field of view of a typical 2D PIV system.

5 AIR CURTAIN INTERACTION WITH WIND

5.1 Introduction

Modern offices and other commercial buildings are subject to air infiltration, which contributes to high levels of heat loss [88]. On average, the heating load of these buildings due to infiltration is about 25%, while the cooling load caused by infiltration is about 4% [89]. Air curtains can be applied to building entrances to prevent outdoor air infiltration and reduce building energy heat loss [90]. Also, as a virtual barrier separating the indoor and outdoor environments, air curtains can considerably reduce mass, heat, moisture, and particle exchange to provide better indoor comfort [91].

The aim of this research is to characterize the dynamic behavior of the air curtain. A sub-scaled model was designed and built as a 1:10 ratio of the full-scale building model. The whole velocity field around the air curtain at the entrance of the building model was tested by two dimensional PIV. A PIV system can be used to capture the whole velocity field and obtain detailed data on jet flow behavior. A numerical approach was performed using CFD Fluent with an RNG $k - \varepsilon$ model. The PIV measurement results were compared to the validated CFD simulation.

The effect of the jet supply angle, jet supply velocity, wind velocity, wind angle, vestibular, double swing door, and the existence of people on the air curtain characteristics related to the air flow patterns and performance curve are discussed according to the results obtained by experimental and numerical methods. The validated CFD model could provide data for a quantitative analysis of wind effect on air curtain performance.

5.2 Methodology

Particle image velocimetry tests of air curtain performances on a sub-scale model were conducted in the Boundary Layer Wind Tunnel at the Building Aerodynamics Laboratory at Concordia University for open terrain conditions. The blow-down tunnel is of the open-circuit design and is 12.2 m in length with a working section of 1.80 m × 1.60 m (W × H). The sub-scale building model is located at the test section, and is a turntable of 1.60 m diameter for testing under different wind directions, as shown in Fig. 5-1 (a). The longitudinal free wind speed (gradient velocity) at the test section varies between 3 m/s and 14 m/s. The boundary layer wind flow was simulated using triangular boards, a steel plate, and carpet roughness. The wind speed in the wind tunnel was adjusted manually using the wind tunnel flow outlet control.

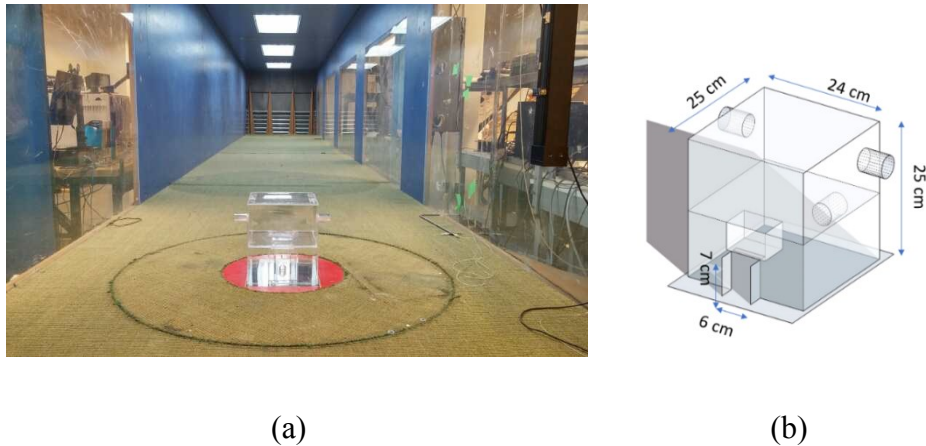


Figure 5-1. (a) Atmospheric boundary layer wind tunnel at Concordia University; (b) scaled-down chamber model.

5.2.1 Model Configuration

A 1:30 scale acrylic model with full-scale plan dimensions of 7.5 m × 7.2 m × 7.5 m (L × W × H), which corresponded to a 2-story building, was used for the study. The sub-scale model was studied previously by Yulli in regard to leakages through building entrances and vestibules. As shown in

Fig. 5-1 (b), the model, which had dimensions of 25 cm × 24 cm × 25 cm (L × W × H), was divided into an upper section and a lower section. An air curtain was simplified as a block with a slot and was installed in the lower section of the model. A fully-open (opening angle of 90°) double-swing door of 6 cm × 7 cm (W × H) and a sliding door with same opening size were chosen for the tests. Two holes of 4 cm in diameter were drilled at the upper sides of the model for injecting the compressed air to create the air curtain jet. The flow rate of the compressed air supply was controlled by a digital flow controller (NZXT Technologies) to achieve the desired jet velocity. Another hole of 4 cm in diameter at the back of the model was connected to a series of external CPU fans with digital controllers to regulate the exhaust airflow rate from the model.

5.2.2 PIV measurement setup

A series of PIV tests were conducted in the wind tunnel to visualize the flow pattern in the middle cross-section. The tests provided a better understanding of the aerodynamic interaction between the approaching wind and the air curtain jet flows. Fig. 5 (a) shows the PIV experimental setup in the wind tunnel. The laser was placed outside the wind tunnel and the camera was inside of it. To create a vertical laser sheet, a mirror was installed at a 45° angle under the wind tunnel to reflect the incident laser sheet vertically along the center of the air curtain door. To capture the air curtain jet flow movement, aluminum oxide powder was used as tracer seeds. During the experiment, the compressed air was projected into the mixed box, where air was mixed with aluminum oxide powder as shown in Fig. 5-2 (b). At the same time, the tracer particles were sent into the building model with the air. To capture the outdoor air movement, tracer particle oil droplets were released about 1m in front of the model during the experiments. Other PIV parameters are shown in Table 6 below. The pressure difference across the model door and the infiltration rate were also measured in the wind tunnel test. Detailed measurement methods were explained in the previous studies [92].

Table 6. Setup of PIV data acquisition and evaluation.

Field of view	Interval of time	Sampling frequency	Number of captured pictures	Interrogation window	Overlap	Measured time
120 mm×89 mm	40 μ s	8 Hz	50 frames	32 pixels × 32 pixels	25%	7 s

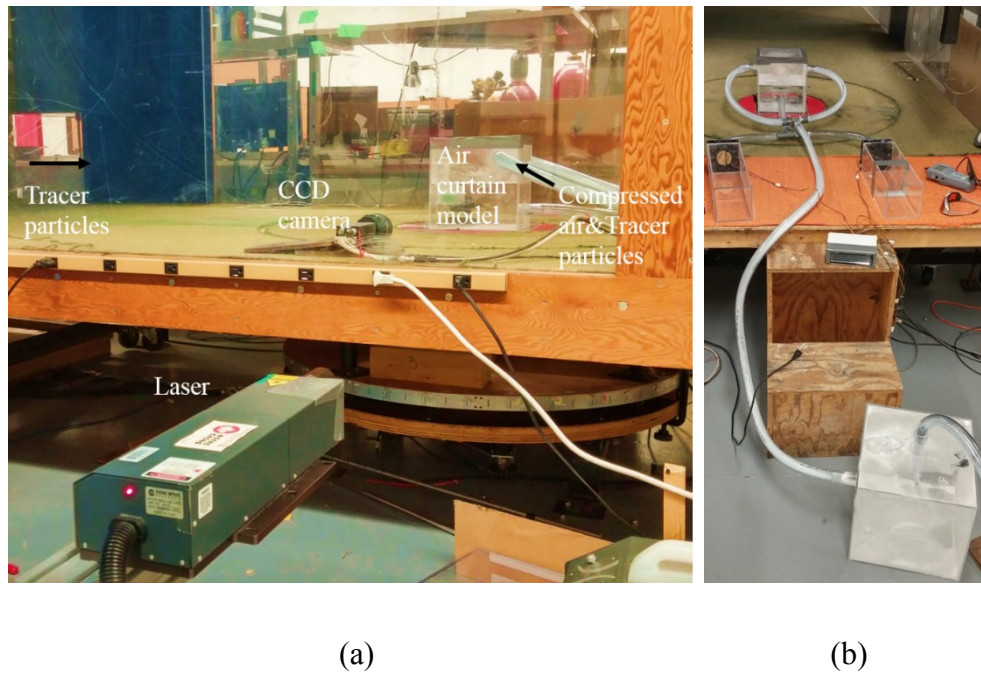


Figure 5-2. PIV measurements setup.

5.2.3 CFD simulation for wind tunnel experiment

The numerical model was constructed principally using structured hexahedra grids, since it has been proven that this mesh style provides the best computational results [93]. Due to the circular section of the fan, a structured O grid was used near it. The expansion ratio between two consecutive cells was limited to 1:1.2. The number of total mesh cells was 6,528,477. The mesh structure built for the numerical simulation is shown in Fig. 5-3.

The computational domain is a parallelepiped, as shown in Fig. 5-4. Based on recommendations from past studies [94][95], the dimensions of this domain are specified as follows: considering H (0.24 m) as the building height in the model, the top boundary is $6 H$ (1.44 m) higher than the model. The lateral boundary is $5 H$ (1.2 m) away from the building and the outlet boundary is $20 H$ (4.8 m) downwind from the building to allow flow development. The distance between the inlet plane and the model is $5 H$ (1.2 m).

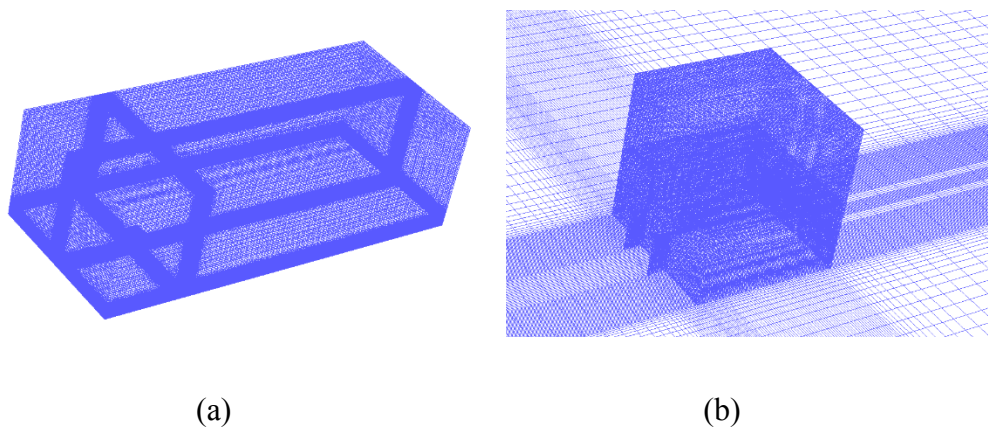


Figure 5-3. Mesh structure for CFD simulations. (a) Whole domain; (b) model.

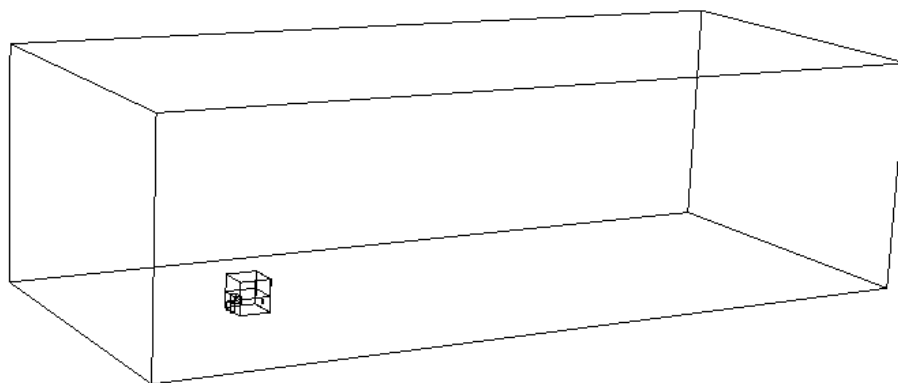


Figure 5-4. Schematic view of the model with outer domain.

Two power law equations were created according to the wind profile data measured in the wind tunnel experiments. The power law exponent of 0.1, which corresponds to the open country terrain, was used for the study. The velocity at the building door height (0.5 m) was 4 m/s and 10 m/s for different cases. The wind velocity and turbulence intensity measured in the wind tunnel and used in the CFD simulation is shown in Fig. 5-5. The bottom surface is specified as a rigid plane with an aerodynamic roughness length $Z_0=0.00095$ m. In Fluent, this roughness length is implemented by the sand-grain roughness height k_s (m), which can be defined using the function developed by Blocken et al. [95]:

$$k_s=9.793Z_0/C_s, \quad \text{Eq. 5-1}$$

C_s is a roughness constant. Considering that the roughness height cannot be larger than half of the mesh cell size, k_s is set as 0.001. Therefore, the roughness constant is specified as 0.93.

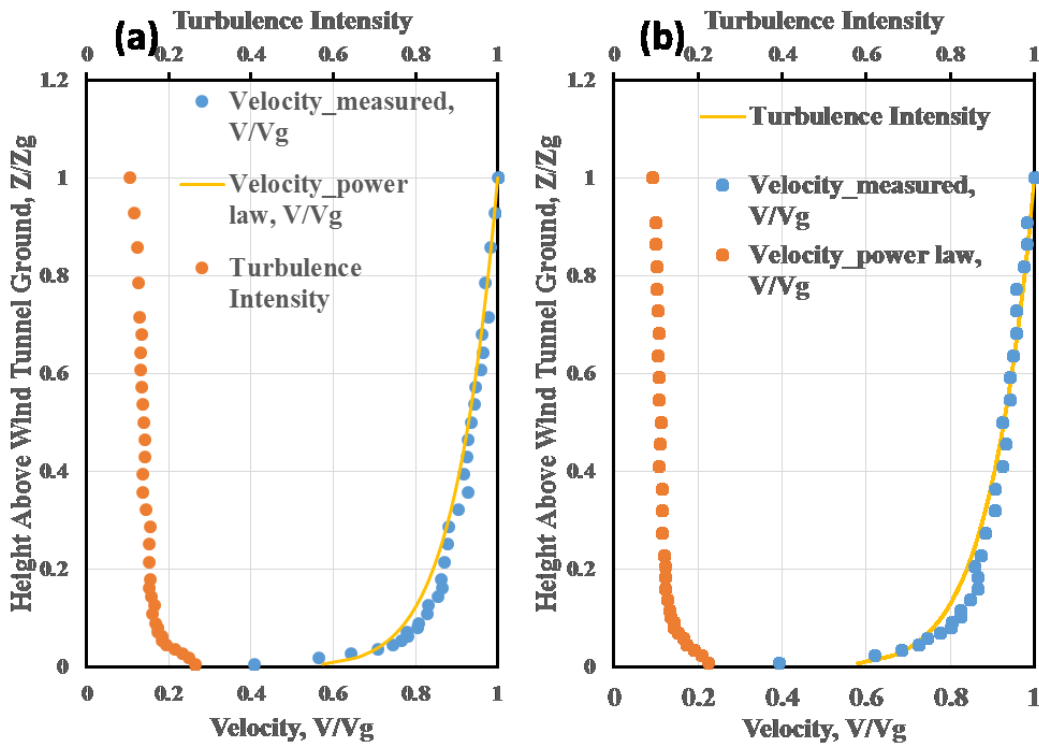


Figure 5-5. Velocity and turbulence intensity profiles of the wind tunnel flow: (a) 4 m/s reference velocity; (b) 10 m/s reference velocity.

5.2.4 Air curtain flow analytical model

According to previous papers [20][97][98], a turbulent slot jet impinging on a flat plate can normally be described as shown in Fig. 5-6. The flow field of an impinging jet can be divided into three zones: (1) the free jet prior to impingement, (2) the impingement region, and (3) the wall jet region. The free jet region consists of one or more of the following zones depending on the distance between the jet nozzle and the ground surface: (1) the potential core, where the centerline velocity remains constant and equal to the velocity of the jet at nozzle exit while the jet is mixing and diffusing with the ambient air in its shear layers; (2) the transition zone, in which the jet shows a decay of the centerline velocity and the shear layers interact at the jet centerline; and (3) the fully developed zone, where the jet is totally developed and attains a self-similar behavior.

E. Nino et al. [20] visualized the air curtain jet with the fan driven at a frequency of 10 Hz ($Re = 10,000$) by an integration in time of the jet evolution as shown in the Fig. 5-7, which shows the characteristic zones indicated as A) the potential core, B) transition zone, and C) the fully developed zone.

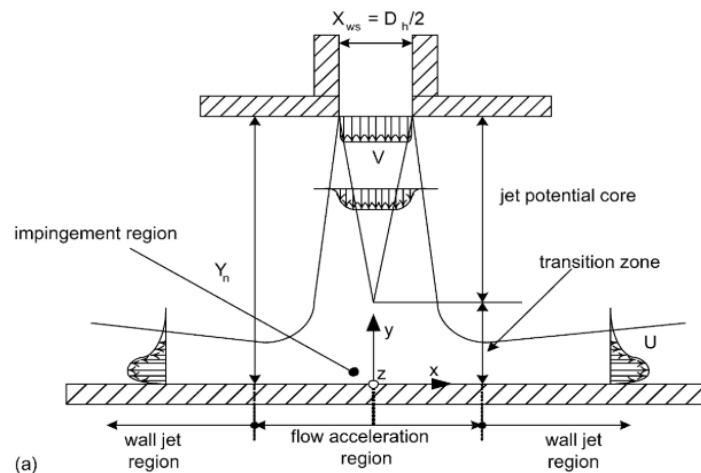


Figure 5-6. Schematic of slot jet impingement on a flat surface.

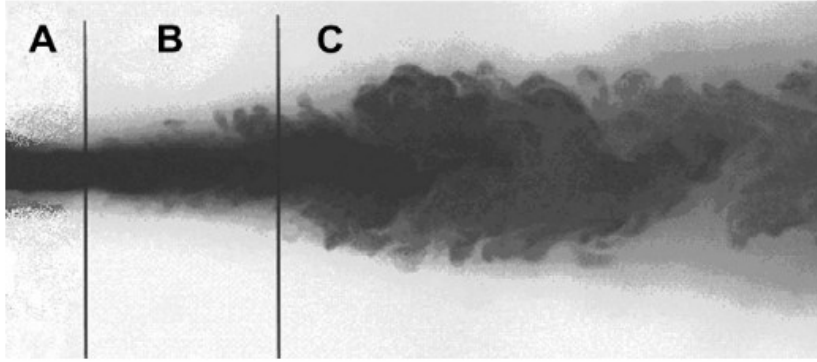


Figure 5-7. Visualization of air curtain at 10 Hz. A) potential core zone; B) transition zone; C) developed zone.

F.C. Hayes [98][99] studied how the discharge angle, the slot width, and the outlet velocity affect the performance of an air curtain and developed a theoretical model for predicting the rate of heat transfer across the air curtain. As mentioned in his studies, the velocity distribution along an isothermal jet can be described with the following equations:

the transition zone, $\bar{x} < 5.2b_0$

$$\frac{u}{u_0} = \frac{1}{2} \left[1 + \operatorname{erf} \left(\sigma_1 \frac{\bar{y} + \frac{b_0}{2}}{\bar{x}} \right) \right], \quad \text{Eq. 5-2}$$

and the fully developed zone, $\bar{x} > 5.2b_0$

$$\frac{u}{u_0} = \frac{\sqrt{3}}{2} \sqrt{\frac{b_0 \sigma_2}{\bar{x}}} \left[1 - \tan h_t^2 \left(\sigma_2 \frac{\bar{y}}{\bar{x}} \right) \right]. \quad \text{Eq. 5-3}$$

Where u is jet centerline velocity, u_0 is the jet initial velocity, \bar{y} is the distance to the jet centerline which direction normal to the jet centerline, \bar{x} is the distance to the nozzle which direction tangent to the jet centerline, b_0 is the nozzle width, h_t is the heat transfer coefficient, and σ_1 and σ_2 both are empirical constants, the value can be calculated as: $\sigma_1 = 13.5$, and $\sigma_2 = 7.67$.

5.3 Results and discussions

5.3.1 Comparing PIV, CFD, and analytical results

Fig. 5-8 shows the comparison of jet flow centerline velocities between the PIV experiment, the CFD model, and the theoretical model. It can be seen that the simulation result is relatively close to the results of the PIV experiment for the range of $3b_0$ to $9b_0$. The maximum difference for this part is about 14%. Compared to the theoretical results, jet flow velocities obtained from the experimental and CFD results enter the fully developed region faster. When the jet flow is near the ground, the velocity decays with a higher gradient because of the impingement with the ground and wind. Except for in the region that is closest to the ground (the distance to the jet inlet is larger than $9b_0$), the differences between the theoretical result and experimental results are less than 15%.

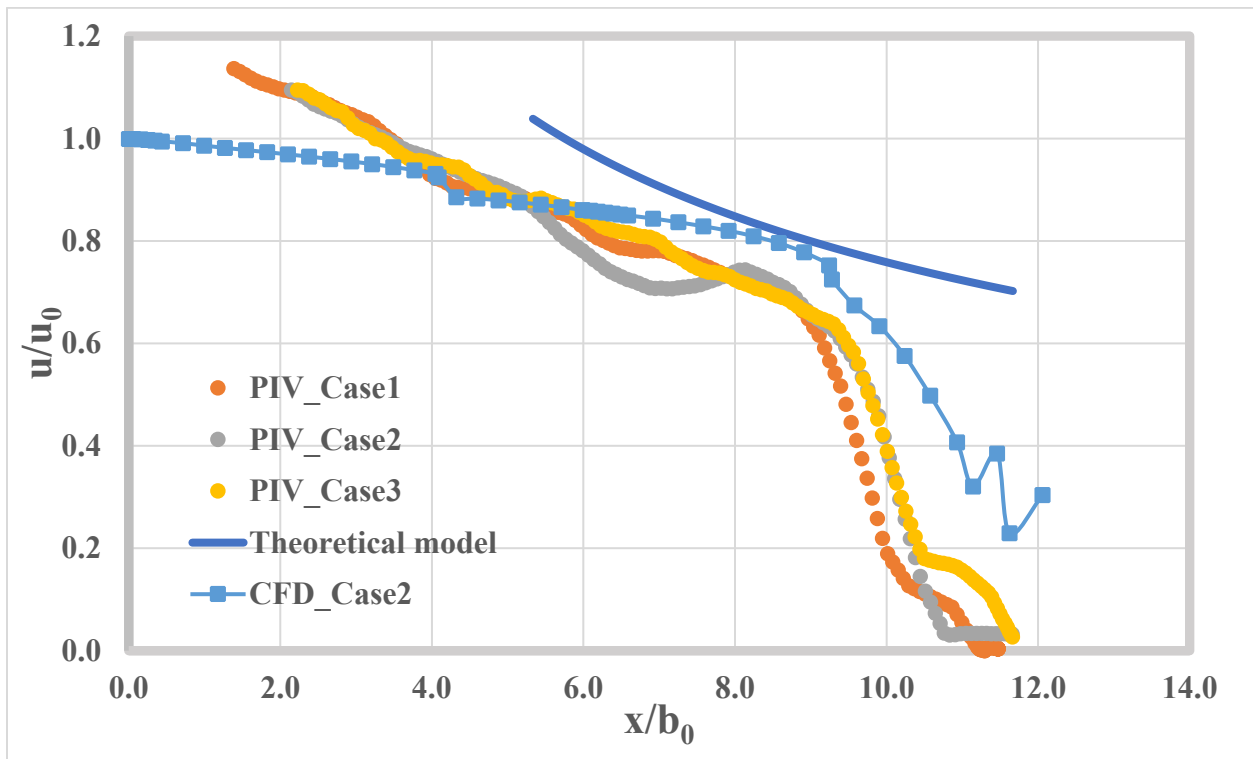


Figure 5-8. Centerline velocity below the air supply inlet (Case1: air curtain supply speed 9.6 m/s and supply angle 0° , ΔP -2.67 Pa; Case2: air curtain supply speed 9.6 m/s and supply angle 0° , ΔP 1.74 Pa; Case3: air curtain supply speed 9.6 m/s and supply angle 0° , ΔP 6.17 Pa).

5.3.2 Wind tunnel wind field

The wind field about 0.8 m in front of the building model in the wind tunnel was measured using the PIV technique. This provides a brief view of the gradient wind distribution in the wind tunnel and impingement with the façade of the building model. The wind field velocity contour and streamlines are shown in Fig. 5-9 and Fig. 5-10. It was seen that the wind distribution in the wind tunnel was almost uniform in the x direction, until about 0.4 m in front of the model. Under the influence of the collision effect with the building façade, the wind velocity was weakened. As shown in Fig.5-10, the flow separates when it meets the building model, and the stagnation point is located at a height of about 0.16 m. A vortex is formed at the base of the building.

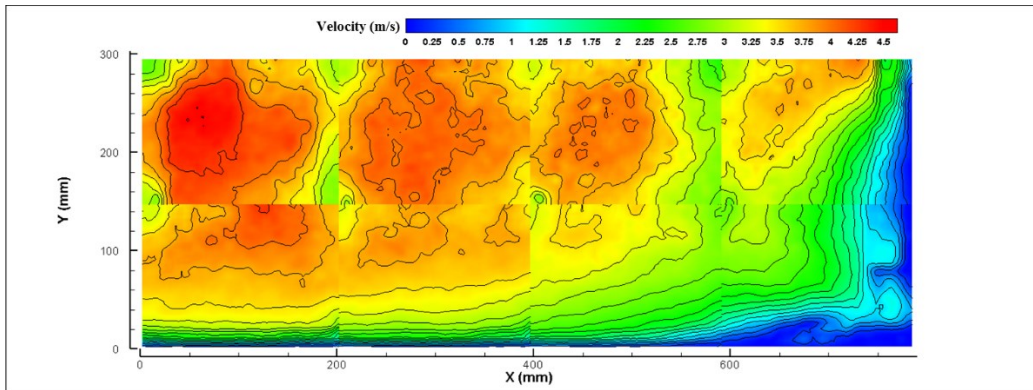


Figure 5-9 Wind field contour of wind tunnel

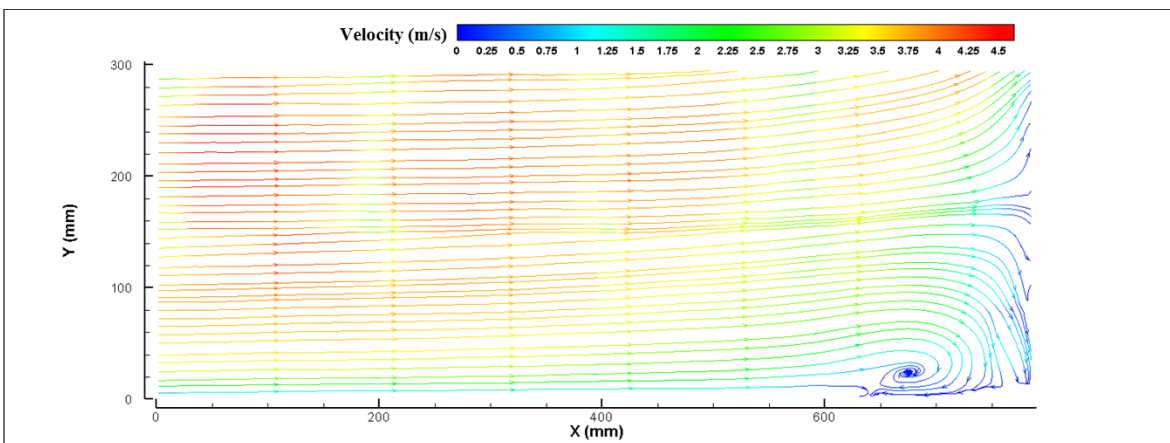


Figure 5-10 Wind field streamlines of wind tunnel

5.3.3 Jet flow visualization

The flow field generated by the air curtain was investigated by means of the PIV technique under different supply velocity conditions. The images reported in Fig. 5-11 (a), (b), and (c) represent the instantaneous images of the air curtain jet flows at different air supply velocities (9.6 m/s, 5.6 m/s, and 2 m/s). The estimated Reynolds number is 4161 for 9.6 m/s supply, 2427 for 5.6 m/s air curtain supply, and 867 for 2 m/s air curtain supply. A longer potential core zone could be visualized at the jet flow with a higher Reynolds number. For the jet flow with the low Reynolds number, it is substantially laminar with some instability present a distance away from the nozzle exit. If the Reynolds number is increased, the instability is present closer to the jet slot. In general, in increasing the Re , it is possible to observe and increase the jet's vortex. The distance from the nozzle exit to where the instability starts to grow is reduced with a higher Reynolds number.

The structure of the air curtain jets were illuminated with alumina powder as tracing seeds. Fig. 5-11 (a) and (b) shows that the tracer particles are capable of following the slot jet flow issuing from the compressed air supply device with a relative high Reynolds number. As shown in Fig. 5-11 (c), only air was illuminated with fewer tracer particles, which could affect the flow velocity field results at the region close to the jet slot. Also, it shows that two kinds of tracer seeds can be illuminated and visualized at the same time at a relatively high resolution.

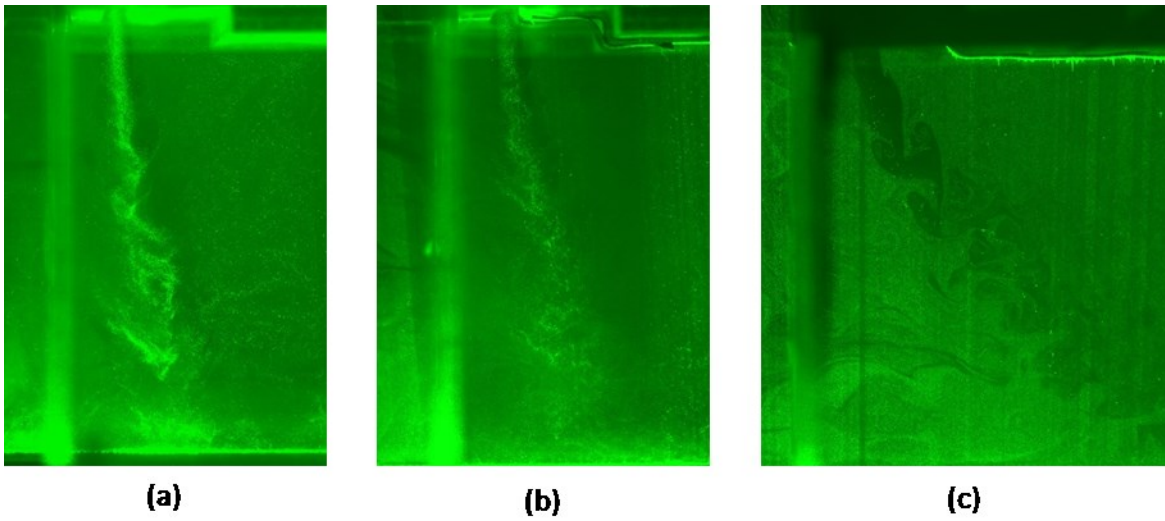


Figure 5-11. Flow visualization of air curtain jet flow under $0.00285 \text{ m}^3/\text{s}$ infiltration at the door: (a) 9.6 m/s supply velocity; (b) 5.7 m/s supply velocity; (c) 2 m/s supply velocity.

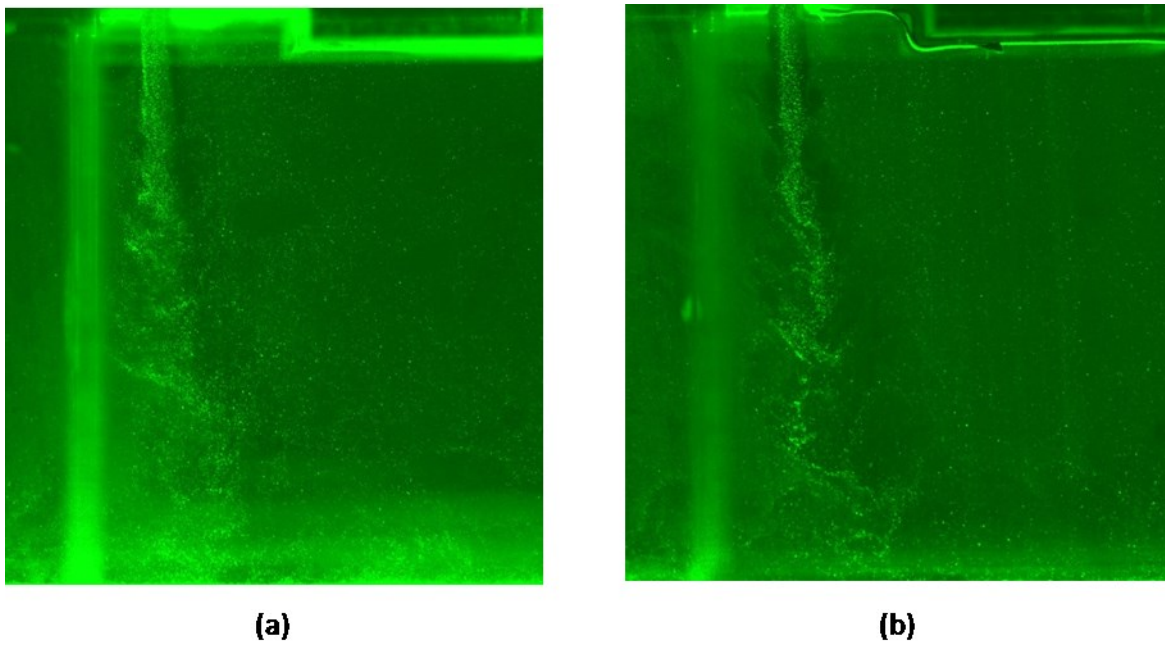


Figure 5-12. Flow visualization of air curtain jet flow under $0.00056 \text{ m}^3/\text{s}$ exfiltration: (a) 9.6 m/s supply velocity; (b) 5.7 m/s supply velocity.

5.3.4 Effects of air supply and validation with CFD simulation results

Fig. 5-13 and Fig. 5-14 present the experimental and numerical results of the air curtain with supply angles of 0° and 20° and a wind speed of 4 m/s. Fig. 5-15 and Fig. 5-16 present the experimental and numerical results of the air curtain with supply angles of 0° and 20° and a wind speed of 10 m/s. Fig. 5-13a, Fig. 5-14a, Fig. 5-15a, and Fig. 5-16a show decent agreement between the experimental results and the CFD results in terms of the air curtain performance curve. Note that larger discrepancies appear when the air curtain supply angle is 20° . Fig. 5-13b, Fig. 5-14b, Fig. 5-15b, and Fig. 5-16b show even better agreement between PIV and the CFD velocity vector field. The air infiltration decreases significantly from $0.00285 \text{ m}^3/\text{s}$ to $-0.00067 \text{ m}^3/\text{s}$ when the air supply angle increases from 0° to 20° . Observing the flow pattern in Fig. 5-13b and Fig. 5-14b, it was seen that the jet with a 20° supply angle is more capable of resisting the outside wind, as the air curtain bends towards the outside of the building so that exfiltration can occur. For the air curtain with a 0° supply angle, infiltration would occur at the lower parts of the jet flow as the outside wind mixes with the jet air flow and bends into the indoor environment. A similar conclusion can be reached with Fig. 5-15b and Fig. 5-16b.

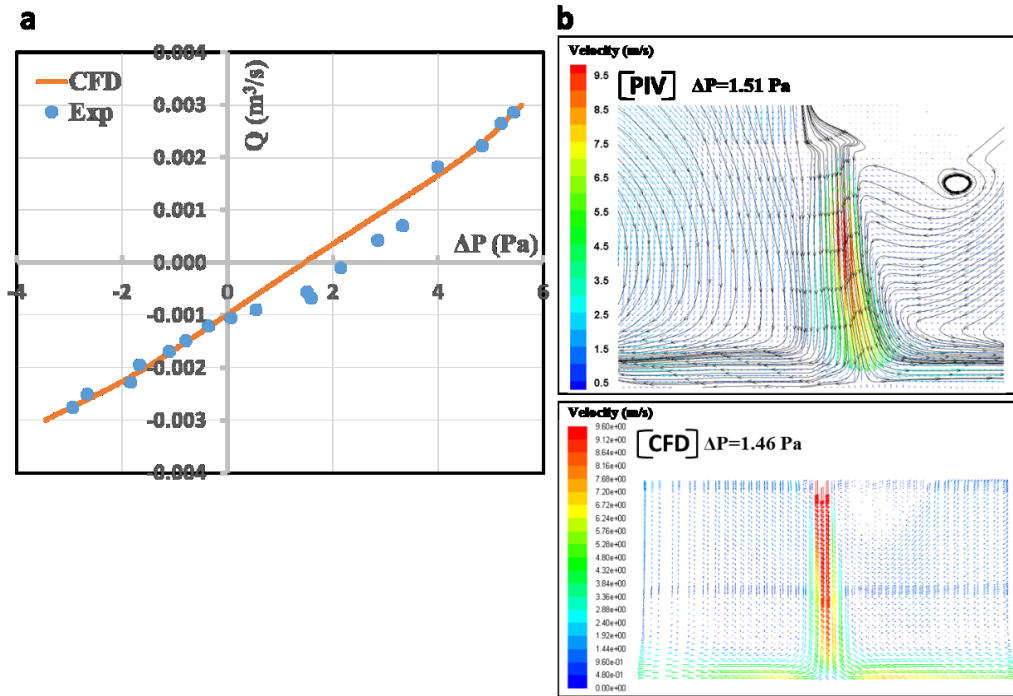


Figure 5-13. Performance curve and velocity vectors of 0° air curtains with an average supply speed of 9.6 m/s under 4 m/s wind obtained by experimental and numerical methods.

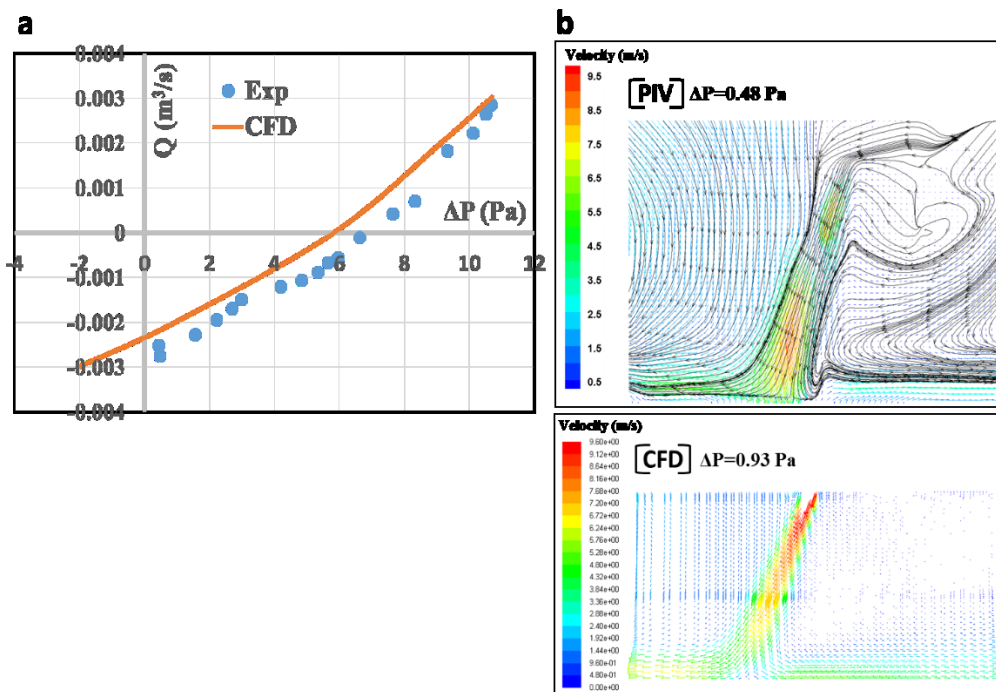


Figure 5-14. Performance curve and velocity vectors of 20° air curtains with an average supply speed of 9.6 m/s under 4 m/s wind obtained by experimental and numerical methods.

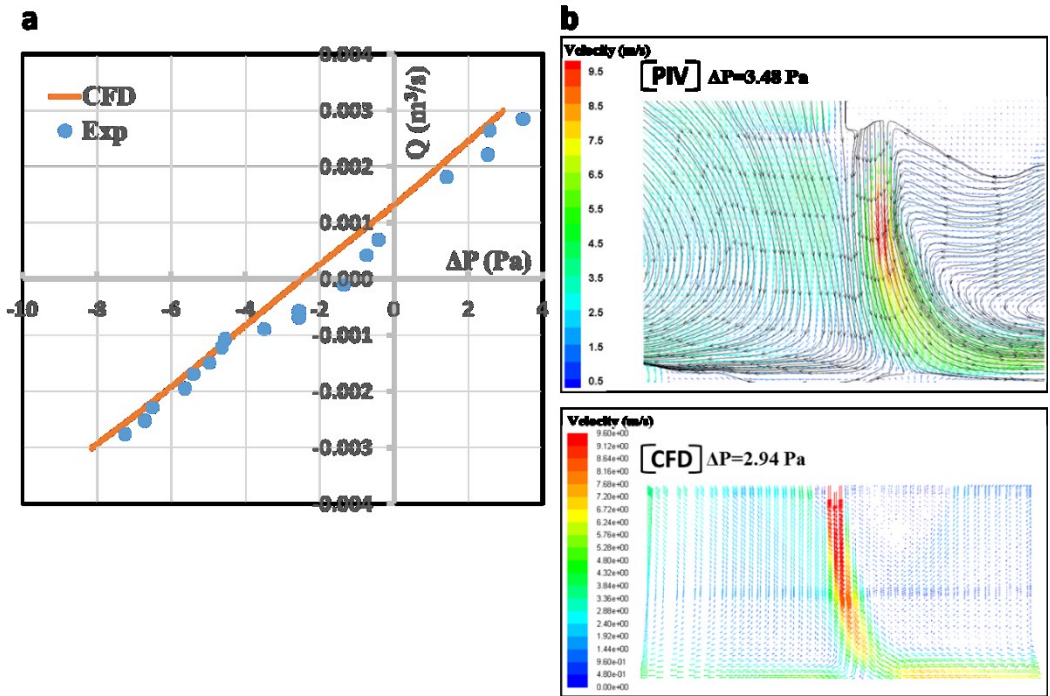


Figure 5-15. Performance curve and velocity vectors of 0° air curtains with an average supply speed of 9.6 m/s under 10 m/s wind obtained by experimental and numerical methods.

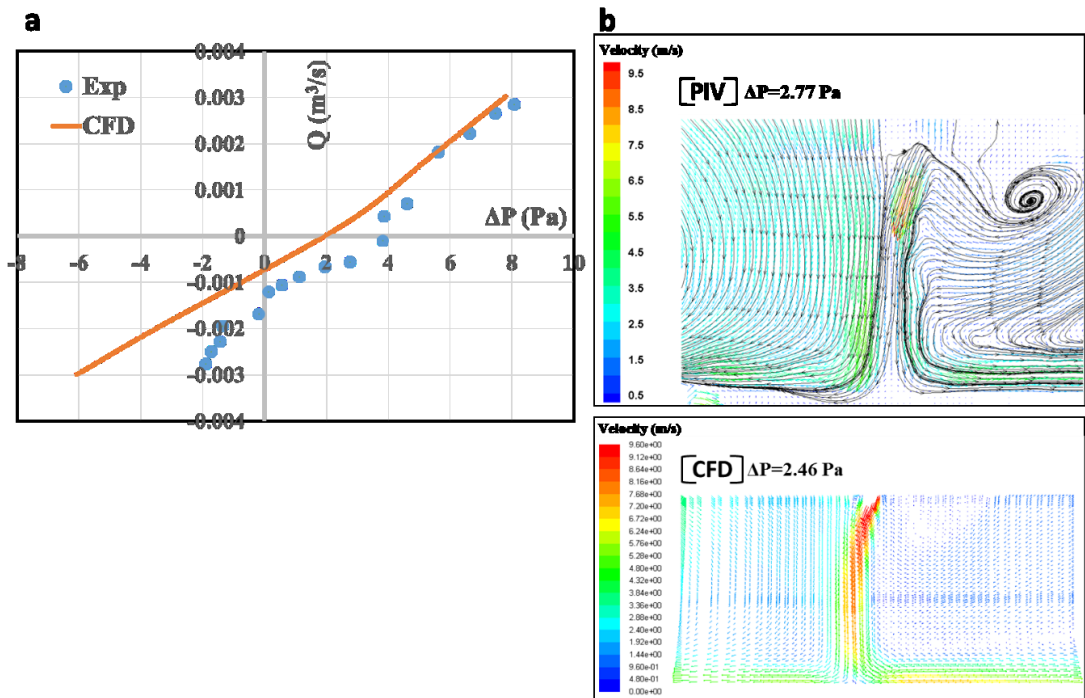


Figure 5-16. Performance curve and velocity vectors of 20° air curtains with an average supply speed of 9.6 m/s under 10 m/s wind obtained by experimental and numerical methods.

Fig. 5-17 and Fig. 5-18 show the performance curve and velocity vectors field of air curtains with 0° air supply angles, under conditions of no outside wind, for different air supply velocities obtained by experimental and numerical methods. Fig. 5-17a and Fig. 5-18a show acceptable agreement between the experimental results and the CFD results in terms of the air curtain performance curve. Also, acceptable agreement between the PIV and CFD results can be seen for the comparison of air curtain flow fields. It was seen that with similar pressure differences across the door of the building, the air curtain jet with a lower supply velocity more easily bent into the interior and created more infiltration, increasing from -0.00067 to 0.00089 m^3/s .

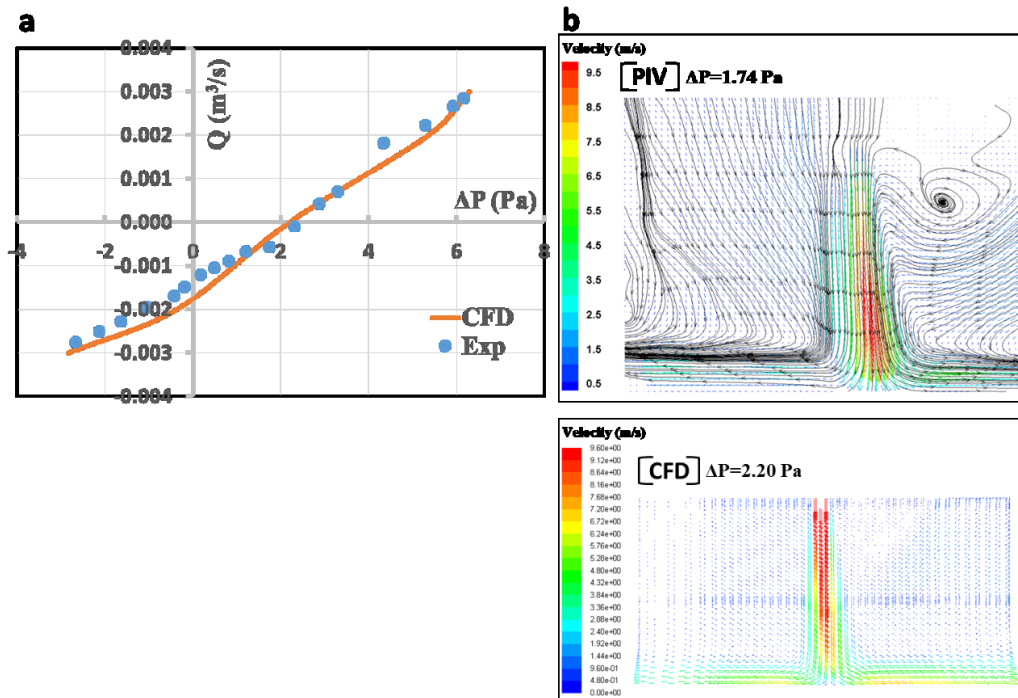


Figure 5-17. Performance curve and velocity vectors of 0° air curtains with an average supply speed of 9.6 m/s under no wind conditions obtained by experimental and numerical methods.

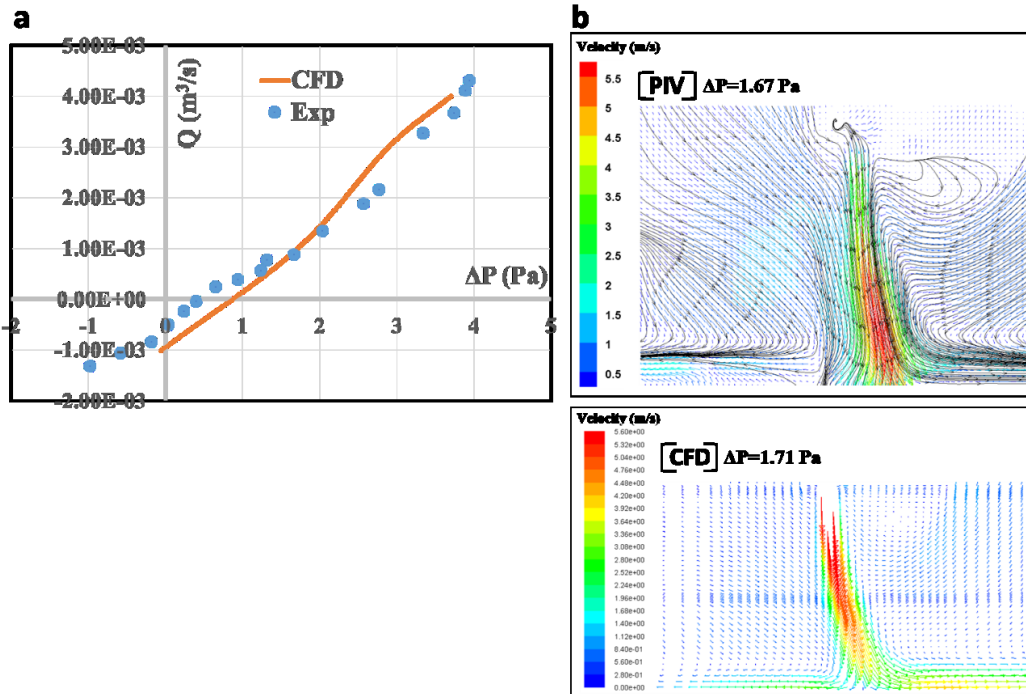


Figure 5-18. Performance curve and velocity vectors of 0° air curtains with an average supply speed of 5.6 m/s under no wind conditions obtained by experimental and numerical methods.

5.3.5 Effects of wind and validation with CFD simulation results

Fig. 5-19 shows the velocity vector fields of air curtains with 9.6 m/s air supply velocities and 0° air supply angles for different wind velocities obtained by the experimental and numerical models. The results indicate that the air curtain jet bends more towards the right with increasing wind velocity due to the impingement with the strong inflow. The phenomenon is obvious when comparing the results under no wind conditions and 10 m/s wind.

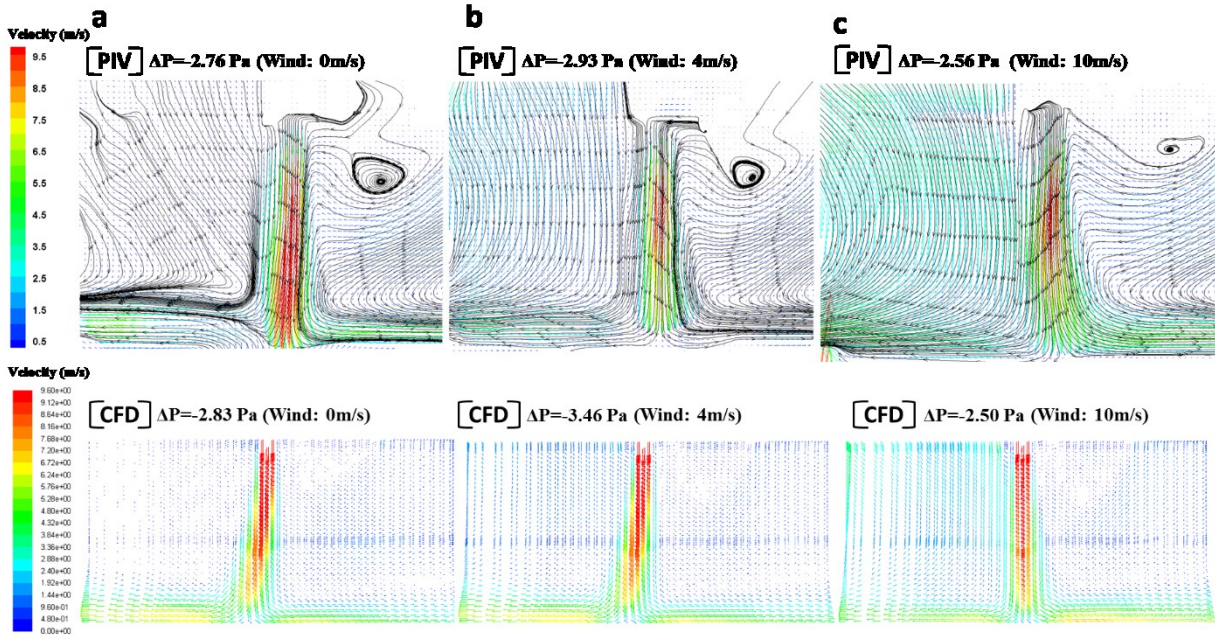
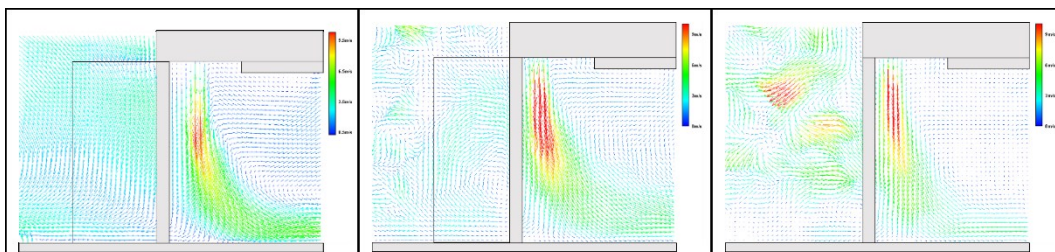
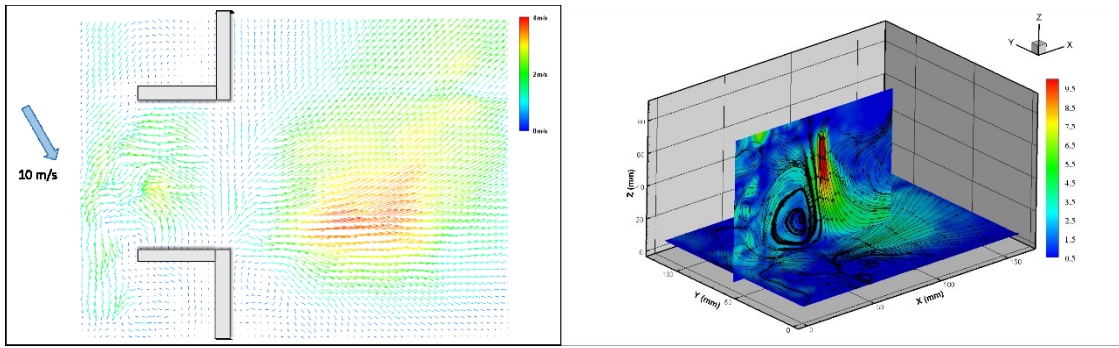


Figure 5-19. Velocity vectors of air curtains with 9.6 m/s supply velocities and 0° supply angles, under the same pressure conditions ($\Delta P=2.5$ Pa) obtained by the experimental and numerical methods.

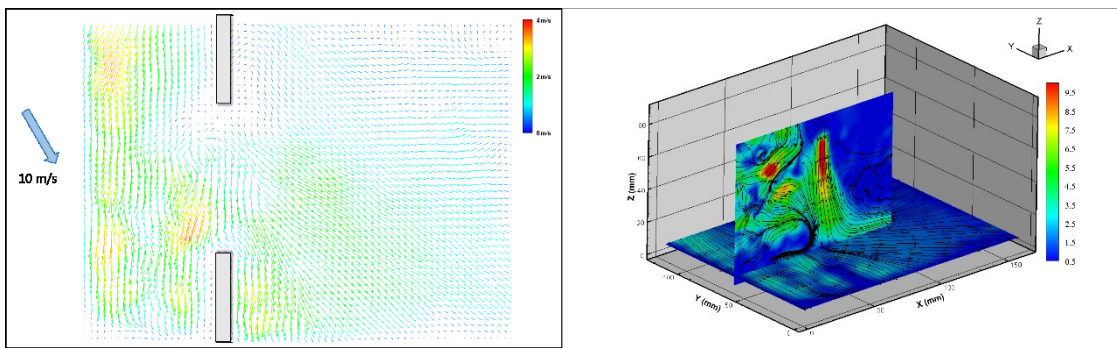
Fig. 5-20 presents the experimental results obtained with 0° and 60° outside wind blowing towards the building model under the same jet supply conditions. As shown in Fig. 5-17 (b), (d), and (e), the double doors protected the air curtain when the wind was at an angle of 60° so that less collision between the air curtain and the wind occurred, which resulted in better performance of the air curtain jet.



(a) 0° wind angle ($\Delta P = 3$). (b) 60° wind angle, with double swing door. (c) 60° wind angle, with sliding door.



(d) 60° wind angle, horizontal view, with double swing door. (e) 60° wind angle, 3D view.



(f) 60° wind angle, horizontal view, with sliding door. (g) 60° wind angle, 3D view.

Figure 5-20. Velocity vectors of air curtains with 9.6 m/s air supply velocities and 0° air supply angles under 10 m/s wind obtained by experimental methods.

5.3.6 Effects of the vestibular and people in different positions

Fig. 5-21 shows the streamlines of air curtain jet flow interactions with outside wind with a vestibular. It was seen that one part of the wind was blocked by the vestibular and formed a vortex outside the vestibular, while another part of the wind was driven towards the interior due to the pressure difference across the door of the building model. In general, the vestibular promoted the resistance of the air curtain to the outside wind.

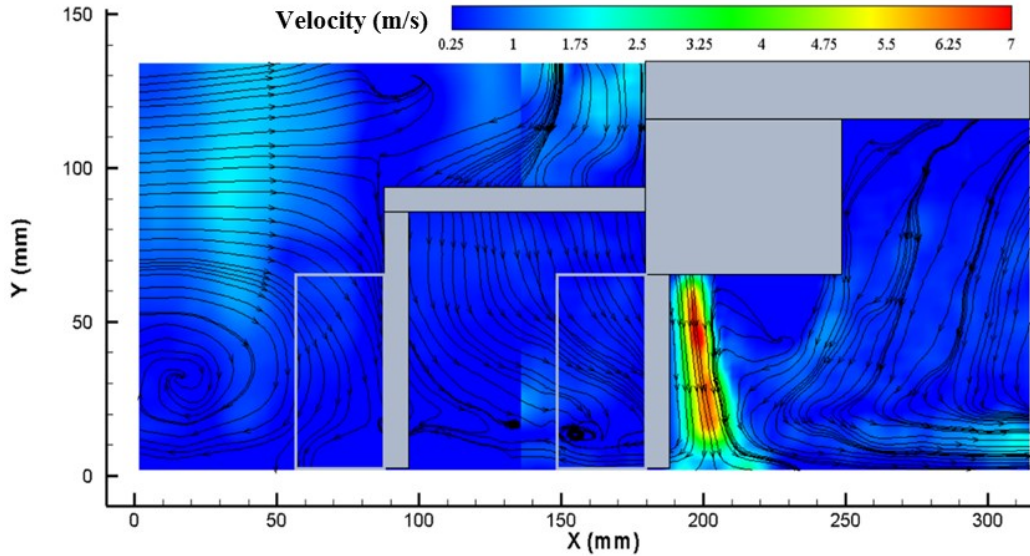


Figure 5-21. Velocity vectors of air curtains with 9.6 m/s air supply velocities and 0° air supply angles, under 4 m/s outside wind obtained by the experimental method.

Fig. 5-22 shows the experimental results with a model of a person standing below the air curtain and in front of the building model. The PIV flow pattern indicates that the slot jet flow moves around the person while still providing a sealing effect as that the jet maintains a relatively high velocity at the feet of the person when the person stands below the nozzle. Under the same outside wind conditions, when the person stands in front of the building model, the person provides additional resistance to the wind, and it can be seen that the flow velocity decreases.

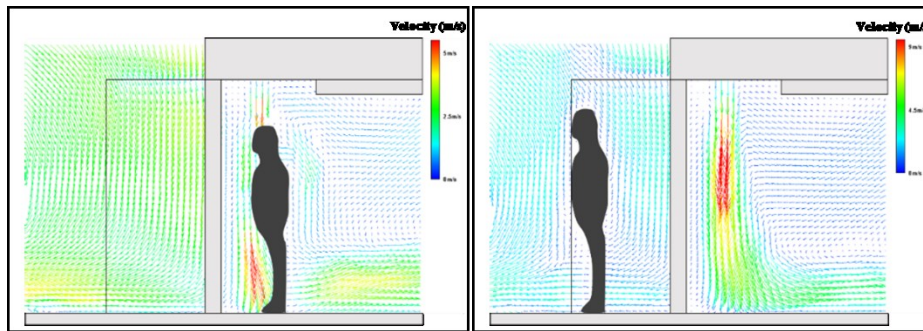
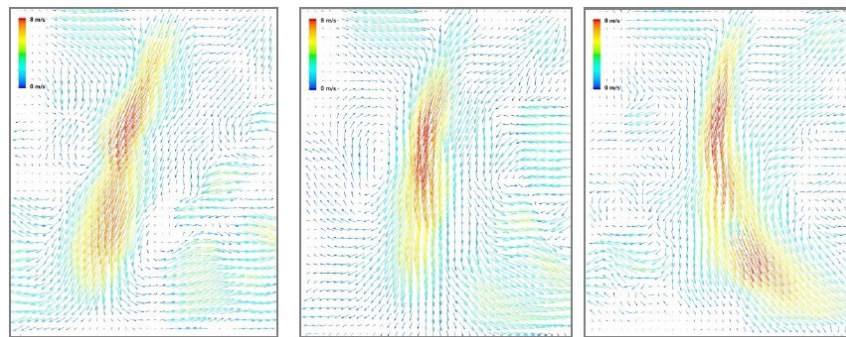


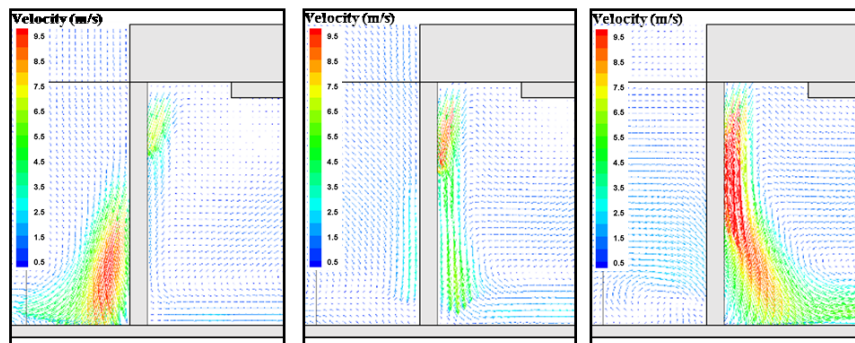
Figure 5-22. Velocity vectors of air curtains with 9.6 m/s air supply velocities and 0° air supply angles under 10 m/s outside wind conditions obtained by experimental methods.

5.3.7 Results comparison in full-scale experiments and sub-scale experiments

Full-scale air curtain PIV experiments were conducted by Sherif Goubran et al. [99]. To confirm that the scaled PIV experiments are comparable to the large-scale tests, some of the results under similar pressure difference conditions obtained by sub-scale model PIVs and full-scale model PIVs were compared. As shown in Fig. 5-23, acceptable agreement can be achieved for the air curtain flow pattern under different pressure difference conditions. Also, with help of the sub-scale model PIV technique, it is possible to obtain results of a higher quality and completeness. This proves that compared to full-scale models, sub-scale models are more suitable for PIV experiments, as the dimensions of sub-scale models are similar to the field of view of typical PIV systems.



(a) Full-scale exp. $\Delta P=1.7$ Pa (b) Full-scale exp. $\Delta P=4.7$ Pa (c) Full-scale exp. $\Delta P=8.5$ Pa



(d) Sub-scale exp. $\Delta P=0.4$ Pa (e) Sub-scale exp. $\Delta P=6.3$ Pa (f) Sub-scale exp. $\Delta P=11.1$ Pa

Figure 5-23. Comparison of velocity vectors of air curtains with 9.6 m/s air supply velocities and 20° air supply angles between full-scale and sub-scale experimental methods.

5.4 Conclusions

In this study, a total of 36 PIV experiments were conducted to investigate the effects of the air curtain supply angle and speed, outside wind angle and speed, and the present of a vestibular and people on the performance of air curtains according to the flow velocity vector fields, infiltration/exfiltration rates through the doors, and pressure differences across the doors. In summary, increasing the air supply angle and speed will improve air curtain performance, but will create exfiltration under certain conditions. Under relatively high-speed winds, the air curtain sealing effect on the doors is weakened. Compared to the model with sliding doors, the model with double swing doors will help to block the impingement of outside wind, so that the performance of an air curtain is increased. The presence of a vestibular and people in different standing positions will affect the air curtain performance as well. In addition, the CFD model was built and validated by experimental results. The comparison shows acceptable agreement between the numerical results and PIV results in flow patterns and a centerline velocity decay curve.

Further investigation of wind effects on the performance of air curtains was conducted based on the validated CFD model. As shown in Fig. 5-24 and Fig. 5-25, air curtain performance under wind with ranges of 0 m/s to 20 m/s was simulated. More quantitative analysis will be done in the future.

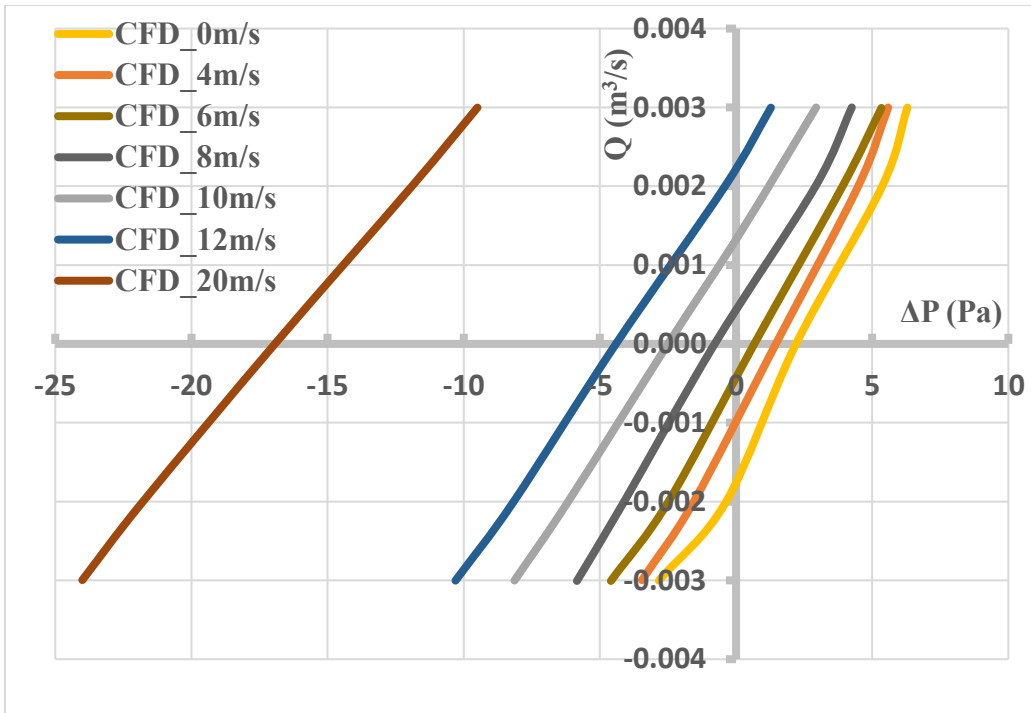


Figure 5-24. Performance curve of air curtains with 9.6 m/s air supply velocities and 0° air supply angles.

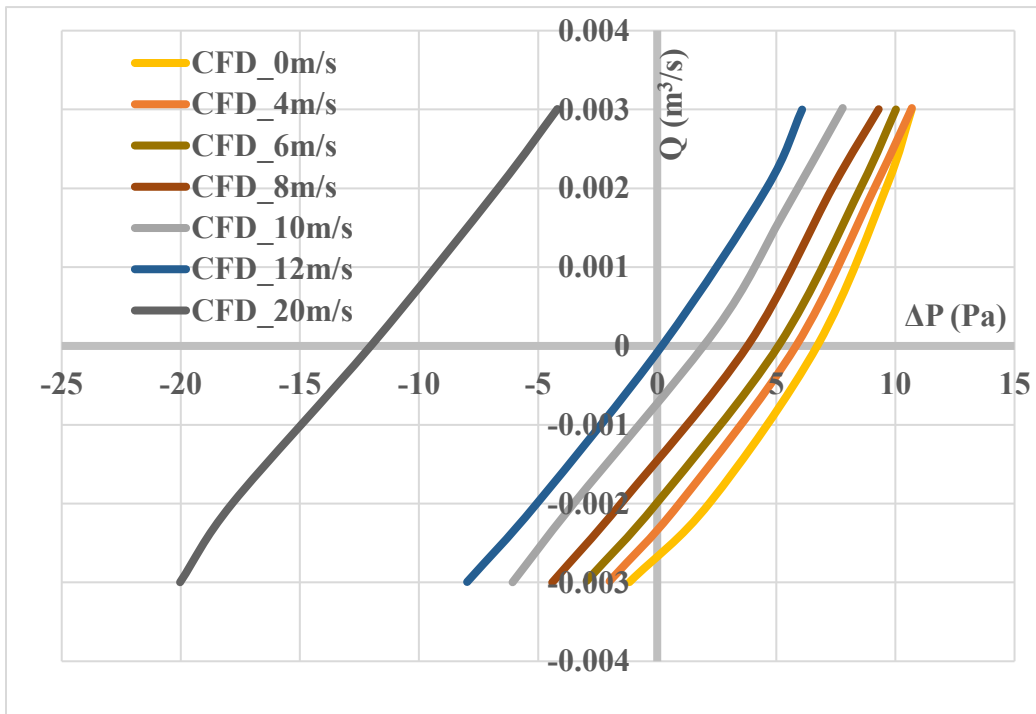


Figure 5-25. Performance curve of air curtains with 9.6 m/s air supply velocities and 20° air supply angles.

6 HYBRID VENTILATION IN SUB-SCALE HIGH-RISE BUILDINGS

6.1 Introduction

Natural ventilation driven by the buoyancy effect and wind pressure can be utilized for effective cooling systems in buildings. But under some climate conditions, natural ventilation is not enough for providing a comfort indoor environment. A hybrid ventilation system, using a natural ventilation strategy combined with a mechanical system, can extend the applicability of natural ventilation to some degree.

Understanding how hybrid ventilation systems affect the indoor environment of a building, particularly ventilation rates and indoor air temperature, is important in evaluating an energy-saving design and predicting a building's indoor environment conditions.

Hybrid ventilation in high-rise building was already studied by previous researches by full-scale measurement and simulation models [100][101]. But because of the limitation of the methods, it is difficult to conduct the ventilation studies to the whole building for every floors.

The objective of this chapter is to investigate the performance of hybrid ventilation systems in regard to airflow pattern and temperature distribution in a sub-scale 16-story building model compared to its natural ventilation performance. Particle image velocimetry results will be used to validate a multizone numerical model.

6.2 Methodology

6.2.1 Experimental design

The 1:100 sub-scale building model was designed to be a model of the Concordia University Engineering building (EV building), which is a 16-story high building located in downtown

Montreal (45.5°N, 74°W). The full-scale building consists of five three-story atria separated by floor slabs, an office area, and corridors that connect the exterior with the indoor environment. Two large façades face approximately southwest and northeast, while the atrium is located on the southwest façade of the building, extending from the 2nd floor to the 16th floor. Each three-story atria is connected by floor grilles, enhancing the buoyancy-driven flow in the whole building, and a motorized damper system is installed at the end of the corridors in the south and north façade of each floor. An exhaust fan system is located at the top atrium of the building to promote the mechanical ventilation effect. Fig. 6-1 shows the SE façade and top view of sub-scaled EV building. The sub-scaled model was designed based on the full-scale building. The dampers at the top three floors and bottom three floors were closed. As the dampers of the corridors and a mechanical ventilation fan is opened when the outdoor temperature is between 15 °C and 22 °C, the outdoor temperature conditions during the PIV experiment were set around 19.5 °C. A CPU fan was installed on the top of the building model as shown in Fig. 6-1 (b) to simulate the mechanical ventilation in the real EV building. The air flow rate as measured by anemometer was about 0.005 m³/s. A heater wire of 100 W was installed in the office area on every floor of the building model to simulate heat resources, for example, devices and humans.

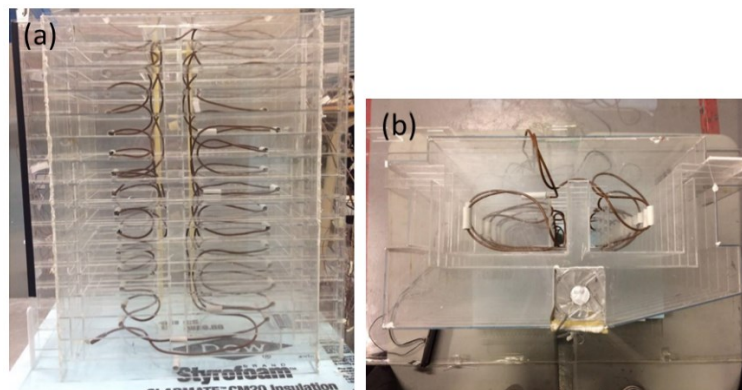


Figure 6-1. EV building model. (a) SE facade of EV building model; (b) top view of the EV building model.

6.2.2 PIV measurement setup

The PIV experiment was conducted using oil particles of diameter 1-2 μm as tracing seeds. To minimize the influence of the initial velocity of the tracer particles, the oil droplets were released into the chamber before the experiments. The experiments were carried out after the seed concentrations were high enough around the building model. It must be mentioned that the density of the seeds cannot be too high or it will block the view of camera or reduce the resolution of the recorded images. For capturing the inflow and outflow fields across the corridor grilles of all 10 floors, 10 measurements were conducted using the PIV system. A traverse system was used in the test as shown in Fig. 6-2, as it would allow the measurements to be conducted under the same conditions without frequent calibration of the PIV system. Other PIV parameters are shown in Table 7 below.

Table 7. Setup of PIV data acquisition and evaluation.

Field of view	Interval time	Sampling frequency	Number of captured pictures	Interrogation window	Overlap	Measured time
149 mm \times 112 mm	100 μs	15 Hz	100 frames	32 pixels \times 32 pixels	25%	7 s

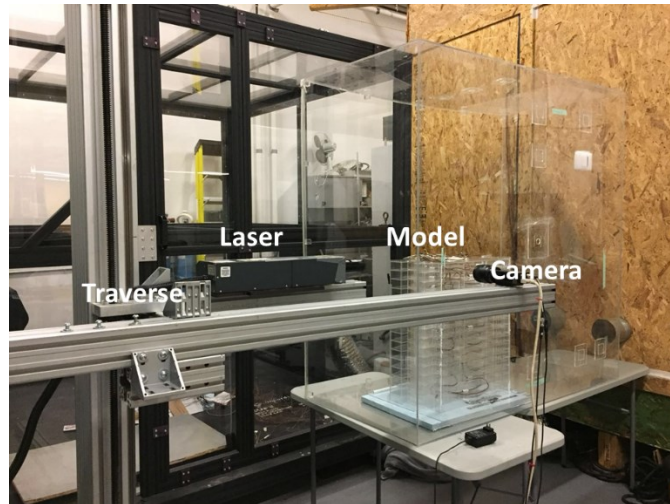


Figure 6-2. Schematic PIV experiments setup.

6.2.3 Numerical simulation model

A multizone numerical model of the sub-scale EV building was built for further hybrid ventilation study. In the multizone network simulation model, temperature and pressure distribution were assumed to be well-mixed as a homogeneous state in each control volume.

The mass balance equation used in the model is:

$$\sum_{z=1}^{N_{zones}} \dot{m}_{zi} + S_i = \frac{dM_i}{dt}. \quad \text{Eq. 6-1}$$

The energy balance equation used in the model are:

$$M_i C_p \frac{dT_i}{dt} = \sum_{z=1}^{N_{zones}} \dot{m}_{zi} C_p (T_z - T_i) + \sum_{w=1}^{N_{surfaces}} h_w A_w (T_s - T_i) + Q_i, \quad \text{Eq. 6-2}$$

$$M_w C_{pw} \frac{dT_w}{dt} = U_w A_w (T_i - T_o), \quad \text{Eq. 6-3}$$

$$U_w = \frac{1}{\frac{1}{h_i} + \frac{L_w}{k_w} + \frac{1}{h_o}}. \quad \text{Eq. 6-4}$$

The interior node connection equation used in the model is:

$$\dot{m}_{zi} = C(\Delta P_{zi})^n. \quad \text{Eq. 6-5}$$

And orifice equation used in the model is:

$$\dot{m} = C_d A_{open} \sqrt{2\rho\Delta P}. \quad \text{Eq. 6-7}$$

6.3 Results and discussion

6.3.1 Airflow field measurement results

Fig. 6-3 shows the air flow velocity contour across the corridor grilles at the SE façade for the 4th to 13th floors under natural ventilation conditions and indicates the influence of buoyancy-driven forces on the flow field within the corridors of the building. It was seen that the strong stack effect creates higher inflows at the lower floors than the upper floors and higher outflows at the lower floors than the upper floors.

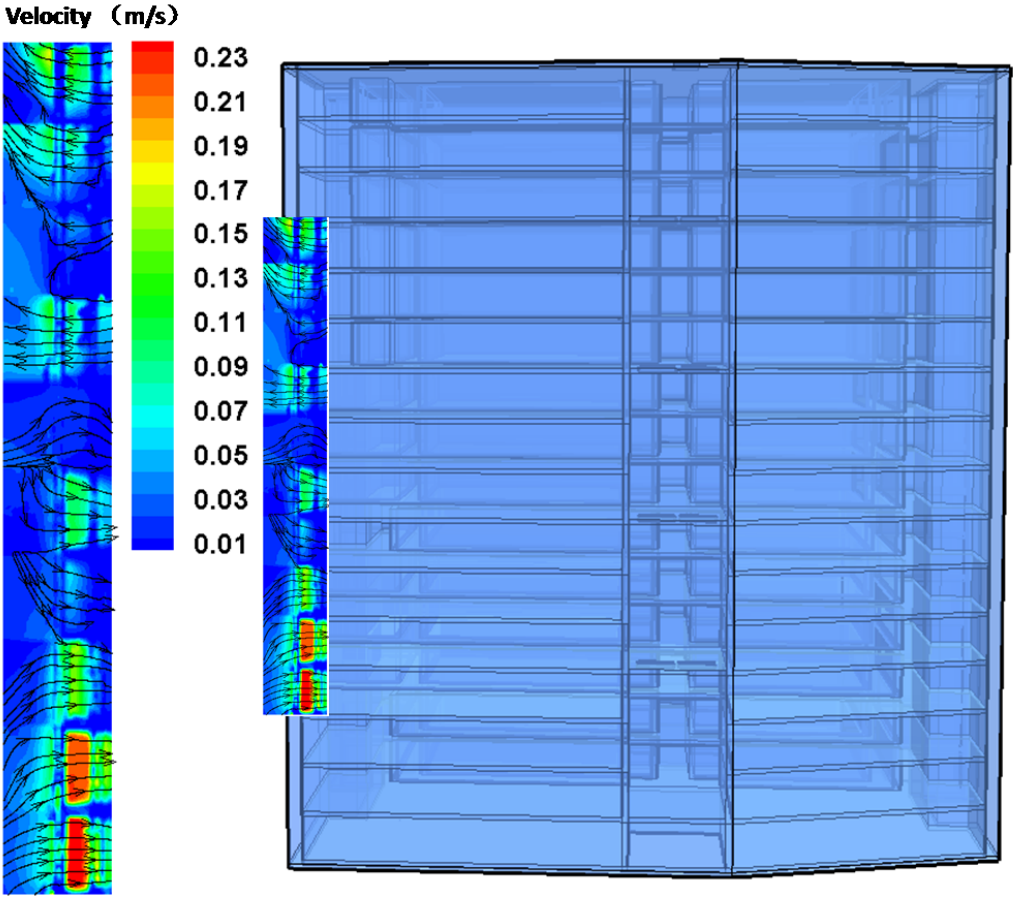


Figure 6-3. Velocity contour of flow across corridor grilles under natural ventilation conditions.

Fig. 6-4 shows the air flow velocity contour across the corridor grilles at the SE façade for the 4th to 13th floors under hybrid ventilation conditions. It was seen that the inflows at the upper floor are higher than those at the lower floors due to the effect of mechanical ventilation devices at the top of the building.

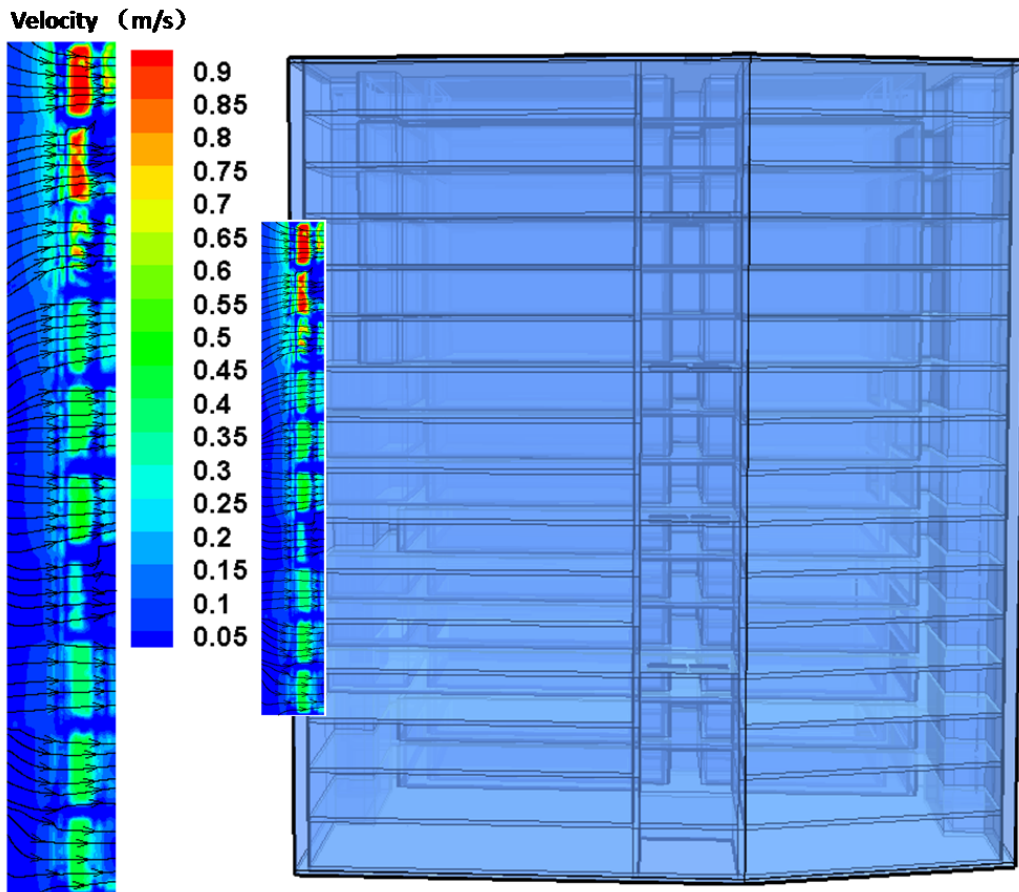


Figure 6-4. Velocity contour of flow across corridor grilles under hybrid ventilation conditions.

Airflow rates through the corridor grilles were calculated from the experimental data. Fig. 6-5 and Fig. 6-6 show the airflow rate distributions for the 4th floor to the 13th floor. From Fig. 6-5, it can be seen that from the 4th floor to the 8th floor, the flow goes inside the building, while it goes outside the building from the 10th floor to the 13th floor. The neutral plane is located at about the

ninth floor, as the flow rate in the ninth floor corridor is close to zero. It is known that the whole building consists of five three-story atriums and the neutral plane is located at the middle of the third atrium, which explains why the neutral plane is not located in the middle of the entire building. From the airflow rate results shown in Fig. 6-6, it can be calculated that the inflow rate as a whole is about $0.00289 \text{ m}^3/\text{s}$, which is about a 13.5% difference from half of the exhaust fan flow rate. Due to the structure design of the building, the flow rates at the 12th floor and 13th floor is much higher than those of the lower floors, while the inflows in the other floors' corridors are limited by the walls.

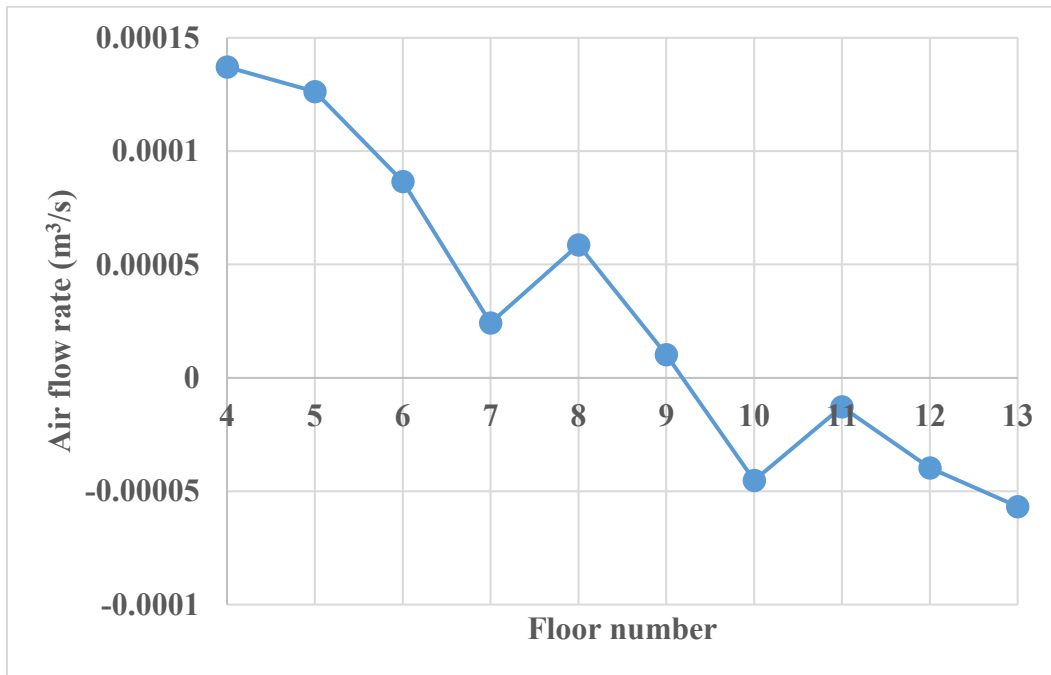


Figure 6-5. Airflow rate through the corridor grilles under natural ventilation conditions.

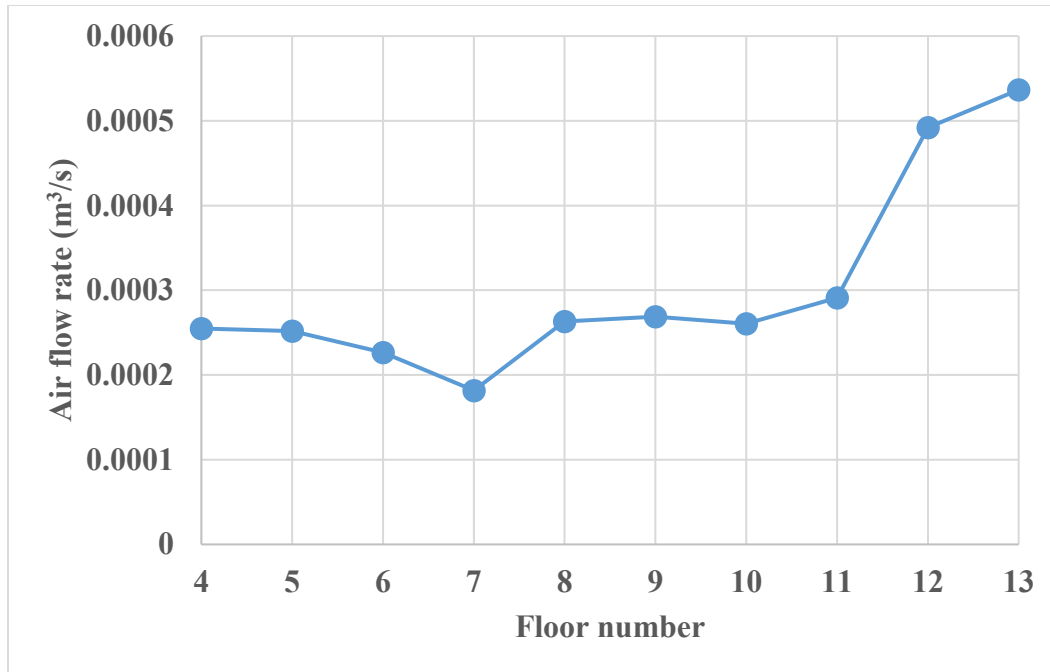


Figure 6-6. Airflow rate through the corridor grilles under hybrid ventilation conditions.

6.3.2 Temperature measurement results

Fig. 6-7 shows the temperature distribution at the atrium, offices, and corridor grilles of the building under natural and hybrid ventilation conditions. Compared to natural ventilation, it was seen from Fig. 6-7 (a) and (b) that with the effects of the exhaust fan at the top of the building, the temperatures in the corridors and atrium change significantly. A high inflow on every floor due to the mechanical ventilation device drives heat away at the corridors, which leads to decreases in temperature in those areas. As the air flow of the building is driven out through the atriums and goes out from the exhaust fan at the top floor, heat is brought to the atrium area. As the result, the temperatures in the atriums rise under hybrid ventilation conditions. With the heat exchange between the offices and the other areas, the temperature inside the offices slightly decreases due to the mechanical ventilation.

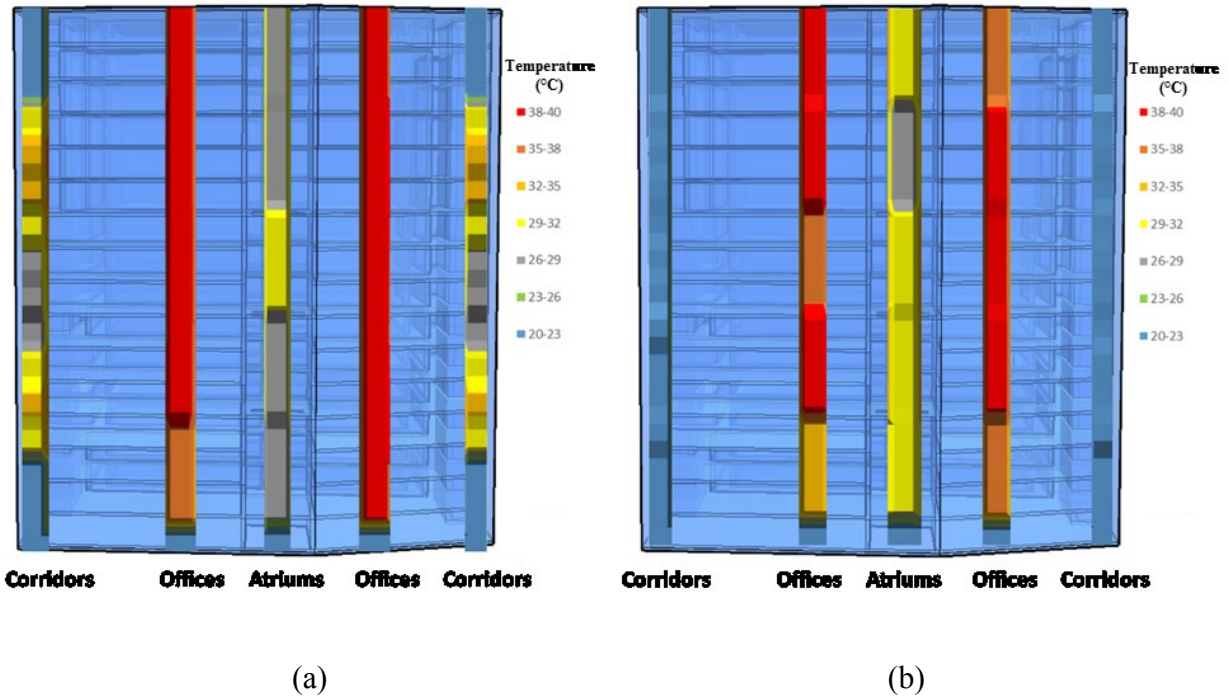


Figure 6-7. Temperature (°C) distribution in corridors, offices, and atriums: (a) natural ventilation; (b) hybrid ventilation.

6.3.3 Comparison with simulation results

Fig. 6-8 compares the natural ventilation air flow rates at the inlet dampers between the PIV experimental results and the numerical results. It is obvious that the air flow directions of two floors is opposite between the PIV and numerical results. That is because the flow coefficient used in the interior node connection equation for all the floors was the same, which can affect the simulation results. Except for the two floors with opposite air flows, the differences between the PIV results and numerical results were all in the range of 21.5% to 90.9%. The discharge coefficient used in the orifice equation is based on experience, which can be significantly different from real-world conditions. As we know, the EV building model consists of five three-floor atrium zones. Numerical results show that the minimum air flow rate happens at the middle floor of each

atrium zone, which are the 6th, 9th, and 12th floors. The PIV results show a similar phenomenon, but consider the stack effect more for the whole building model.

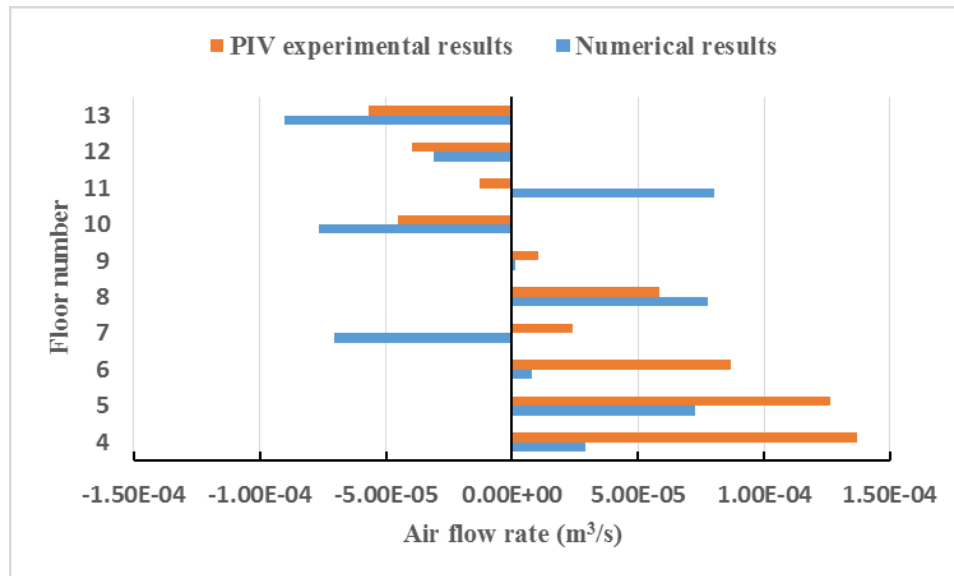


Figure 6-8. Comparison of natural ventilation air flow rates at the inlet dampers between the PIV experimental results and numerical results.

Fig. 6-9 compares the hybrid ventilation air flow rates at the inlet dampers between the PIV experimental results and the numerical results. It is obvious that the air flow directions of two floors is opposite between the PIV and numerical results. As mentioned before, that is because the flow coefficient used in the interior node connection equation for all the floors was the same, which can affect the simulation results considering the real world conditions. Except for the two floors with opposite air flows, the differences between the PIV results and the numerical results were all in the range of 1.9% to 95.6%. This wide range is due to the fact that the discharge coefficient used in the orifice equation was based on experience, which can be significantly different from real-world conditions. The numerical results also show that the minimum air flow rate happens at the middle floor of each atrium zone, which are at the sixth and ninth floors. For the upper three floors,

because of the strong effect of the mechanical fan, the flow rates are high and similar between the numerical results and the PIV results.

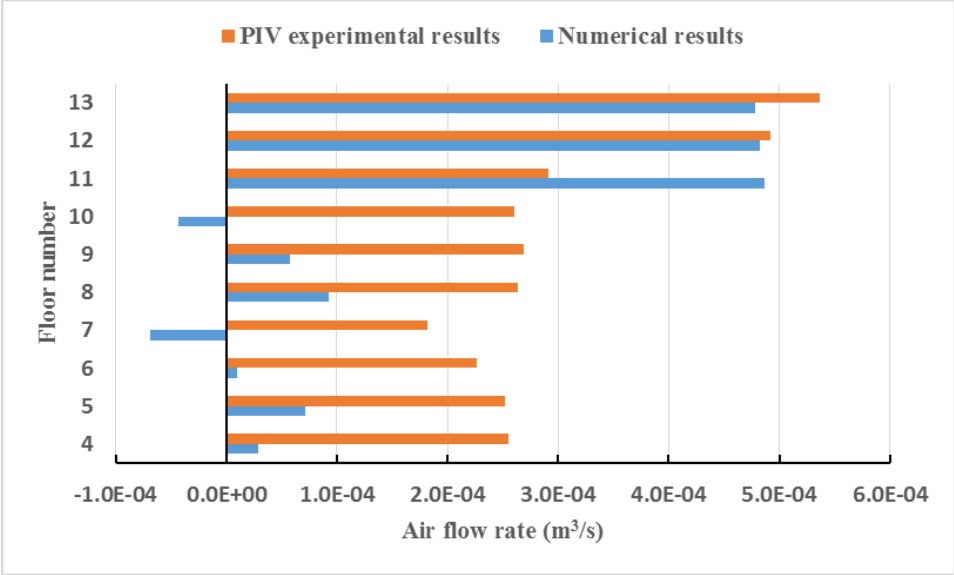


Figure 6-9. Comparison of hybrid ventilation air flow rates at the inlet dampers between the PIV experimental results and the numerical results.

6.4 Conclusions

The performance of a hybrid ventilation system in terms of airflow pattern and temperature distribution in a sub-scale 16-story building model was investigated by comparing it with the performance of natural ventilation. Inflow field patterns and flow rates for all 10 floors were measured using the PIV technique.

The PIV results of air flow rates across the openings were validated by an anemometer, and the results showed that the difference was about 13.5%. The air velocities and temperature distributions in the corridors, offices, and atriums showed that hybrid ventilation enhanced the ventilation effects, especially in the corridors and atriums, of the EV building, and promoted thermal comfort.

In addition, the PIV measurement results were used to validate the multizone numerical model. Although there were significant differences in air flow rates between the PIV measurement results and the numerical simulation results, it is possible to improve the accuracy of numerical model by modifying the flow and discharge coefficients. Further work to improve the numerical model using PIV experimental results will be done in the future.

7 MECHANICAL VENTILATION IN A SUB-SCALE WAREHOUSE

7.1 Introduction

Agriculture has covered the expansion of human population over history by boosting the productivity of crops. Despite extreme cold weather and limited natural resources in the north of Canada, there is a great need for the development of innovative agricultural technologies. In indoor warehouses, ventilation systems play an important role in providing a favorable growing environment for crops as air replacement and movement is important for promoting the photosynthesis and transpiration of plants [100-102]. However, the improper design of controlled air distribution in indoor plant factories can cause non-uniform environmental conditions and airflow distribution, which can lead to non-uniform crop growth, inconsistent quality, and crop disorders [104].

Yoshiaki Kitaya [105] assessed the effects of air velocity of less than 1.3 m/s on net photosynthetic rates, transpiration rates, and water use efficiencies of a seedlings canopy and single leaves of cucumber plants. For the cucumber seedlings canopy, the net photosynthetic rate and transpiration rate increased by 1.2 and 2.8 times respectively when the air velocity was increased from 0.02 to 1.3 m/s. For the single leaves of cucumber plants, the net photosynthetic rate and transpiration rate increased by 1.7 and 2.1 times respectively when the air velocity was increased from 0.005 to 0.8 m/s.

The interactions between multi-jet flow and crops in large warehouses are complex, so it is challenging to model using a numerical model. Also, because of the complicated models of a localized mechanical ventilation system and plant, it is hard to achieve high-accuracy results using

the CFD simulation method. Experimental measurements in sub-scale models have shown to be effective tools in simulating complex airflow phenomena with relatively high accuracy.

Angui Li et al. [106] conducted PIV measurements to investigate the air distribution influenced by multi-nozzle jets and heat sources in a 1:50 sub-scale model of a large generator hall in an underground hydropower station, and to verify the accuracy of CFD results.

The aim of this chapter is to investigate the flow distribution of localized mechanical ventilation in a warehouse. Particle image velocimetry results were used to calibrate the empirical equation so that the jet flow velocity can be predicted under different conditions.

7.2 Methodology

7.2.1 3D printing model and experimental design

As shown in Fig. 7-1, full-scale localized mechanical ventilation system tests were conducted to investigate the effects of air flow on the growth of crops. By comparing the growing behavior of crops with and without a localized air supply, it was seen that the crops under jet flows grew better and faster, with fewer withered pale green leaves.

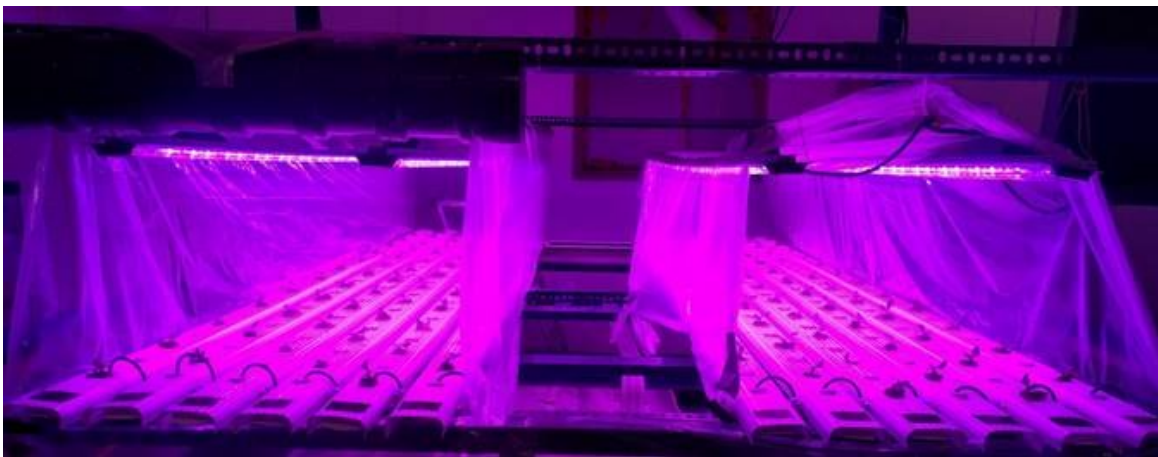


Figure 7-1. Full-scale growing bed experiment. Left: with localized air supply. Right: without localized air supply.

It should be mentioned that romaine lettuce was used in the full-scale tests. Its growing stages and corresponding dimensions were recorded as shown in Table 8. For sub-scale model experiments, the lettuce in stage 4 was made using a 3D printer as shown in Fig. 7-2.

Table 8. Romaine lettuce growth stages.

	Diameter(")	Height(")
Stage 1	2.54	1.35
Stage 2	3.58	2.08
Stage 3	5.03	3.19
Stage 4	7.08	4.89
Stage 5	9.96	7.50



Figure 7-2. 3D-printed crop model.

A sub-scale localized mechanical ventilation system was designed according to full-scale growing bed and made using a 3D printer. Table 9 shows the dimensions and air supply volume flow rates of both the sub-scale model and the full-scale model.

Table 9. Parameters of the sub-scale model and corresponding parameters of the full-scale model.

PARAMETERS	SUB-SCALE MODEL	FULL-SCALE MODEL
Total air supply volume flow rate	6.8 cfm	170 cfm
Total air supply duct numbers	6	6
Total discharge orifice numbers	69	69
Distance between ducts and crops	4.2 cm	21 cm
Diameter of the orifice	1/16 inches (1.5875 mm)	5/16 inches (7.9375 mm)
Height of the crops	3.5 cm	18 cm

7.2.2 PIV measurement setup

To visualize the fluid fields provided by the jet flow, two dimensional PIV system was used in this research. Two PIV measurement planes were set, one with dimensions of 507 mm by 380 mm (L × H) for the airflow around the whole row of plants and one with dimensions of 245 mm by 184 mm (L × H) to focus on six plants and jet inlets. The PIV system can provide the vector velocity fields of the flow around the crops by measuring the movement of particle seeds. Oil particles were used as tracer seeds and fed into a large mixed box by an atomizer. Compressed air was injected into the same mixed box after it was full of particle seeds.

In the PIV technique, the time interval between two different laser pulses should be set properly for different cases according to the maximum velocity of the measured flow fields. Based on the preliminary tests, the time interval between one pair of pictures, Δt , was set to 50, 100, 200, and 300 μs for cases 1 through 4. For each PIV case, 100 frame pairs (200 images) were captured. The interrogation area was selected to be 16 × 16 pixels. More PIV measurement parameters are shown in Table 10.

Because of the non-transparent crop model blocking the laser sheet, it was difficult to capture the flow field between the crops. As shown in Fig. 7-3, with the help of mirror, it was possible to measure the air velocity above the plants and between the plants at the same time.

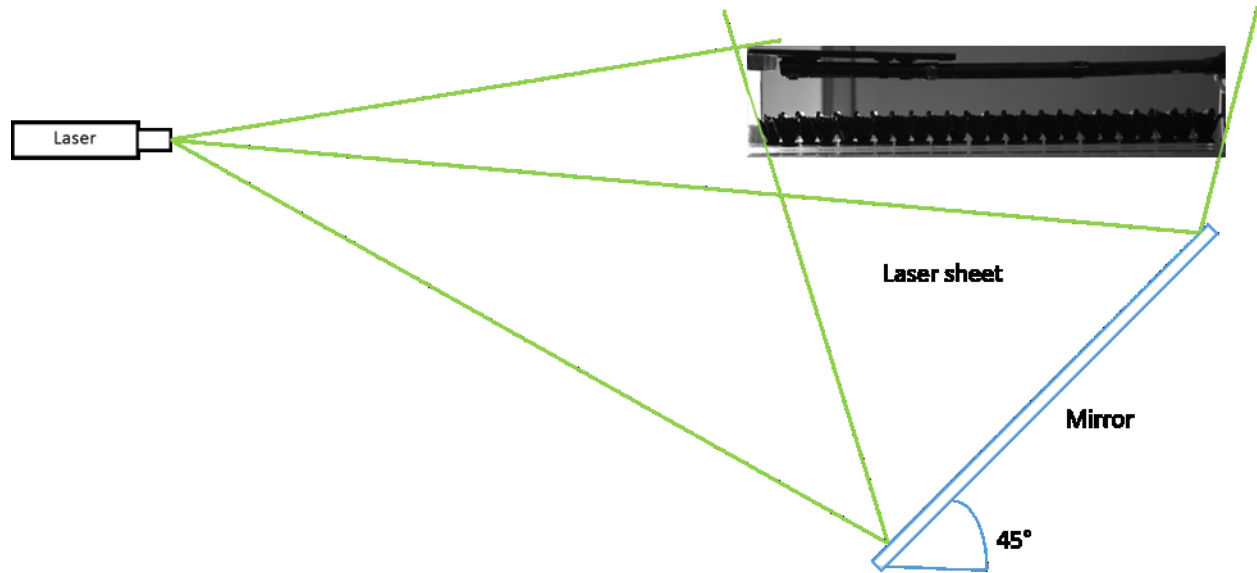


Figure 7-3. Schematic PIV experiment setup.

Table 10. Setup of PIV data acquisition and evaluation.

	Measurement Plane1	Measurement Plane2
Field of view	507 mm by 380 mm	245 mm by 184 mm
Delay time (Δt)	50, 100, 200, 300 μ s	50, 100, 200, 300 μ s
Sampling frequency	15 Hz	15 Hz
Number of captured pictures	100 frames	100 frames
Interrogation window	16 pixels by 16 pixels	16 pixels by 16 pixels
Overlap	25%	25%
Measured time	7 s	7 s

7.2.3 CFD simulations

The indoor airflow of a large space warehouse was investigated using Reynolds-Averaged Navier-Stokes (RANS) methods.

A CFD model was built using ANSYS Fluent 18.1 as shown in the Fig. 7-4. Unstructured grids were meshed using ANSYS Workbench. The multi-jet supply was modeled as velocity inlet for which the mass flow rate was the same as in a real warehouse design. In addition, the lateral boundary was set as a pressure outlet, as it is the boundary of the whole warehouse. A standard $k-\varepsilon$ turbulence model was chosen to simulate the three-dimensional multi-jet flow velocity.

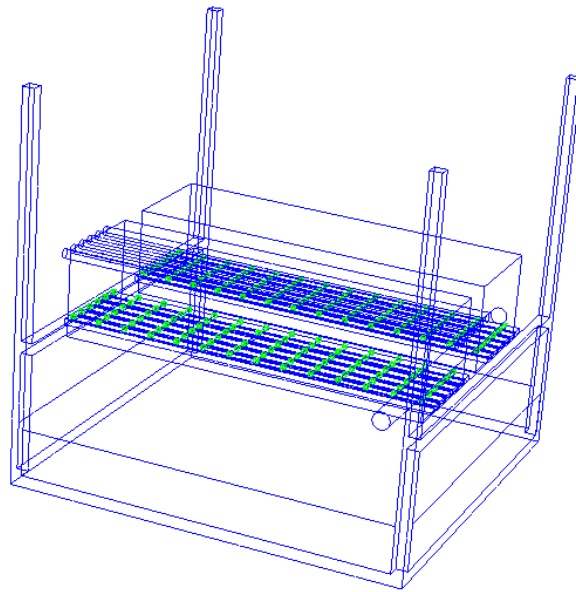


Figure 7-4. Schematic view of the growing bed model.

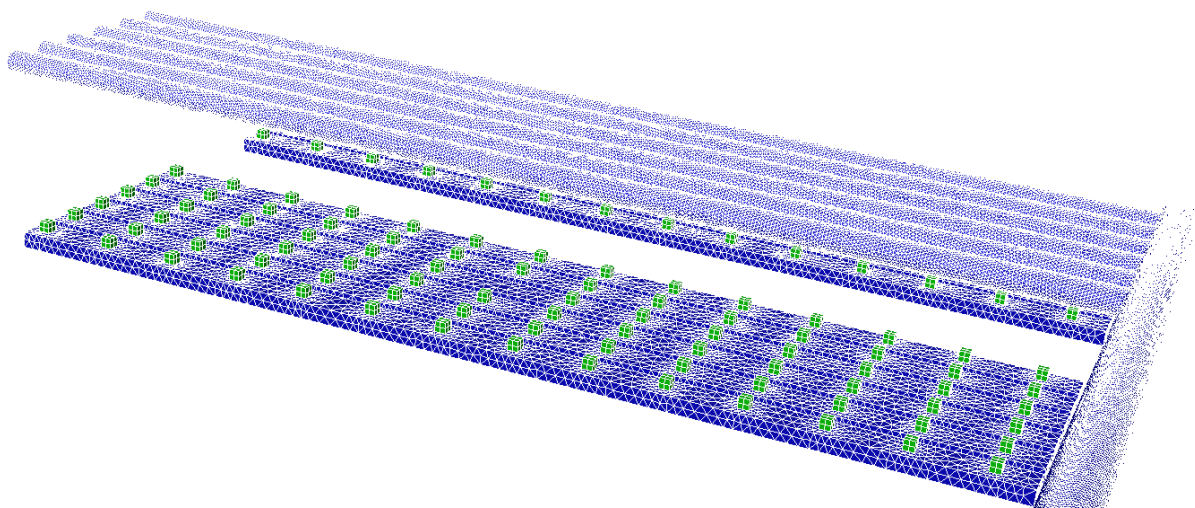


Figure 7-5. Mesh structure of the air supply system and growing bed.

7.2.4 Single jet flow empirical model

The structure of the round free jet has been studied by many researchers [106-110], as shown in Fig. 7-6 [107]. There are three different regions that can be defined: the near field, the intermediate field, and the far field. The near field consists of a mixing region surrounding the potential core of the flow. In the intermediate field, the entire jet is a mixing region, and the central velocity decreases as x increases. In the far-field region, velocity profiles and the x gradient of u_0 finally reach an asymptotic state as the fluid enters the fully-developed zone, where the central velocity is inversely proportional to the distance from a point near the orifice inlet, and all profiles are similar.

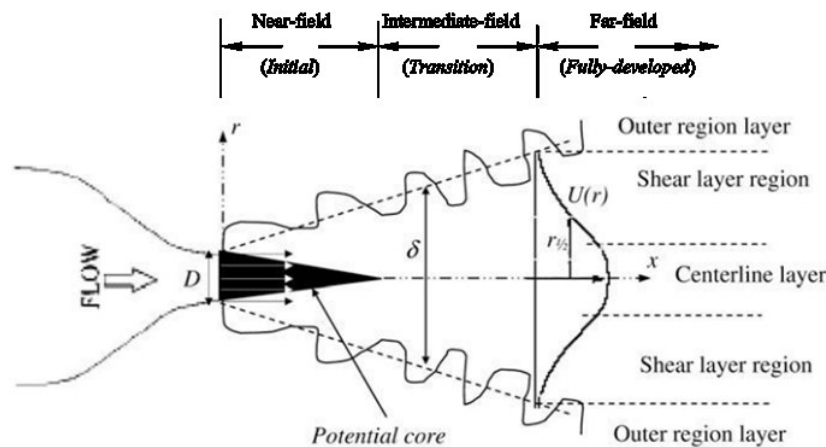


Figure 7-6. Schematic of the round free jet.

For predicting the multi-jet mechanical ventilation system performance, an empirical model had to be used and modified by experimental results. For this study, the empirical equation used was obtained from the book written by Zengji Cai et al. [111].

The jet centerline velocity attenuation formula is:

$$\frac{u_m}{u_0} = \frac{0.48}{\frac{ax}{d_0} + 0.147}. \quad \text{Eq. 7-1}$$

The jet diameter variation formula is:

$$\frac{D_0}{d_0} = 6.8\left(\frac{ax}{d_0} + 0.147\right). \quad \text{Eq. 7-2}$$

In the equations shown above, u_0 is the discharge velocity of the orifice, u_m is the centerline velocity of the jet, d_0 is the diameter of orifice, D_0 is the jet flow diameter, x is the distance from the orifice, and a is a coefficient obtained from an experiment.

7.3 Results and discussions

7.3.1 CFD simulation results

Air distribution generated from a multi-jet system in the sub-scale and full-scale warehouse models was simulated by CFD Fluent. Fig. 7-7 shows the steady-state flow velocity contour inside and outside the multi-nozzle tube, which was the closest to the air supply entrance of the whole system. From Fig. 7-7 (a), it can be seen that the nozzle jets were sent out from the inlets and mixed with the ambient air. With an air supply flow rate of 170 cfm for the whole system, the jet velocities were about 35 m/s at the nozzle, and were weakened in the distance between the tubes and the ground surface of 50 cm. Similar flow pattern can be observed in Fig. 7-7 (b), in which the jet flows were generated with a sub-scale system model.

Fig. 7-8 (a) and (b) show the 3D jet flow streamlines for the whole mechanical ventilation system. As shown in Fig. 7-8, all the jet flows were separated because of their interactions with other jets, the existence of crops, and the flat surface.

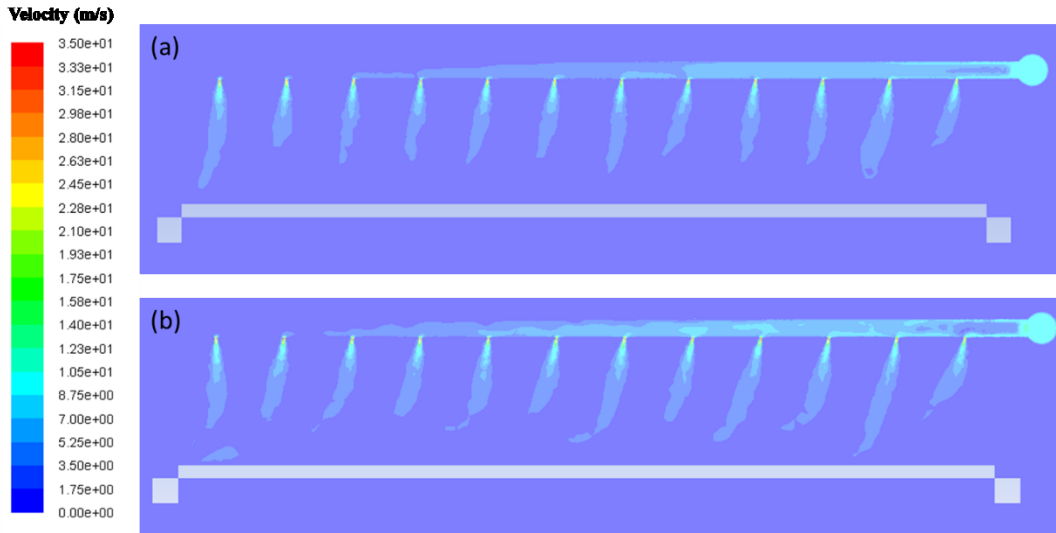


Figure 7-7. Simulated velocity field contours: (a) full-scale model; (b) sub-scale model.

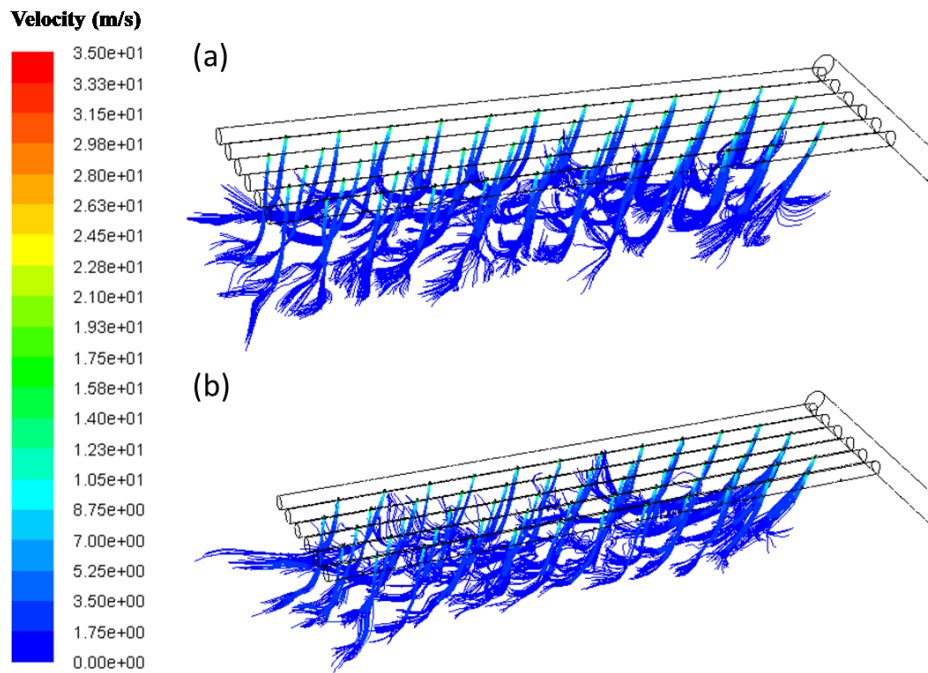


Figure 7-8. Simulated 3D velocity field streamlines: (a) full-scale model; (b) sub-scale model.

From Fig. 7-9, it can be seen that the 12 jet air flow rates of the tube closest to the air supply entrance of the whole system for full-scale simulation and sub-scale simulation were similar. Also, the flow rate distribution was uniform according to the simulation results. The difference between the largest air flow rate and the smallest air flow rate was less than 10%.

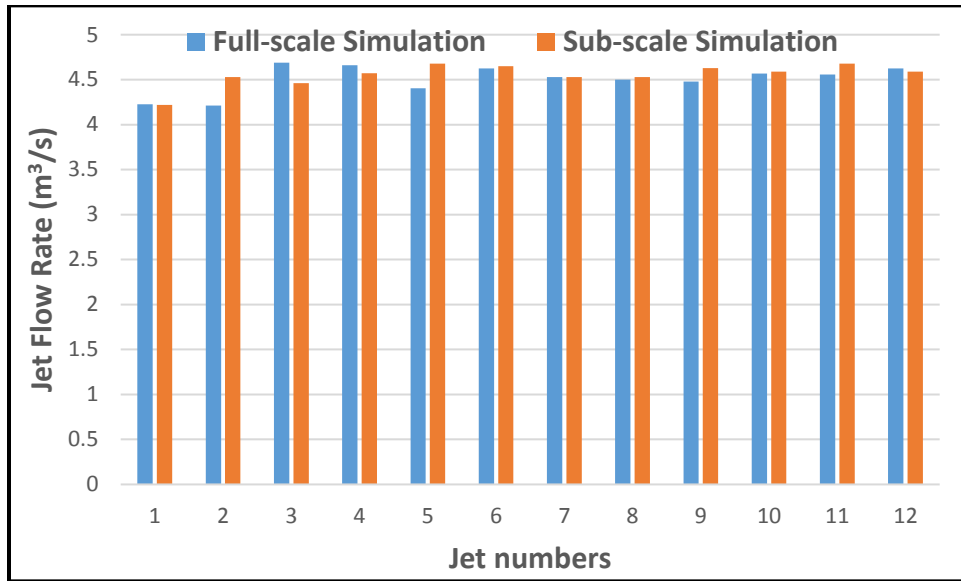


Figure 7-9. Jet flow rates for the full-scale model and the sub-scale model.

According to the CFD simulations, the air distribution in the warehouse with localized mechanical ventilation for the sub-scale model and full-scale model was similar, comparing the flow patterns and air flow rates. Also, the jet flow rate distributions at the nozzles were almost uniform, so that every crop would receive a similar localized mechanical ventilation flow rate.

7.3.2 Flow field measurement results

Flow field in the warehouse model can be visualized by the PIV system. As shown in Fig. 7-10, the jet flows were supplied towards every crop model. The jet structures remained complete until reaching the crops.

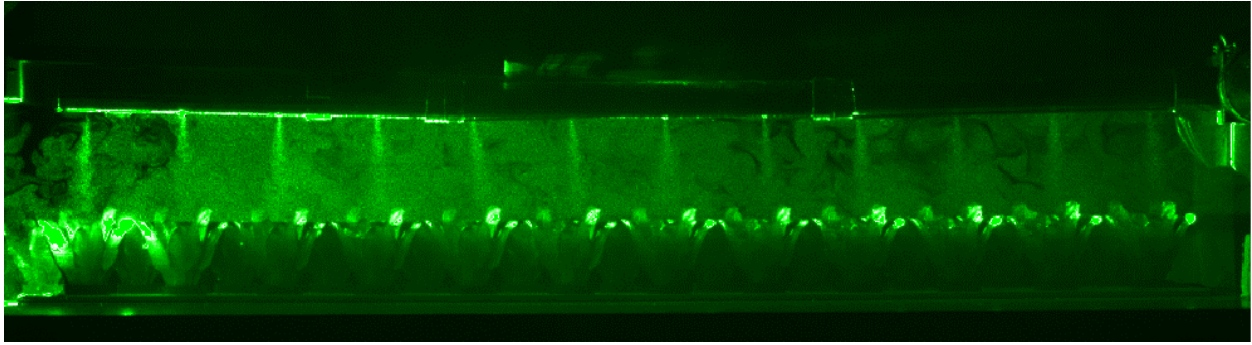


Figure 7-10. Visualization of the flow field with 6.8 cfm air supply flow rate.

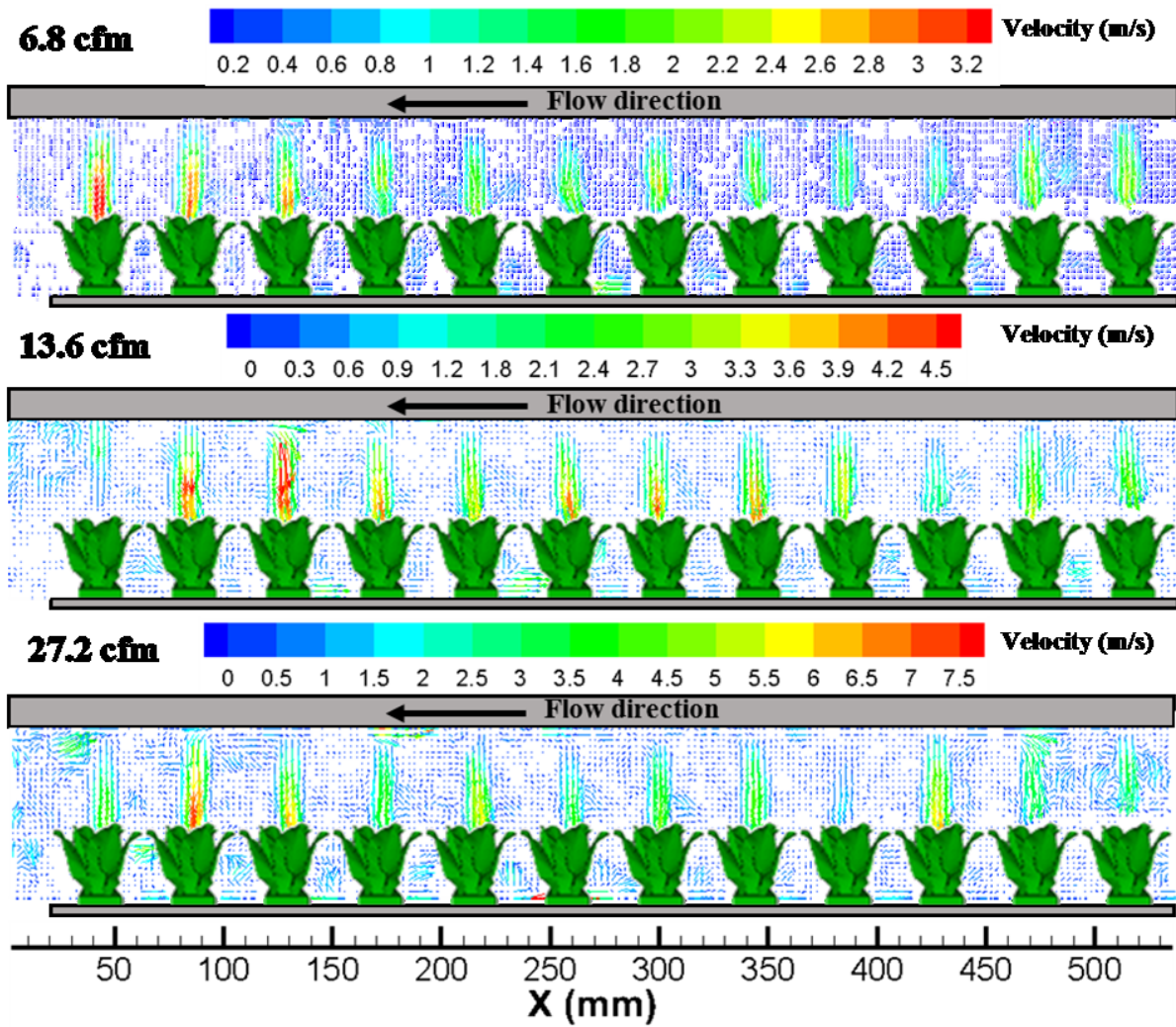


Figure 7-11. Flow field vectors measured by PIV.

Fig. 7-11 shows the flow velocity field vectors at different air supply velocities for cases 2 and 3. The flow patterns agree with the CFD simulation results that the jet flow distributions were almost uniform.

For quantitative analysis, PIV measurements for smaller fields of view were conducted and the results with a higher resolution were obtained. Fig. 7-12 shows the air flow velocity contours with different air supply velocities for cases 1 through 4. The air flow patterns in the four cases are very similar to each other. As seen in Fig. 7-12, the jet flow velocities are remarkably low near the crops because of collisions with the upward flows near the leaves of crops.

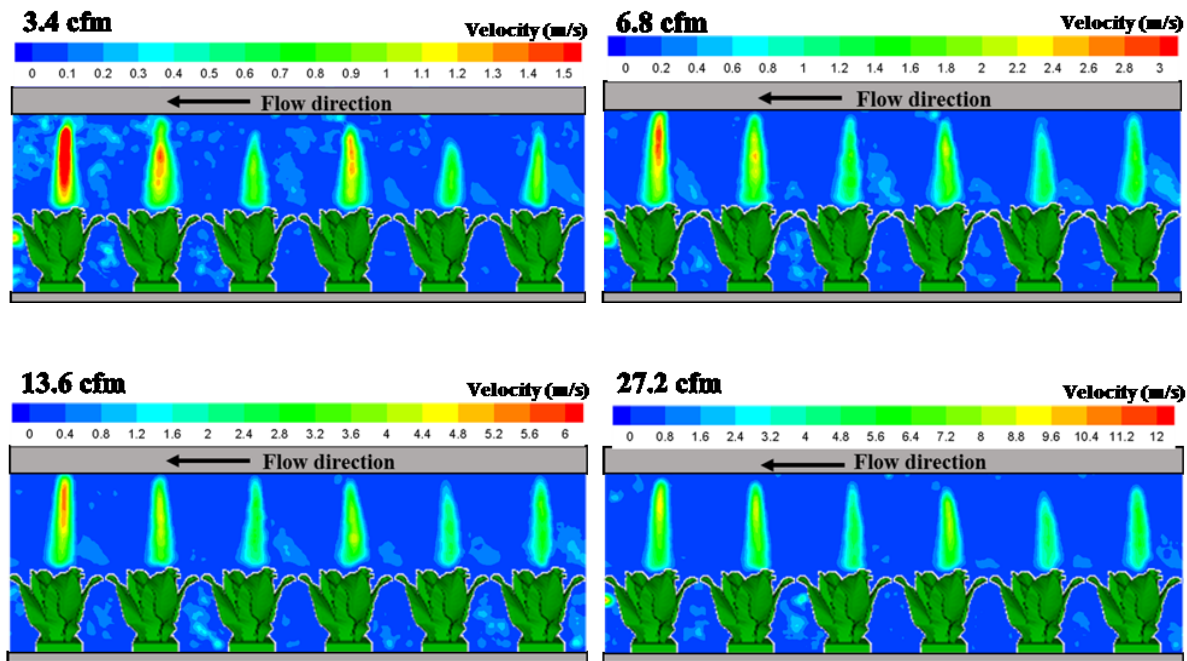


Figure 7-12 Flow field contours measured by PIV

7.3.3 PIV data correlation results

As shown in Fig. 7-13, the dimensionless average centerline velocity along with the dimensionless distance from the nozzle were extracted from the PIV data. The centerline velocity used in the

figure was calculated from the average of six jet centerline velocities. The air velocities near the crops with a distance larger than $23d_0$ from the nozzles decayed at an extremely high gradient. This is because of the upwards flows near the crops. The jet velocity close to the point near the orifice inlet was low due to the limitations of PIV technique in measuring high jet velocities. A correlation curve was made based on the PIV data and the empirical model. The turbulence coefficient used in the empirical equation was 0.43. As shown in Fig. 7-13, the correlation curve was an acceptable fit with the experimental results in the fully-developed region until the area close to the crop leaves, which was about $23d_0$ from the nozzle inlet.

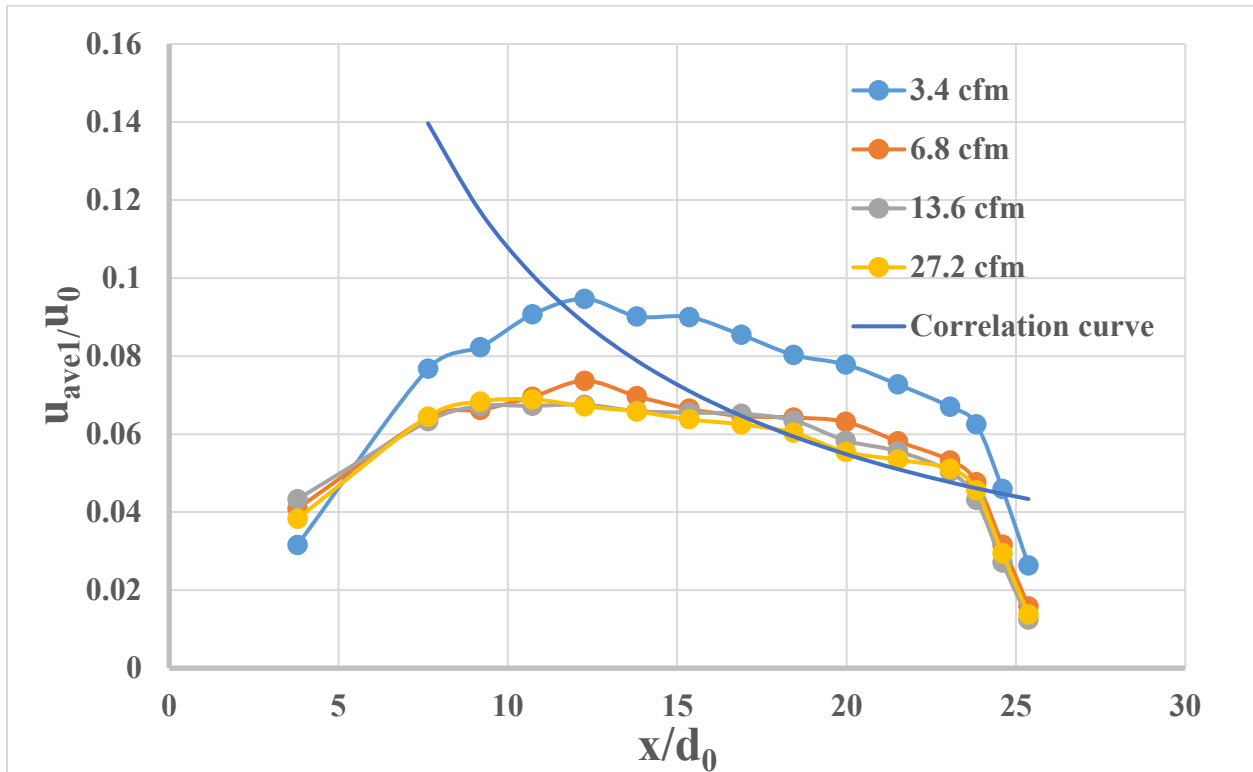


Figure 7-13. Dimensionless centerline velocity below the nozzle inlet.

Fig. 7-14 shows the dimensionless average jet velocities along the dimensionless distance from the nozzle. The jet velocities were calculated using the average of the velocities on the jet widths

for all six jets. It can be seen that all the four experimental curves were similar. Also, a correlation curve was made according to the PIV data and the empirical model. The turbulence coefficient used in the empirical equation was 0.6. Similar to Fig. 7-13, the correlation results agreed with the experimental results from the fully-developed region to the area close to the crop leaves, which was about $23d_0$ from the nozzle inlet.

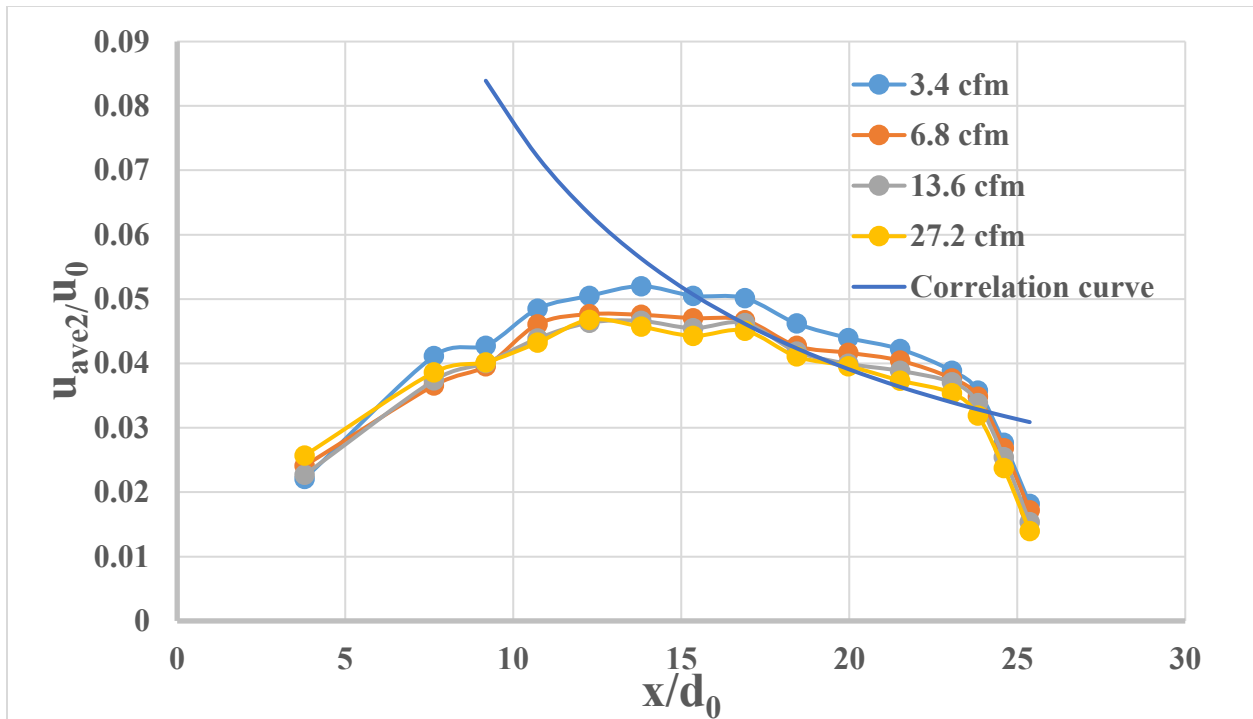


Figure 7-14. Dimensionless centerline velocity below the nozzle inlet.

Fig. 7-15 shows the dimensionless average jet diameters along the dimensionless distance from the orifice inlet. The jet diameters were calculated using the average of the width of all six jets. From Fig. 7-15, it can be seen that the width of the jets increased from the orifice until the distance to the crop models were decreased to $2d_0$. Based on the empirical equation, a correlation curve was made to fit the experimental data. According to the jet theory, the turbulence coefficient a is the

same in the empirical equation for jet centerline velocity decay. Therefore, 0.6 was used in the equation for jet diameter increasing.

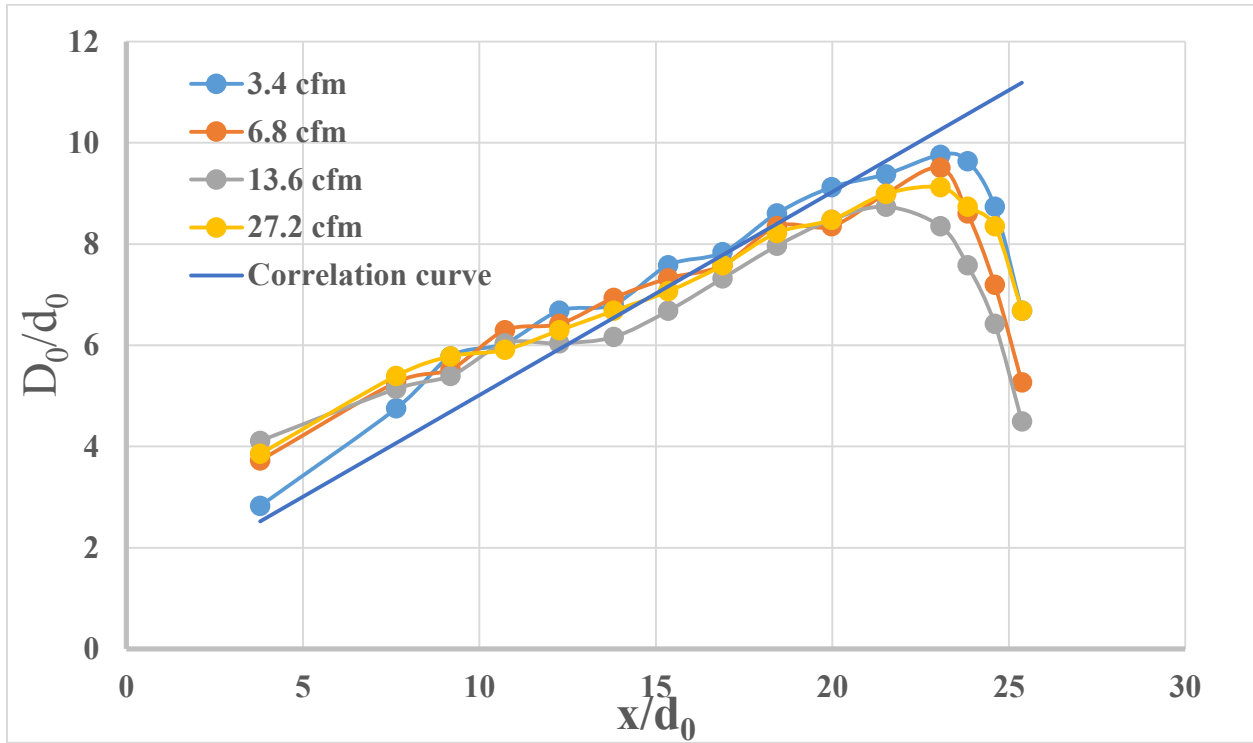


Figure 7-15. Dimensionless jet diameter.

For the prediction of the localized mechanical ventilation system performance, Table 11 was created according to the empirical model modified by the experimental data. With the help of a verified empirical formula, the duct inlet volume flow rate, the distance between the orifices and crops, the orifice diameter, and the jet coverage diameter can be predicted according to different goals, for example, achieving a flow rate of 2 m/s on top of the crops.

Table 11 Localized mechanical ventilation system performances according to modified empirical models

2m/s air flow velocity around plant (5mm above plant)										
		Sub-scale results				Full-scale results				
Distance between orifice and crop	Diameter of orifice	1d (1/16 inches) (1.5875 mm)	2d (1/8inches) (3.175 mm)	3d (3/16 inches) (4.7625 mm)	4d (1/4inches) (6.35 mm)	1D (5/16 inches) (7.9375 mm)	2D (5/8 inches) (15.875 mm)	3D (15/16 inches) (23.8125 mm)	4D (5/4 inches) (31.75 mm)	Distance between orifice and crop
	Area of orifice	1a	4a	9a	16a	1A	4A	9A	16A	
16d (1 inches) (2.54 cm)	Duct inlet volume flow rate (cfm)	9.1191	18.5926	28.4207	38.6032	227.9767	464.8158	710.5173	965.0811	16D (5 inches) (12.7 cm)
	Orifice inlet velocities(m/s)	31.5121	16.0623	10.9124	8.3374	31.5121	16.0623	10.9124	8.3374	
	Jet coverage diameter(m)	0.0094	0.0110	0.0126	0.0141	0.0469	0.0548	0.0628	0.0707	
21d (1.3125 inches) (3.33 cm)	Duct inlet volume flow rate (cfm)	12.7603	25.8751	39.3445	53.1683	319.0081	646.8786	983.6115	1329.2068	21D (6.5625 inches) (16.67 cm)
	Orifice inlet velocities(m/s)	44.0949	22.3537	15.1066	11.4831	44.0949	22.3537	15.1066	11.4831	
	Jet coverage diameter(m)	0.0125	0.0141	0.0157	0.0173	0.0627	0.0707	0.0786	0.0865	
26d (1.625 inches) (4.1275 cm)	Duct inlet volume flow rate (cfm)	16.4362	33.2268	50.3719	67.8716	410.9038	830.6699	1259.2985	1696.7894	26D (8.125 inches) (20.64 cm)
	Orifice inlet velocities(m/s)	56.7971	28.7048	19.3407	14.6587	56.7971	28.7048	19.3407	14.6587	
	Jet coverage diameter(m)	0.0158	0.0173	0.0189	0.0205	0.0788	0.0867	0.0946	0.1026	
31d (1.9375 inches) (4.921 cm)	Duct inlet volume flow rate (cfm)	20.0935	40.5416	61.3441	82.5011	502.3385	1013.5394	1533.6027	2062.5283	31D (9.6875 inches) (24.6 cm)
	Orifice inlet velocities(m/s)	69.4357	35.0241	23.5536	17.8183	69.4357	35.0241	23.5536	17.8183	
	Jet coverage diameter(m)	0.0189	0.0205	0.0221	0.0237	0.0947	0.1026	0.1106	0.1185	

8 DISCUSSION AND CONCLUSIONS

8.1 Conclusions

The objective of this thesis is to provide an overview of the typical two dimensional PIV technique used in building environment research. First, a two dimensional PIV system, including the illumination system, image recording devices, tracer gas, and the generator for the gas, was developed for sub-scale model experiments. According to previous studies, the PIV measurement procedures are summarized in the following steps: preparation of the PIV system and testing model, setup of devices with high precision, calibration of the camera, flow visualization before data acquisition to check the model reflection and seed tracking behaviors, image acquisition, data pre-processing, data evaluation, and post-processing for data validation, quantitative analysis and better presentation. Factors that may create errors and uncertainties or affect the accuracy of the PIV results were also discussed in this thesis.

Four problems were investigated to show different applications of the PIV technique in measuring airflow fields. These showed that PIV is a very effective tool for investigating the ventilation performance of buildings. For buoyancy-driven naturally ventilated single-zone sub-scale models, PIV was able to capture the entire indoor flow field. Accurate velocity vector information can be measured in a smaller field of view with a higher resolution. Additionally, the airflow rate across an opening as measured using PIV techniques can be validated using the tracer gas method, and the difference between the results obtained by the two experimental methods in this study was about 12%. To measure the ventilation air flow of a complicated high-rise building, PIV experiments must be conducted in several measured planes. A time-average velocity field for every

floor can be captured by combining the results. The results were validated by an anemometer, and the difference was about 13.5%.

Particle image velocimetry is also suitable for studying jet flow characteristics, including single jet interactions with wind and multi-jet interactions with obstructions. Flow structure can be investigated by flow pattern visualization. Also, PIV can be used to measure jet flow velocity vector fields. Because of the self-similar behavior of jet flows, an empirical equation correlated with PIV data was used to predict jet flow behavior at the fully-developed region.

Overall, the quantitative and detailed flow information obtained by PIV can be used for flow pattern visualization, flow structure analysis, numerical model validation, and empirical model correlation. The whole procedure in PIV experimental studies for building airflow environments is shown in Fig. 8-1. However, limitations involved in PIV techniques and sub-scale model experiments must be optimized for further studies.

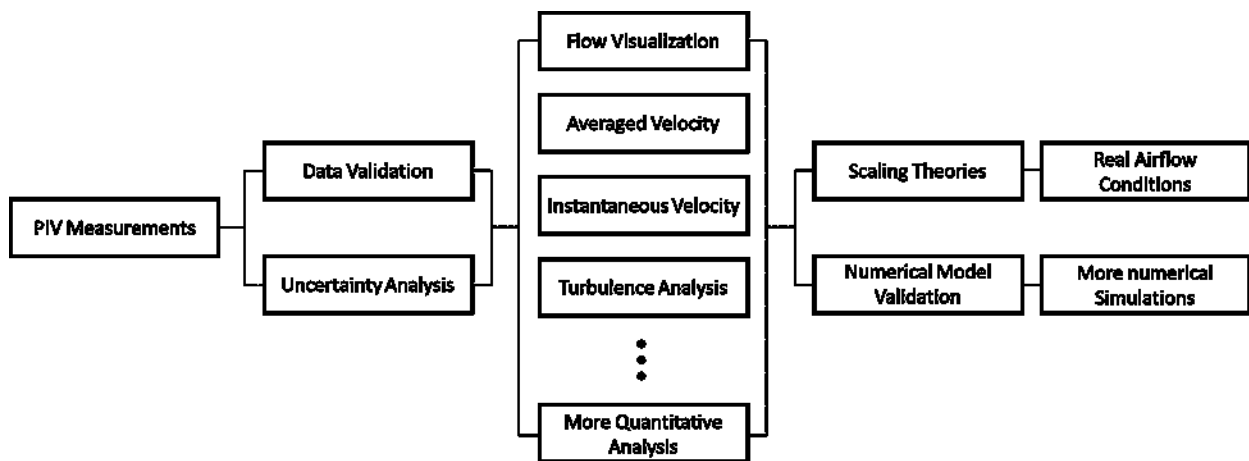


Figure 8-1. Procedure for PIV experimental studies in sub-scale building model airflow environments.

8.2 Contributions of this study

- A common procedure for the application of typical 2D PIV in building ventilation performance analyses is developed based on the case studies.
- A detailed operation guide to 2D PIV measurement using Dantec DynamicStudio software is developed. Researchers without experience using 2D PIV systems are able to obtain high-quality results by following the guide.
- Applied PIV technique in almost all the typical problems in building airflow field analysis[7]: ventilation devices, single jet flow, multi-jet flow, thermal airflow, natural ventilation, mechanical ventilation, and hybrid ventilation, except for airflow around persons.
- The relationship between PIV measurements and the analytical model, the empirical model, the multizone model, and the CFD model is discussed. This information can act as a reference to other researchers who are interested in numerical models.

8.3 Limitations of the study

Limitation of the scaling theory:

As sub-scale models experiments may suffer from scaling problems associated with buoyancy forces and time, it is essential to develop the scaling theory. Otherwise, sub-scale results may not accurately represent real conditions, and it may be difficult to directly use them in real problems.

Limitation of the experiment devices:

Three-dimensional PIV and large scale PIV experiment systems and testing procedures require further study as a result of the requirement for high quality and accuracy measurement results for the flow fields of building environments.

Limitation of experiment errors and uncertainties:

The accuracy of PIV measurements is complex. More parameters and methods should be discussed to reduce errors and uncertainties.

8.4 Future work

This study presented different applications of PIV techniques and combined them with other experimental methods and assessment models. For future work, a few items can be investigated further as follows:

- Developing scaling theory and equations considering buoyancy-driven flows by conducting multi-scale PIV experiments,
- Investigating airflow in unsteady states by applying turbulence analysis methods to the PIV technique,
- Conducting quantitative analysis of the air curtain results obtained by the CFD model to investigate the effects of wind on air curtain performance,
- Investigating the effects of the distance between air jets and crops and orifice diameters by conducting more PIV measurements to validate the modified empirical models in the localized mechanical ventilation study case,
- Investigating the effects of temperature and humidity on the jet flow performance for single jet and multi jet study cases, and
- Improving the accuracy of the multizone model for EV building hybrid ventilation performance prediction.

REFERENCES

- [1] A. Baskaran and A. Kashef, “Investigation of air flow around buildings using computational fluid dynamics techniques,” *Eng. Struct.*, vol. 18, no. 11, pp. 861–875, 1996.
- [2] P. J. Jones and G. E. Whittle, “Computational fluid dynamics for building air flow prediction-current status and capabilities,” *Build. Environ.*, vol. 27, no. 3, pp. 321–338, 1992.
- [3] Q. Chen, “Ventilation performance prediction for buildings: A method overview and recent applications,” *Build. Environ.*, vol. 44, no. 4, pp. 848–858, 2009.
- [4] Q. Chen *et al.*, “Ventilation performance prediction for buildings: Model assessment,” *Build. Environ.*, vol. 45, no. 2, pp. 295–303, 2010.
- [5] B. Blocken, T. Stathopoulos, and J. P. A. J. van Beeck, “Pedestrian-level wind conditions around buildings: Review of wind-tunnel and CFD techniques and their accuracy for wind comfort assessment,” *Build. Environ.*, vol. 100, pp. 50–81, 2016.
- [6] S. Fu, P. H. Biwole, and C. Mathis, “Particle tracking velocimetry for indoor airflow field: A review,” *Build. Environ.*, vol. 87, pp. 34–44, 2015.
- [7] X. Cao, J. Liu, N. Jiang, and Q. Chen, “Particle image velocimetry measurement of indoor airflow field: A review of the technologies and applications,” *Energy and Buildings*. 2014.
- [8] G. Gan, “Evaluation of room air distribution systems using computational fluid dynamics,” *Energy Build.*, vol. 23, no. 2, pp. 83–93, 1995.
- [9] L. Zhao, Y. Zhang, X. Wang, G. L. Riskowski, and L. L. Christianson, “Development of PIV techniques to measure airflow patterns in ventilated airspaces,” *ASHRAE Trans.*, vol.

105, 1999.

- [10] Y. Sun and Y. Zhang, “An Overview of Room Air Motion Measurement: Technology and Application,” *HVAC&R Res.*, vol. 13, no. 6, pp. 929–950, 2007.
- [11] R. J. Hansman, R. S. Figliola, P. H. Sydenham, and R. H. Dieck, “Measurement , Instrumentation & Sensors Contents Measurement Characteristics,” *Measurement*, 1999.
- [12] H. Mittal, A. Sharma, and A. Gairola, “A review on the study of urban wind at the pedestrian level around buildings,” *J. Build. Eng.*, vol. 18, no. March, pp. 154–163, 2018.
- [13] J. K. Markus Raffel, Christian E. Willert, Steve T. Wereley, *Particle Image Velocimetry*. 2007.
- [14] R. J. Adrian, “Twenty years of particle image velocimetry,” *Exp. Fluids*, vol. 39, no. 2, pp. 159–169, 2005.
- [15] P. A. Elvsén and M. Sandberg, “Buoyant jet in a ventilated room: Velocity field, temperature field and airflow patterns analysed with three different whole-field methods,” *Build. Environ.*, vol. 44, no. 1, pp. 137–145, 2009.
- [16] A. Meslem, I. Nastase, and F. Allard, “Passive mixing control for innovative air diffusion terminal devices for buildings,” *Build. Environ.*, vol. 45, no. 12, pp. 2679–2688, 2010.
- [17] L. D. Montoya, J. L. Jackson, and M. Amitay, “Control of aerosol dispersion and removal in a room using synthetic jet actuators,” *Build. Environ.*, vol. 45, no. 1, pp. 165–175, 2010.
- [18] G. Cao, M. Sivukari, J. Kurnitski, M. Ruponen, and O. Seppänen, “Particle Image Velocimetry (PIV) application in the measurement of indoor air distribution by an active chilled beam,” *Build. Environ.*, vol. 45, no. 9, pp. 1932–1940, 2010.

- [19] G. Cao, M. Sivukari, J. Kurnitski, and M. Ruponen, "PIV measurement of the attached plane jet velocity field at a high turbulence intensity level in a room," *Int. J. Heat Fluid Flow*, 2010.
- [20] E. Nino, R. Fasanella, and R. M. Di Tommaso, "Submerged rectangular air jets as a particulate barrier," *Build. Environ.*, vol. 46, no. 11, pp. 2375–2386, 2011.
- [21] A. Meslem, A. Dia, C. Beghein, M. El Hassan, I. Nastase, and P. J. Vialle, "A comparison of three turbulence models for the prediction of parallel lobed jets in perforated panel optimization," *Build. Environ.*, vol. 46, no. 11, pp. 2203–2219, 2011.
- [22] I. Nastase, A. Meslem, I. Vlad, and I. Colda, "Lobed grilles for high mixing ventilation - An experimental analysis in a full scale model room," *Build. Environ.*, vol. 46, no. 3, pp. 547–555, 2011.
- [23] D. Kumlutaş, Z. H. Karadeniz, and F. Kuru, "Investigation of flow and heat transfer for a split air conditioner indoor unit," *Appl. Therm. Eng.*, vol. 51, no. 1–2, pp. 262–272, 2013.
- [24] N. Chami and A. Zoughaib, "Modeling natural convection in a pitched thermosyphon system in building roofs and experimental validation using particle image velocimetry," *Energy Build.*, vol. 42, no. 8, pp. 1267–1274, 2010.
- [25] C. Sanjuan, M. J. Suárez, E. Blanco, and M. D. R. Heras, "Development and experimental validation of a simulation model for open joint ventilated façades," *Energy and Buildings*, vol. 43, no. 12, pp. 3446–3456, 2011.
- [26] C. Sanjuan, M. N. Sánchez, M. del R. Heras, and E. Blanco, "Experimental analysis of natural convection in open joint ventilated façades with 2D PIV," *Building and Environment*, vol. 46, no. 11, pp. 2314–2325, 2011.

- [27] D. Marr, H. Higuchi, T. Khan, J. Zhang, and M. Glauser, "On Particle Image Velocimetry (PIV) measurements in the breathing zone of a thermal breathing manikin," *ASHRAE Trans.*, vol. 111 PART 2, pp. 299–305, 2005.
- [28] D. R. Marr, I. M. Spitzer, and M. N. Glauser, "Anisotropy in the breathing zone of a thermal manikin," *Exp. Fluids*, vol. 44, no. 4, pp. 661–673, 2008.
- [29] D. R. Marr and M. N. Glauser, "Length scale propagation along a joint inlet and thermal buoyancy driven flow," *Proc. ASME Fluids Eng. Div. Summer Meet. 2006, FEDSM2006*, vol. 1 SYMPOSIA, pp. 127–132, 2006.
- [30] O. Özcan, K. E. Meyer, and A. K. Melikov, "A visual description of the convective flow field around the head of a human," *J. Vis.*, vol. 8, no. 1, pp. 23–31, 2005.
- [31] A. D. Eisner, J. Rosati, and R. Wiener, "Experimental and theoretical investigation of particle-laden airflow under a prosthetic mechanical foot in motion," *Build. Environ.*, vol. 45, no. 4, pp. 878–886, 2010.
- [32] S. W. Zhu, S. Kato, and J. H. Yang, "Study on transport characteristics of saliva droplets produced by coughing in a calm indoor environment," *Build. Environ.*, vol. 41, no. 12, pp. 1691–1702, 2006.
- [33] B. A. Craven and G. S. Settles, "A Computational and Experimental Investigation of the Human Thermal Plume," *J. Fluids Eng.*, vol. 128, no. 6, p. 1251, 2006.
- [34] C. Y. H. Chao *et al.*, "Characterization of expiration air jets and droplet size distributions immediately at the mouth opening," *J. Aerosol Sci.*, vol. 40, no. 2, pp. 122–133, 2009.
- [35] M. Vansciver, S. Miller, and J. Hertzberg, "Particle image velocimetry of human cough," *Aerosol Sci. Technol.*, vol. 45, no. 3, pp. 415–422, 2011.

- [36] S. B. Kwon *et al.*, “Study on the initial velocity distribution of exhaled air from coughing and speaking,” *Chemosphere*, vol. 87, no. 11, pp. 1260–1264, 2012.
- [37] S. B. Poussou, S. Mazumdar, M. W. Plesniak, P. E. Sojka, and Q. Chen, “Flow and contaminant transport in an airliner cabin induced by a moving body: Model experiments and CFD predictions,” *Atmos. Environ.*, vol. 44, no. 24, pp. 2830–2839, 2010.
- [38] M. Z. I. Bangalee, J. J. Miao, S. Y. Lin, and J. H. Yang, “Flow visualization, PIV measurement and CFD calculation for fluid-driven natural cross-ventilation in a scale model,” *Energy Build.*, vol. 66, pp. 306–314, 2013.
- [39] P. Karava, T. Stathopoulos, and A. K. Athienitis, “Airflow assessment in cross-ventilated buildings with operable façade elements,” *Building and Environment*, vol. 46, no. 1, pp. 266–279, 2011.
- [40] R. Ramponi and B. Blocken, “CFD simulation of cross-ventilation flow for different isolated building configurations: Validation with wind tunnel measurements and analysis of physical and numerical diffusion effects,” *J. Wind Eng. Ind. Aerodyn.*, vol. 104–106, pp. 408–418, 2012.
- [41] R. Ramponi and B. Blocken, “CFD simulation of cross-ventilation for a generic isolated building: Impact of computational parameters,” *Build. Environ.*, vol. 53, pp. 34–48, 2012.
- [42] V. A. Reyes, F. Z. Sierra-Espinosa, S. L. Moya, and F. Carrillo, “Flow field obtained by PIV technique for a scaled building-wind tower model in a wind tunnel,” *Energy Build.*, vol. 107, pp. 424–433, 2015.
- [43] M. V. Cruz-Salas, J. A. Castillo, and G. Huelsz, “Experimental study on natural ventilation of a room with a windward window and different windexchangers,” *Energy Build.*, vol. 84,

- pp. 458–465, 2014.
- [44] T. Van Hooff, B. Blocken, T. Defraeye, J. Carmeliet, and G. J. F. Van Heijst, “PIV measurements of a plane wall jet in a confined space at transitional slot Reynolds numbers,” *Exp. Fluids*, 2012.
- [45] J. D. Posner, C. R. Buchanan, and D. Dunn-Rankin, “Measurement and prediction of indoor air flow in a model room,” *Energy Build.*, vol. 35, no. 5, pp. 515–526, 2003.
- [46] L. Zhao, Y. Zhang, X. Wang, G. L. Riskowski, L. L. Christianson, and Q. Chen, “Measurement of two-dimensional air velocities in a full-scale room using particle image velocimetry,” *ASHRAE Trans.*, vol. 107 PART 2, pp. 434–444, 2001.
- [47] X. Cao, J. Liu, J. Pei, Y. Zhang, J. Li, and X. Zhu, “2D-PIV measurement of aircraft cabin air distribution with a high spatial resolution,” *Build. Environ.*, 2014.
- [48] G. Günther, J. Bosbach, J. Pennecot, C. Wagner, T. Lerche, and I. Gores, “Experimental and numerical simulations of idealized aircraft cabin flows,” *Aerosp. Sci. Technol.*, vol. 10, no. 7, pp. 563–573, 2006.
- [49] Y. Sun, Y. Zhang, L. Zhao, and X. Wang, “An algorithm of stereoscopic particle image velocimetry for full-scale room airflow studies,” *ASHRAE Trans.*, vol. 110 PART 1, pp. 75–80, 2004.
- [50] R. P. Lone H. Mortensena, Carsten Rodea, “Investigation of airflow patterns in a microclimate by particle image velocimetry (PIV),” *Am. J. Surg.*, vol. 126, no. 6, pp. 714–716, 2008.
- [51] M. Caciolo, P. Stabat, and D. Marchio, “Full scale experimental study of single-sided ventilation: Analysis of stack and wind effects,” *Energy Build.*, vol. 43, no. 7, pp. 1765–

1773, 2011.

- [52] Y. Z. Huawei sun, Lingying Zhao, “Evaluating RNG k- epsilon Models Using PIV Data for Airflow in Animal Buildings at Different Ventilation Rates,” 2007.
- [53] B. W. J. mohammad H.Hosni, “Development of a particle image velocimetry for measuring air velocity in large-scale room airflow applications: Discussion,” *ASHRAE Trans.*, vol. 108 PART 2, p. 1172, 2002.
- [54] K. C. Kim, H. S. Ji, and S. H. Seong, “Flow structure around a 3-D rectangular prism in a turbulent boundary layer,” *J. Wind Eng. Ind. Aerodyn.*, vol. 91, no. 5, pp. 653–669, 2003.
- [55] Z. Yang, P. Sarkar, and H. Hu, “An experimental study of a high-rise building model in tornado-like winds,” *J. Fluids Struct.*, vol. 27, no. 4, pp. 471–486, 2011.
- [56] J. Allegrini, V. Dorer, and J. Carmeliet, “Wind tunnel measurements of buoyant flows in street canyons,” *Build. Environ.*, vol. 59, pp. 315–326, 2013.
- [57] P. Y. Cui, Z. Li, and W. Q. Tao, “Wind-tunnel measurements for thermal effects on the air flow and pollutant dispersion through different scale urban areas,” *Build. Environ.*, vol. 97, pp. 137–151, 2016.
- [58] Y. Tominaga, S. ichi Akabayashi, T. Kitahara, and Y. Arinami, “Air flow around isolated gable-roof buildings with different roof pitches: Wind tunnel experiments and CFD simulations,” *Build. Environ.*, vol. 84, pp. 204–213, 2015.
- [59] Y. Zhang, P. Sarkar, and H. Hu, “An experimental study of flow fields and wind loads on gable-roof building models in microburst-like wind,” *Exp. Fluids*, vol. 54, no. 5, 2013.
- [60] P. Saarenrinne, M. Piiro, and H. Eloranta, “Experiences of turbulence measurement with PIV,” *Meas. Sci. Technol.*, vol. 12, no. 11, pp. 1904–1910, 2001.

- [61] H. Huang, D. Dabiri, and M. Gharib, "On errors of digital particle image velocimetry," *Meas. Sci. Technol.*, vol. 8, no. 12, pp. 1427–1440, 1997.
- [62] J. Westerweel, "Theoretical analysis of the measurement precision in particle image velocimetry," *Exp. Fluids*, vol. 29, no. 7, pp. S003-S012, 2000.
- [63] and P. W. O. A. K. Prasad, R. J. Adrian, C.C. Landreth, "Effect of resolution on the speed and accuracy of particle image velocimetry interrogation," *Proc. Indian Acad. Sci. - Sect. A*, vol. 31, no. 3, pp. 187–190, 1992.
- [64] J. Li, J. Liu, C. Wang, N. Jiang, and X. Cao, "PIV methods for quantifying human thermal plumes in a cabin environment without ventilation," *J. Vis.*, 2017.
- [65] J. Westerweel, *Digital particle image velocimetry : theory and application*. Delft University Press, 1993.
- [66] A. Fouras and J. Soria, "Accuracy of out-of-plane vorticity measurements derived from in-plane velocity field data," *Exp. Fluids*, vol. 25, no. 5–6, pp. 409–430, 1998.
- [67] R. J. Adrian, "Particle-Imaging Techniques for Experimental Fluid Mechanics," *Annu. Rev. Fluid Mech.*, vol. 23, no. 1, pp. 261–304, 1991.
- [68] B. Böhm, D. Geyer, A. Dreizler, K. K. Venkatesan, N. M. Laurendeau, and M. W. Renfro, "Simultaneous PIV/PTV/OH PLIF imaging: Conditional flow field statistics in partially premixed turbulent opposed jet flames," *Proc. Combust. Inst.*, vol. 31 I, no. 1, pp. 709–717, 2007.
- [69] D. D. A/S, "DynamicStudio User's Guide," p. 685, 2015.
- [70] J. Kitzhofer, F. G. Ergin, and V. Jaunet, "2D Least Squares Matching applied to PIV Challenge data (Part 1)," *16th Int Symp Appl. Laser Tech. to Fluid Mech.*, no. Part 1, pp. 9–

12, 2012.

- [71] R. D. Meyer and G. Tan, “An overview of unsteady analysis techniques for natural wind turbulence and its effects on natural ventilation,” *Int. J. Vent.*, vol. 13, no. 1, 2014.
- [72] L. Pérez-Lombard, J. Ortiz, and C. Pout, “A review on buildings energy consumption information,” *Energy Build.*, vol. 40, no. 3, pp. 394–398, 2008.
- [73] Z. D. Chen and Y. Li, “Buoyancy-driven displacement natural ventilation in a single-zone building with three-level openings,” *Build. Environ.*, vol. 37, no. 3, pp. 295–303, 2002.
- [74] S. R. Livermore and A. W. Woods, “Natural ventilation of a building with heating at multiple levels,” *Build. Environ.*, vol. 42, no. 3, pp. 1417–1430, 2007.
- [75] S. D. Fitzgerald and A. W. Woods, “Transient natural ventilation of a space with localised heating,” *Build. Environ.*, vol. 45, no. 12, pp. 2778–2789, 2010.
- [76] X. Yang, K. Zhong, Y. Kang, and T. Tao, “Numerical investigation on the airflow characteristics and thermal comfort in buoyancy-driven natural ventilation rooms,” *Energy Build.*, vol. 109, pp. 255–266, 2015.
- [77] A. W. W. Shaun D. Fitzgerald* and BP, “Natural ventilation of a room with vents at multiple levels,” *Build. Environ.*, vol. 42, no. 3, pp. 1417–1430, 2007.
- [78] C. Gladstone and A. W. Woods, “On buoyancy-driven natural ventilation of a room with a heated floor,” *J. Fluid Mech.*, vol. 441, pp. 293–314, 2001.
- [79] S. Cui, M. Cohen, P. Stabat, and D. Marchio, “CO₂ tracer gas concentration decay method for measuring air change rate,” *Build. Environ.*, vol. 84, pp. 162–169, 2015.
- [80] T. G. M. Demmers, L. R. Burgess, V. R. Phillips, J. A. Clark, and C. M. Wathes,

- “Assessment of techniques for measuring the ventilation rate, using an experimental building section,” *J. Agric. Eng. Res.*, vol. 76, no. 1, pp. 71–81, 2000.
- [81] S. Van Buggenhout, A. Van Brecht, S. Eren Özcan, E. Vranken, W. Van Malcot, and D. Berckmans, “Influence of sampling positions on accuracy of tracer gas measurements in ventilated spaces,” *Biosyst. Eng.*, vol. 104, no. 2, pp. 216–223, 2009.
- [82] H. Xin, H. Li, R. T. Burns, R. S. Gates, D. G. Overhults, and J. W. J. Earnest, “Use of CO₂ concentration difference or CO₂ balance to assess ventilation rate of broiler houses,” *Trans. ASABE*, vol. 52, no. 4, pp. 1353–1361, 2009.
- [83] H. Han, C. Y. Shin, I. B. Lee, and K. S. Kwon, “Tracer gas experiment for local mean ages of air from individual supply inlets in a space with multiple inlets,” *Build. Environ.*, vol. 46, no. 12, pp. 2462–2471, 2011.
- [84] H. G. J. Snell, F. Seipelt, and H. F. A. Van Den Weghe, “Ventilation rates and gaseous emissions from naturally ventilated dairy houses,” *Biosyst. Eng.*, vol. 86, no. 1, pp. 67–73, 2003.
- [85] A. Kiwan *et al.*, “Air exchange rate measurements in naturally ventilated dairy buildings using the tracer gas decay method with ⁸⁵Kr, compared to CO₂ mass balance and discharge coefficient methods,” *Biosyst. Eng.*, vol. 116, no. 3, pp. 286–296, 2013.
- [86] M. Samer *et al.*, “Developing the ⁸⁵Kr tracer gas technique for air exchange rate measurements in naturally ventilated animal buildings,” *Biosyst. Eng.*, vol. 109, no. 4, pp. 276–287, 2011.
- [87] A. D. Stavridou and P. E. Prinos, “Unsteady CFD Simulation in a Naturally Ventilated Room with a Localized Heat Source,” *Procedia Environ. Sci.*, vol. 38, pp. 322–330, 2017.

- [88] U.S. Department of Energy, “2011 Buildings Energy Data Book,” *Energy Effic. Renew. Energy Dep.*, p. 286, 2012.
- [89] A. K. P. Steven J. Emmerich, “Energy impacts of infiltration and ventilation in U.S. office buildings using multizone airflow simulation,” in *IAQ Energy 98*, 1998, pp. 191–203.
- [90] L. L. Wang and Z. Zhong, “An approach to determine infiltration characteristics of building entrance equipped with air curtains,” *Energy Build.*, 2014.
- [91] D. Frank and P. F. Linden, “The effects of an opposing buoyancy force on the performance of an air curtain in the doorway of a building,” *Energy Build.*, 2015.
- [92] S. Yang, H. Alrawashdeh, C. Zhang, D. Qi, L. (Leon) Wang, and T. Stathopoulos, “Wind effects on air curtain performance at building entrances,” *Build. Environ.*, 2019.
- [93] M. M. Hefny and R. Ooka, “CFD analysis of pollutant dispersion around buildings: Effect of cell geometry,” *Build. Environ.*, vol. 44, no. 8, pp. 1699–1706, 2009.
- [94] M. Chavez, B. Hajra, T. Stathopoulos, and A. Bahloul, “Near-field pollutant dispersion in the built environment by CFD and wind tunnel simulations,” *J. Wind Eng. Ind. Aerodyn.*, vol. 99, no. 4, pp. 330–339, 2011.
- [95] B. Blocken, T. Stathopoulos, and J. Carmeliet, “CFD simulation of the atmospheric boundary layer: wall function problems,” *Atmos. Environ.*, vol. 41, no. 2, pp. 238–252, 2007.
- [96] V. Narayanan, J. Seyed-Yagoobi, and R. H. Page, “An experimental study of fluid mechanics and heat transfer in an impinging slot jet flow,” *Int. J. Heat Mass Transf.*, 2004.
- [97] F. C. Hayes, “Heat Transfer Characteristics of the Air Curtain.” .
- [98] F. C. Hayes and W. F. Stoecker, “Design Data For Air Curtains,” *ASHRAE Transactions*.

- pp. 168–180, 1969.
- [99] S. Goubran, D. Qi, W. F. Saleh, L. L. Wang, and R. Zmeureanu, “Experimental study on the flow characteristics of air curtains at building entrances,” *Build. Environ.*, 2016.
- [100] P. Karava, A. K. Athienitis, T. Stathopoulos, and E. Mouriki, “Experimental study of the thermal performance of a large institutional building with mixed-mode cooling and hybrid ventilation,” *Build. Environ.*, vol. 57, pp. 313–326, 2012.
- [101] S. Hussain and P. H. Oosthuizen, “Validation of numerical modeling of conditions in an atrium space with a hybrid ventilation system,” *Build. Environ.*, vol. 52, pp. 152–161, 2012.
- [102] R. L. Korthals, S. L. Knight, L. L. Christianson, and L. Art Spomer, “Chambers for Studying the Effects of Airflow Velocity on Plant Growth,” *Biotronics*, vol. 23, pp. 113–119, 1994.
- [103] “Effects of Air Current Speed on Net Photosynthetic and Evapotranspiration Rates of a Tomato plug sheet under artificial light,” *Environ. Control Biol.*, vol. 36, no. 3, pp. 131–136, 1998.
- [104] Y. Zhang, M. Kacira, and L. An, “A CFD study on improving air flow uniformity in indoor plant factory system,” *Biosyst. Eng.*, vol. 147, pp. 193–205, 2016.
- [105] Y. Kitaya, “Importance of air movement for promoting gas and heat exchanges between plants and atmosphere under controlled environments,” in *Plant response to air pollution and global change*, & L. J. D. K. K. Omasa, I. Nouchi, Ed. Tokyo, Japan: Springer-Verlag, 2005, pp. 185–193.
- [106] A. Li, T. Ren, C. Yang, J. Xiong, and P. Tao, “Numerical simulation, PIV measurements and analysis of air movement influenced by nozzle jets and heat sources in underground generator hall,” *Build. Environ.*, vol. 131, no. January, pp. 16–31, 2018.

- [107] H. Fellouah, C. G. Ball, and A. Pollard, “Reynolds number effects within the development region of a turbulent round free jet,” *Int. J. Heat Mass Transf.*, vol. 52, no. 17–18, pp. 3943–3954, 2009.
- [108] A. Benaissa and T. Gisselbrecht, “Self-similar evolution of velocity and temperature small scales in a turbulent round jet,” *Eur. J. Mech. B/Fluids*, vol. 42, pp. 169–175, 2013.
- [109] F. Pigozzo, “Universal Gas Analyzer,” 2011.
- [110] Zengji Cai and Tianyu Long, “Fluid mechanics pump and fan”, China Construction Industry Press, 1999.
- [111] <https://www.photonicsonline.com/doc/ndyag-laser-0002>

APPENDIX1: PIV MEASUREMENT PROCEDURE

1. Start DynamicStudio

Start DynamicStudio.

Open the existing DynamicStudio database or create a new one to hold the images which is going to be acquired later.

To create a new one, click “New Database” in “File” menu and specify name and location for a new database.

DynamicStudio database has file extension “*.dynamix” and contain information about the relation between the different datasets as well as about how raw images were acquired. The actual data are not in the database itself, but in a folder with the same name, where sub folders are used to organize the data.

Enter the acquisition mode by clicking the acquisition button  on the toolbar or pressing “Enter Acquisition Mode” in “Run” menu.

Cameras and synchronization devices are auto-detected and appear in the “Devices” list. The auto-detection will also detect if connection is lost to either of them and indicate this by changing the text color to red.

Lasers and other light sources have to be added manually as they typically can’t be auto-detected. Right click in the device list and select “Add New Device” in the context menu. Then the list for light sources, custom synchronization, detector, intensifier and simulation will show. For our laser device, select “NewWave Solo”.

After adding all the devices, they can all be seen in the “Synchronization Cables” panel. Connect each devices as shown below, just use the mouse to draw a line between each related port. Or right click the blank space in the “Synchronization Cables” panel, and choose the “Create Default Connections” to finish the connection of all the devices.

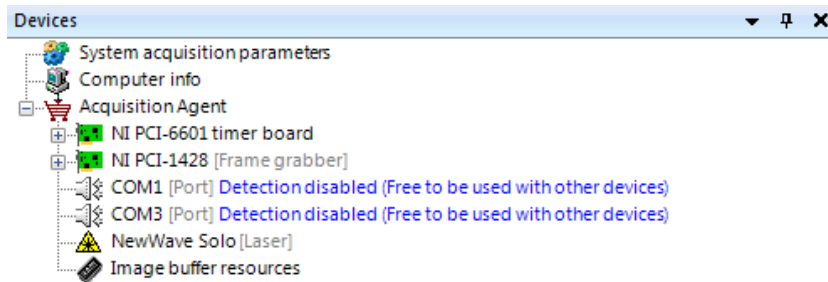


Figure A1-1 DynamicStudio devices list

2. Laser light sheet alignment

Set the laser head on a secure optical table, the beam of traverse or a tripod firmly to be fixed down. Also, the laser head should be installed in a place that the light sheet can pass the measurement plane. And place the laser power supply unit in a free place with air circulation.

Turn the power supply key switch of the laser clockwise to the “ON” position and keep the laser in “internal mode”. Adjust the laser power to the minimum required for light sheet alignment by rotating the “Rep Rate” knob counterclockwise to the minimum position.

Before turn on the laser, make sure you wear the safety goggles which can block the green light and avoid both direct and diffused laser light.

Put the testing model or plane target in the measurement area in order to align the laser light sheet to the measurement plane as much as possible.

Press the “Start/Standby” button on the control panel until the power supply interlock LED is off and the control panel laser emission LED is on.

Press the Fire Laser 1, Fire Laser 2 or both buttons on the control panel to initiate laser firing. If both the Fire Laser 1 and Fire Laser 2 buttons have been pressed, the lasers fire alternately. Either laser button can be toggled on and off using the Laser1/Laser2 Fire buttons. Adjust the “Rep Rate” knob set to the desired laser power. Press the energy High/Low button to select desired energy level.

Rotate the optics to generate the light sheet in the required plane of measurements and adjust the light sheet thickness by moving the lens focus.

Select a suitable height of light sheet based on the distance between sheet optics and the field of view and the size of the field of view. To locate the appropriate laser sheet position and thickness, a piece of black paper can be used to put in front of the laser sheet. For illuminating the particles, the laser sheet should be oriented overlapped to the plane of flow that concerned. Also, the main velocity component of flow should be parallel to the light sheet, in order to minimize systematic errors and out-of-plane loss of particles.

Minimize surface reflection light and check that nothing hits the camera lens. Switch the laser off by pressing “Off” button.



Figure A1-2 Control panel of laser

3. Camera alignment

Put the testing model or plane target in the measurement area for camera alignment and calibration.

Normally a standard ruler will be chosen as the calibration target.

Enter the acquisition mode of DynamicStudio software and set up the acquisition parameters in “System control” panel. “Single frame mode” should be selected. Long exposure time is required for the camera to capture enough illumination, since no laser illumination. The exposure time can be set in the Devices Properties panel, corresponding to the selected camera. A long exposure time, such as 10000 μ s or longer is suggested.

Click “Free Run” in System Control panel to start acquiring image. In free run the camera is running freely without synchronized with other hardware devices which means that in this mode the laser is not flashing, and the frame rate of the camera does not necessarily correspond to the nominal value from the system control. It will be able to see images and focus the camera if ambient light is strong enough compared to exposure time.

Refine the position or the attitude of the camera as well as its focus until a clear view of ruler can be seen in the computer. The digital camera should be located at 90° to the light sheet so that the light scattered by the particles can be recorded.

After the camera is well aligned, click “Stop” in System Control panel.

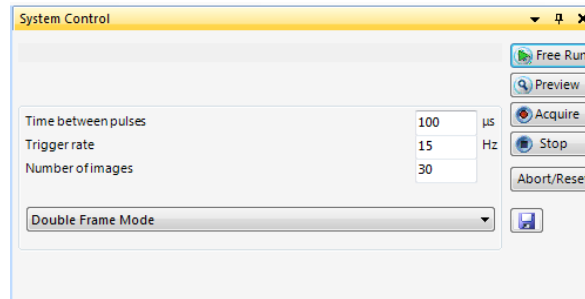


Figure A1-3 Acquisition setup in DynamicStudio system control panel

4. Calibration

Then after the camera and laser sheet are all aligned for acquiring pictures, keep the ‘Single Frame mode’ and click the “Free Run” to acquire images.

Switch to “Acquired Data” panel.

If the acquired images are satisfied, click the “Save for Calibration” button to save the image of calibration target.

A new project need to be created by right clicking the database and select “Create Project”. Then the calibration image will be saved in the new project.

For the velocity measurement, the scale factor, which gives a proportional relation between real length in the physical world and how many pixels corresponding that length can be determined automatically based on the real length of the calibration ruler.

Right-click the calibration image and select “Measure scale factor”. Press “O” and left mouse button to select origin point. Press “A” and left mouse button to select “A” position. Press “B” and left mouse button to select “B” position. Normally just specify “A” and “B” position on clear scale of ruler. Then type in the absolute distance between position “A” and “B” by reading the distance on the ruler. Click “OK” and then the calibration for camera is done.



Figure A1-4 Measure scale factor for calibration

5. Flow visualization

Before the data acquiring, flow visualization is better to be conducted before to check the particle tracking behaviors in the flow field.

Remove the calibration target in the measurement area. Turn off the light of the lab. Start the tracing seeds supply.

Set the both “flashlamp” and “Q-switch” to external trigger mode by pressing the “Ext” button on the control panel of laser. Press the “Start/Standby” button on the control panel until the power supply interlock LED is off and the control panel laser emission LED is on. Normally the laser power need to be switched to “High” level in the control panel of laser.

Select “Double Frame mode” in the System Control panel of DynamicStudio software.

Adjust the “Time between pulses”. The time between pulses should be long enough to determine the displacement of the particles between two pulses, also need to be short enough to avoid particles leaving out of the interrogation area. Start from the minimum exposure time 10-15 μ s based on camera series.

Specify the number of images to acquire and trigger rate.

Click the “Preview” to start the preview mode. In preview mode all devices are synchronized, the laser is flashing and camera triggers acquires images at the rate specified in the System Control panel. It will not stop acquiring images when the requested number of images have been acquired, but simply overwrite the oldest image with the most recent one.

Check the flow field in the screen. The power of the laser can be increased in small steps to keep the camera image from being saturated during the image visualization until the illuminated particles show the best definition. Generally, the seeds concentration in the flow and the camera aperture focus should be adjusted according to the visualization. The extreme high concentration of particles with relatively poorly adjusted camera aperture, may lead to lower spatial resolution of the measurements.

During the flow visualization, double click the image shown, or right-click and select “Color map and histogram”. Then the color of the map can be set to make the seeds movement looked more clearly. Normally the color of image can be set to green as the light sheet is green.

6. Data acquisition

If the image quality is acceptable then stop the preview mode.

Start the “Acquire mode”. Acquire does exactly the same as Preview with the one exception that it stops when the requested number of images have been acquired.

Click “Save in Database” after required numbers of images have been acquired.

The quality of image could be check by observing the cross-correlation map immediately. Right-click the acquired image, select “Cross-Correlation Map”, the cross-correlation map to each interrogation area can be observed. It is better to repeat each measurement several times to achieve accuracy results, for example repeat each measurement 5 times and use the average value.

7. Pre-processing

The correlation signal is strongly affected by the variation in image intensity. The non-uniform illumination of particle image intensity, due to light-sheet non-uniformities or pulse-to-pulse variation, or irregular particle shape, out-of-plane motion, etc., create noise in the correlation signal. Therefore, pre-processing of particle image is often very necessary, Select the proper image process method, in the image processing library.

To define mask, select an image ensemble and bring up the analysis selection dialog. Then select the “Define Mask” in the “Masking” category.

The mask can be composed of three types of shapes (rectangles, polygons and ellipses). To add a shape to the mask, click on the desired mask shape in the toolbar, and select the appropriate mask type (reject, outside, disable or transparent).

After the shape and mask type has been selected, click on the image to start to specify the shape location and size. The shape of mask can be further adjusted after the appearance has been created.

To mask double frame images, first pre-select the mask as “User Selection” by selecting it and pressing the “Space bar” "Selection. Then select the ensemble with images to be masked and select the analysis method “Image Masking”.

In the recipe the gray-value can be specified to be assigned to masked pixels in the parent image: Black-out areas, White-out areas, Mean pixel value and User-defined (fixed) value.

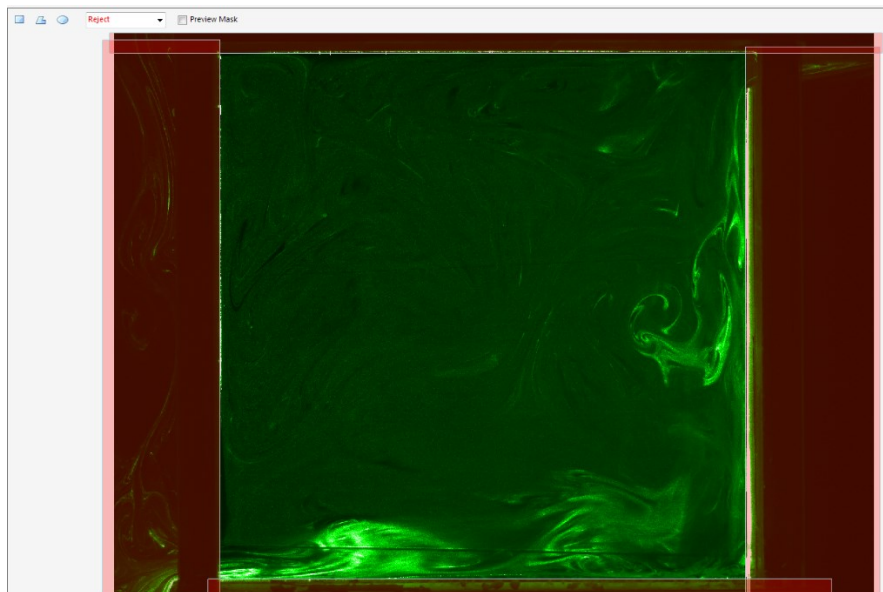


Figure A1-5 Define mask

8. Image evaluation

After pre-processing image, the image evaluation method need be applied to convert pairs of particle images into velocity field.

Right click the image after pre-processing and select “Analyze” option. Select the proper image evaluation method as shown in “PIV Signal” category. Some of the evaluation methods are shown in the Table 12 below.

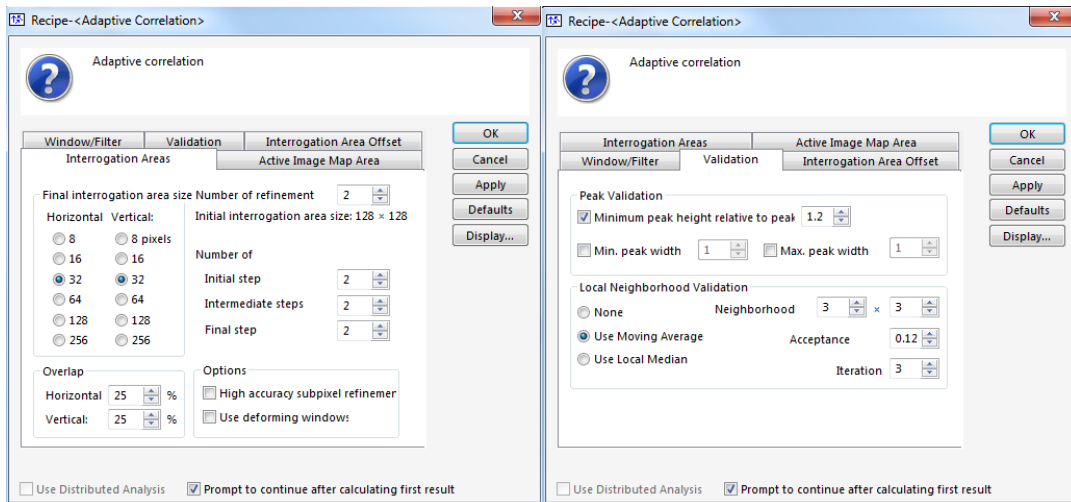
Table 12 Evaluation methods in DynamicStudio

2D Least Squares Matching (LSM)	2D Least Squares matching (LSM) is a method for determining 2D velocity fields in highly seeded flows in water and air.
Adaptive Correction	The adaptive correlation method calculates velocity vectors with an initial interrogation area (IA) of the size N time the size of the final IA and uses the intermediary results as information for the next IA of smaller size, until the final IA size is reached.
Adaptive PIV	The Adaptive PIV method will iteratively adjust the size and shape of the individual interrogation areas (IA) in order to adapt to local seeding densities and flow gradients.
Average Correction	When there are only few particles in the flow one can compute the average flow field through Average correlation. In Average correlation, the correlation function of each interrogation areas is averaged at each location for all the images.

Normally adaptive correlation method can be used for indoor ventilation measurements. Choose the “Adaptive Correlation”.

Final interrogation area size is the smallest grid of iterated operation. Usually, it will be better to choose 32×32 pixels or 64×64 pixels. Overlap means to find the correlative particles in a bigger area to do the calculation, usually choose 25% or 50% for both horizontal and vertical. In options, when the diameters of particles is smaller than one pixel, High accuracy subpixel refiner should be chose, which will improve the peak locking, with slowing down the speed of calculation. Use

deforming windows is for big gradient of fluid flow, which can improve the accuracy of removing bad results.



(a)

(b)

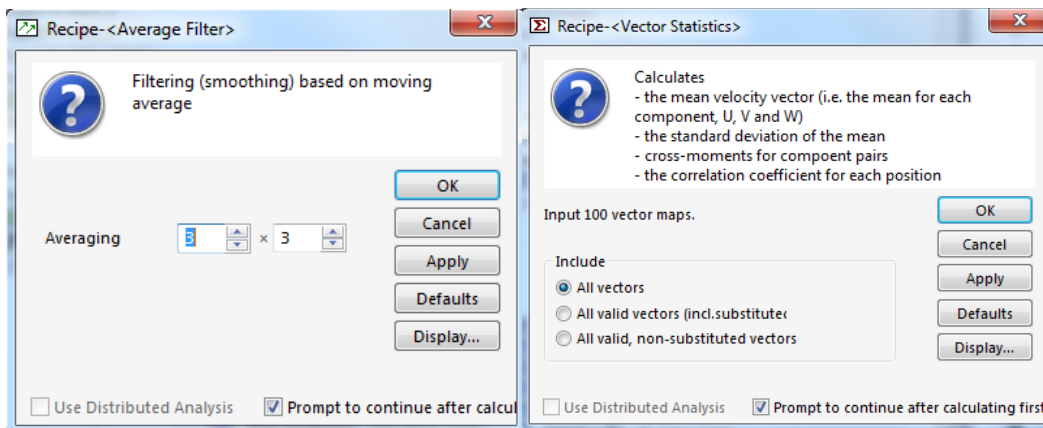
Figure A1-6 Adaptive correlation: (a) interrogation areas; (b) validation

In the “Peak validation” section, the minimum and the maximum peak widths as well as the minimum peak height ratio (between 1st and 2nd peak) can be set. Usually choose Minimum peak height relative to peak, and set to range from 1.1 to 2 for relative high particle concentration.

With “Local neighborhood validation”, individual vectors are compared to the local vectors in the neighborhood vector area, which size $M \times M$ can be set. If a spurious vector is detected, it is removed and replaced by a vector, which is calculated by local interpolation of the vectors present in the $M \times M$ area.

Normally choose “Using moving average”. Spurious vectors are identified according to the value of the “Acceptance factor”. This factor effectively allows a given degree of freedom on velocity vector gradient inside the $M \times M$ area and if the calculated gradient is larger than set, the central

vector is removed. The larger this factor is, the less the velocity vector map is spatially corrected. It is better to set the acceptance factor 0.1-0.15. Then click “OK”, vector maps could be obtained. After correlation, average filter is always used to filter out vector maps by arithmetic averaging over vector neighbors. This method is used to filter out vector maps by arithmetic averaging over vector neighbors. Typical averaging area sizes are 3×3 or 5×5 for indoor ventilation measurements. After that, there are still hundreds of velocity vectors images which is difficult to be used to describe the fluid mechanical features. Select “Vector Statistics” after right click the results after average filter. Choose “All vectors” and click “OK”. Then the mea velocity vectors can be obtained. Also, the numerical data of the vector map can be seen by right clicking the map and selecting “Open as Numeric”.



(a)

(b)

Figure A1-7 (a) average filter; (b) vector statistics

9. Post-processing

After PIV process, a vector map will be obtained. DynamicStudio offers various post-processing algorithms, including various plot, statistics analysis and many additionally calculations. Post-

processing of the data can be done in DynamicStudio or in other software like Tecplot. Then the results must be exported from the PIV software.

Right-click on the record and select “Export” or select “Export” in “File” menu.

If choose “Image export”, specify the destination path, base file name, file type, and then press “OK”. If choose “Image export”, specify the destination path, base file name, file type, and then press “OK”. To export video, select “AVI” as file type and specify the play rate.

If choose “Numerical Export”, four export formats can be chosen. “.csv”: Comma separated values; “.txt”: Tab delimited text file; “.dat”: Tecplot data file; “.xml”: Extensible Markup Language. Normally, “.dat” and “.csv” file will be exported for further processing in Tecplot and excel.

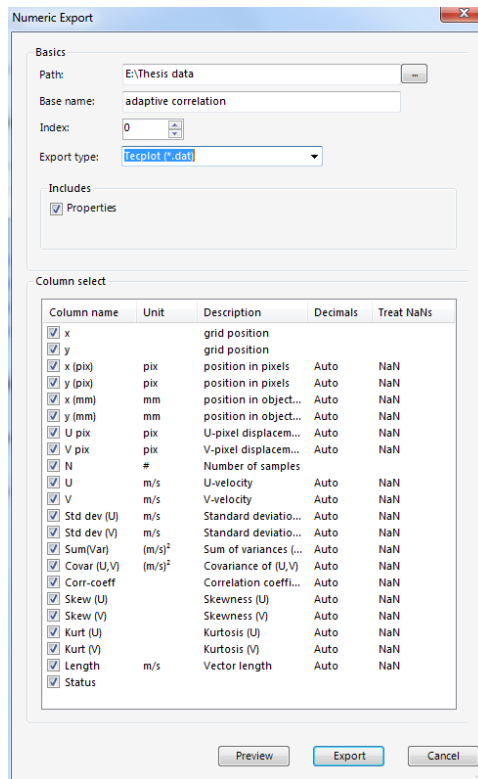


Figure A1-8 Numeric export

APPENDIX2: TRACER GAS MEASUREMENT PROCEDURE

1. Start UGA

Universal Gas Analyzer (UGA) instrument is modern mass spectrometers designed for the analysis of gases. The UGA system can be considered as two main subsystems: gas handling and analyzer. The gas handling system consists of capillaries, multiple inlet valves, a sample valve, a pinhole, a bypass pump (BP), a bypass valve, a turbo pump (TP), and a roughing pump (RP), which can deliver the sample gas into the analyzer. A quadrupole mass spectrometer (also called a residual gas analyzer or RGA) performs the task of analyzing the gas under high vacuum. Fig. A-9 shows the basic schematic of UGA system.

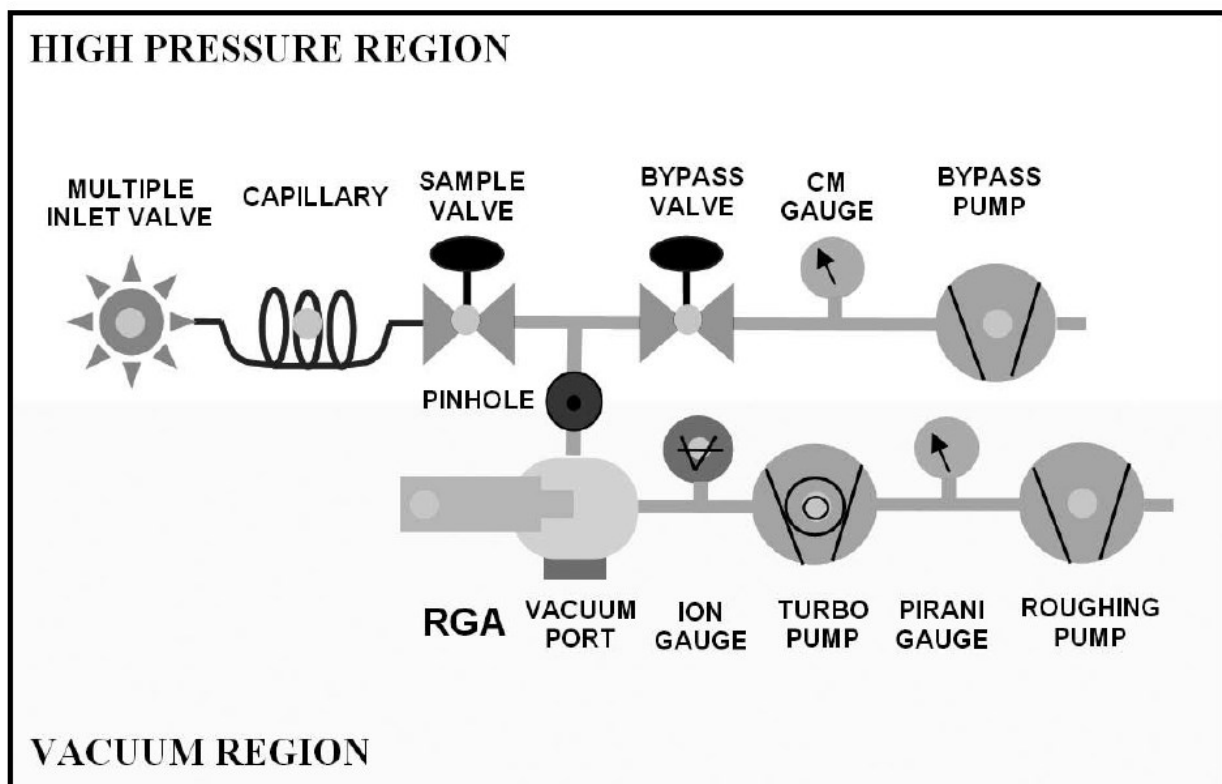


Figure A2-1 UGA schematic[109]

UGA can be operated both manually and automatically by computer. But in order to obtain RGA data, the UGA needs to be connected to the computer, which means even though the system can be operated from the front panel, RGA software will be used to analyze the sample gas. RGA can only be controlled after UGA is connected with computer, which is why it is essential to install both UGA and RGA software first.

Connect the computer and UGA with an RS232 serial connection. Power up the UGA.

From the front panel choose the baud rate as follows. The default rate is 38400. Push the “Level-up” button to enter the UGA menu. Choose “Communication” to move to the next menu tree. Choose “RS232 Baud Rate”. Choose the desired baud rate at the menu. Push the “Level-up” button several times to escape the menu.

After install the UGA and RGA software, start the UGA software.

Click on the “Main” tab, and select “Connection Settings”. In the “Connection Settings” dialog box, choose the “Serial” tab. Verify that the serial resource match the baud rate with UGA setting as shown in the Fig.A2-2, then click “OK”.

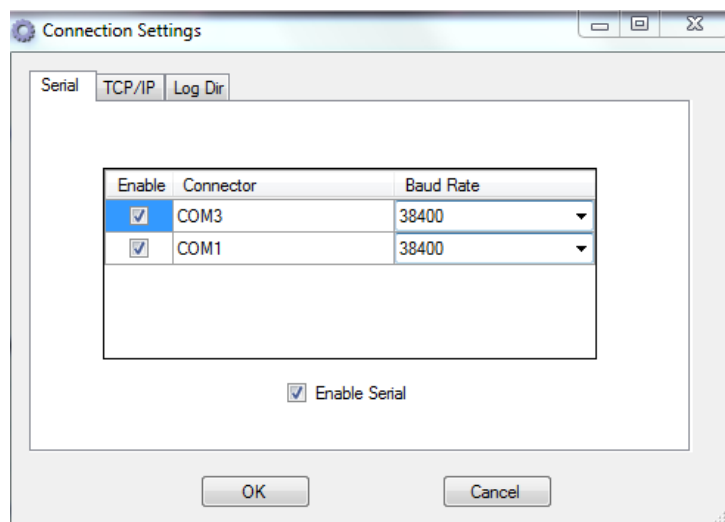


Figure A2-2 Connection Settings

Click on the “Main” menu, and select “Connect”. The software will show the available resources. Select the appropriate COM port and click the “Connect” button.

After the icon indicating the current connection mode changes to green color, close the “ConnectorDialog” window.

UGA can be controlled both by front panel manually or by software automatically. In the UGA software as shown in Fig.A2-3, click the green “Start” button to start UGA and wait until the current status becomes the ready state. It will take about 5 minutes to reach this state. On the left part of the screen, the present states of all the components like valves and pumps, and options like multiple inlet, are indicated by LED graphics. The LED shows green light when the item is on or open. Also, the operation status is shown in the screen, for example, the pressure and temperature of the pump and chamber.

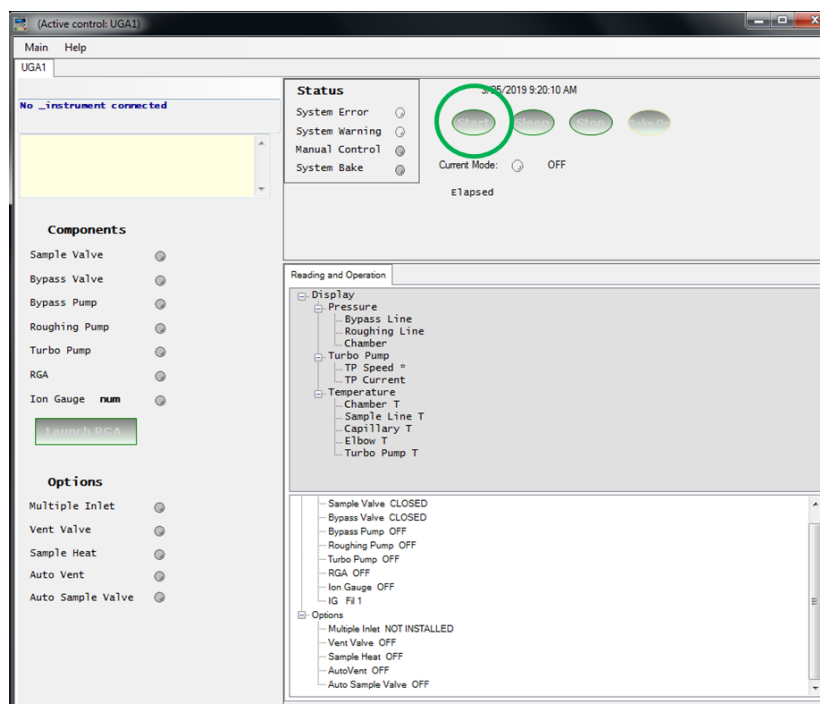


Figure A2-3 UGA software

Although, UGA can be operated by computer, it is better to start UGA manually from the front panel as the status of each pump and valve can be checked during the operation.

Enter the UGA menu system by pushing the “Level-up” button on the control keypad. Enter the “Display” menu and select “Pressure”.

Push the “Bypass Pump” button on the status keypad. Turn on the Bypass Pump (BP) with the control keypad. Wait for the bypass line pressure to 0.1 to 0.3 Torr, which will take about one minute.

Push the “Roughing Pump” button on the status keypad. Turn on the Roughing Pump (RP) with the control keypad. Generally the reading of RP pressure will go down to less than 1 Torr quickly, if the system was in good vacuum. This means the chamber was pumped out well before.

Open Bypass Valve (BV) and wait till BP and RP pressure goes down at least below 0.3 Torr. If the pressure does not go down that level in a couple of hours, then try to increase the pumping powers from 60 to 90. And then wait till the readings get below at least 0.3 Torr. If the system gets enough low pressure, then reset the pumping powers to 60.

Push the “Turbo Pump” button on the status keypad. Turn on the Turbo Pump (TP) with the control keypad. The TP speed can be checked in the TP display. Push the up or down arrow button to see the TP information during the pressure display. Wait until the TP reaches full speed (81k RPM), and TP current should be below 1A.

If all parameters are normal, turn on Ion Gauge (IG) after waiting for eight minutes with TP running in full speed. Keep watching IG pressure reading. It should go up, then go down to below 10^{-6} Torr.

2. Start RGA

Install the capillaries on the multiple inlet of the UGA. Then put capillaries into the measurement points.

When the Current Mode indicator of UGA software shows the ready state, launch RGA software by clicking the “Launch RGA” button. The RGA software automatically connects to RGA through UGA.

Push the “RGA” button on the status keypad. Turn on the RGA with the control keypad.

Push the “Sample Valve” button on the status keypad. Turn on the Sample Valve (SV) with the control keypad. The system will read approximately 1.5 Torr at the bypass line, and 5×10^{-6} Torr for the mass spectrometer chamber.

From the RGA software, click the filament button on the toolbar to activate the ionizer. Change the data acquisition mode by clicking Mode menu and choose “P vs T”. Click Scan menu and choose “Scan Parameters”. Add carbon dioxide (CO₂) into the measurement list and then click “Apply” as shown in Fig.A2-4. Click Scan menu and choose “Schedule”. Choose “Continuous” in data acquisition then click “Apply” as shown in Fig.A2-5

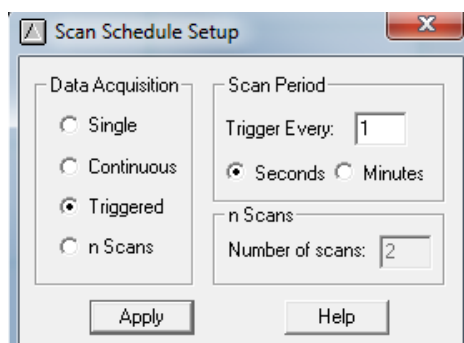


Figure A2-4 Scan Schedule Setup

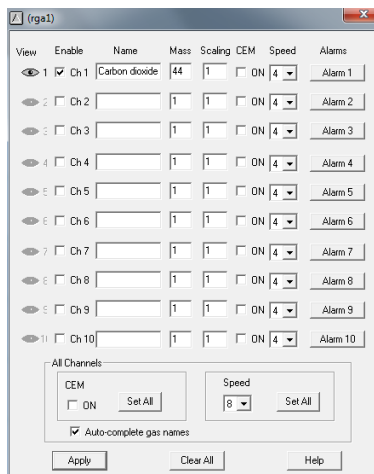


Figure A2-5 Scan Parameters

Click the “GO” button on the tool bar and an analog scan will start. The spectrum of gas around test capillaries will be displayed.

3. Data acquisition

At the beginning of the test, close the inlet and outlet of the chamber. Then inject CO₂ into the chamber from a cylinder. Watch the reading in the RGA software. When the CO₂ concentration value for the three measurement points are close, which means the concentration is homogeneous in the chamber, then stop the injection.

Open the inlet and outlet of the chamber. Then the reading of CO₂ will go down quickly. Stop the scan by clicking “Stop” when the reading reach the background value and does not change.

Export the data by click File menu and choose “Save ASCII Data”. Choose the destination path and then the data can be exported as “.txt” type for further analysis.